R.T.
YILDIZ TECHNICAL UNIVERSITY
GRADUATE SCHOOL OF NATURAL AND APPLIED SCIENCE

COMPUTATION OF ELECTROMAGNETIC FIELDS SCATTERED BY CYLINDRICAL TARGETS BURIED IN A MEDIUM WITH A PERIODIC SURFACE

SENEM MAKAL

Ph.D. THESIS
DEPARTMENT OF ELECTRONICS AND COMMUNICATIONS ENGINEERING
COMMUNICATION

ADVISOR
ASSOC. PROF. DR. AHMET KIZILAY

İSTANBUL, 2012

T.C.
YILDIZ TEKNİK ÜNİVERSİTESİ
FEN BİLİMLERİ ENSTİTÜSÜ

PERİYODİK BİR YÜZEY ALTINA GÖMÜLÜ SİLİNDİRİK HEDEFLERDEN SAÇILAN ELEKTROMAGNETİK ALANLARIN HESAPLANMASI

Senem Makal tarafından hazırlanan tez çalışması 18.01.2012 tarihinde aşağıdaki jüri tarafından Yıldız Teknik Üniversitesi Fen Bilimleri Enstitüsü Elektronik ve Haberleşme Mühendisliği Anabilim Dalı'nda **DOKTORA TEZİ** olarak kabul edilmiştir.

Tez Danışmanı
Doç. Dr. Ahmet KIZILAY
Yıldız Teknik Üniversitesi

Jüri Üyeleri
Doç. Dr. Ahmet KIZILAY
Yıldız Teknik Üniversitesi ______________________

Prof. Dr. Filiz GÜNEŞ
Yıldız Teknik Üniversitesi ______________________

Doç. Dr. Selçuk PAKER
İstanbul Teknik Üniversitesi ______________________

Prof. Dr. Sedef KENT
İstanbul Teknik Üniversitesi ______________________

Yrd. Doç. Dr. Hamid TORPİ
Yıldız Teknik Üniversitesi ______________________

This research has been supported by Yildiz Technical University Scientific Research Projects Coordination Department. Project number: 2010-04-03-DOP01.

ACKNOWLEDGEMENT

I would like to express my immense gratitude to my advisor Assoc. Prof. Dr. Ahmet KIZILAY for his time, guidance, patience and support during this study. I would also like to deeply thank to Prof. Dr. Filiz GÜNEŞ and Assoc. Prof. Dr. Selçuk PAKER for their useful comments and suggestions which have improved the technical content and clarity of this thesis.

I am also grateful to Prof. Dr. Ercüment ARVAS and Asst. Prof. Dr. Hamid TORPİ for their help and advices.

I could never give enough thanks to my family who provided me with love and support throughout my studies.

More thanks of a special kind are appropriate to my friends who are the research assistants in YTU.

I also thank The Scientific and Technological Research Council of Turkey (TÜBİTAK) for national scholarship supported me during my Ph.D. education.

January, 2012

Senem MAKAL

TABLE OF CONTENTS

Page No

CHAPTER 1

CHAPTER 2

CHAPTER 3

CHAPTER 4

CHAPTER 5

CHAPTER 6

CHAPTER 7

APPENDIX-A

APPENDIX-B

LIST OF SYMBOLS

$\vec{E}$	Electric field vector
$\vec{H}$	Magnetic field vector
$\vec{J}$	Surface electric current density
$\vec{M}$	Surface magnetic current density
ε	Dielectric permitivity
μ	Permeability
σ	Conductivity
k	Wavenumber
λ	Wavelength
ϕ	Angle
$\vec{\rho}$	Position vector
r	Radius
S	Surface
σ_{TM}	Radar cross section

LIST OF ABBREVIATIONS

TM	Transverse Magnetic
EFIE	Electric Field Integral Equation
MoM	Method of Moments
E-Field	Electric Field
ppw	Points per Free-space Wavelength
PEC	Perfectly Conducting
PV	Principal Value

LIST OF FIGURES

Page No

ABSTRACT

COMPUTATION OF ELECTROMAGNETIC FIELDS SCATTERED BY CYLINDRICAL TARGETS BURIED IN A MEDIUM WITH A PERIODIC SURFACE

Senem MAKAL

Department of Electronics and Communications Engineering

Ph.D. Thesis

Advisor: Assoc. Prof. Dr. Ahmet KIZILAY

Electromagnetic scattering from a two dimensional, cylindrical, and dielectric object of arbitrary cross-section buried in a lossy dielectric half-space having a periodically rough surface is investigated by a new numerical method. The method is outlined for TM_z (horizontally) polarized incident wave.

The basis of the new solution technique is that if a target is close to the surface, the electromagnetic fields will be nearly identical to that without the target, except within the region of finite extent near the target. Thus, the current on the surface will be affected only in a finite portion of the surface near the target. The electric field integral equations (EFIEs) for the equivalent currents on the target and the perturbation equivalent currents (the difference currents with target present and with target absent) on the surface are obtained by using this approach and solved by the Method of Moment (MoM) in frequency domain. Then, inverse Fourier transform is utilized to get the time domain signals. The short-pulse scattering results is used to investigate the effects of multipath.

Key Words: Electromagnetic scattering, the Method of Moment, perturbational field, integral equations.

YILDIZ TECHNICAL UNIVERSITY

GRADUATE SCHOOL OF NATURAL AND APPLIED SCIENCE

ÖZET

PERİYODİK BİR YÜZEY ALTINA GÖMÜLÜ SİLİNDİRİK HEDEFLERDEN SAÇILAN ELEKTROMAGNETİK ALANLARIN HESAPLANMASI

Senem MAKAL

Elektronik ve Haberleşme Mühendisliği Anabilim Dalı
Doktora Tezi

Danışman: Doç. Dr. Ahmet KIZILAY

Sonsuz uzun, engebeli ve kayıplı bir dielektrik ortamda gömülü bir dielektrik hedeften saçılan elektromagnetik dalganın elektriksel alan değeri TM_z polarizasyonu için perturbasyon yaklaşımı ile çözülmüştür.

Kullanılan bu yeni çözüm metodunun temeli, eğer hedef cisim periyodik yüzeye yakın ise, elektromanyetik alanların hedef cismin bulunmadığı durumdaki alanlar ile sadece hedef cisme yakın sonlu bir bölgede farklı olacağına ve bu sayede periyodik yüzeydeki eşdeğerlik akımının hedef cismin hemen üzerindeki sonlu bir yüzeyde değişiklik göstereceğine dayanmaktadır. Bu yaklaşımla silindirik hedefin üzerindeki eşdeğerlik akımlarına ve sinüzoidal yüzey üzerindeki perturbasyon (hedefin olduğu ve olmadığı durumlardaki eşdeğer akımlar arasındaki fark akımı) eşdeğerlik akımlarına ait elde edilen elektrik alan entegral denklemleri, frekans domeninde Moment Metodu kullanarak çözülmüş ve bu sayede geniş bantta, saçılan elektrik alana ait çözümler elde edilmiştir. Sonrasında, ters Fourier dönüşümü ile zaman domeni işaretleri bulunmuş ve böylece kısa darbe saçılma işaretleri kullanılarak çoklu yansıma etkileri incelenmiştir.

Anahtar Kelimeler: Elektromagnetik alanlar, Moment Metodu, perturbasyon alanları, integral denklemleri.

YILDIZ TEKNİK ÜNİVERSİTESİ FEN BİLİMLERİ ENSTİTÜSÜ

CHAPTER 1

INTRODUCTION

1.1 Literature

Solution of the electromagnetic scattering by buried objects has been interested by many researches. Therefore, several techniques have been employed to obtain the scattered fields. This is because scattered field values can be used in nondestructive evaluation applications such as detecting landmines, buried pipes, near-surface geophysical exploration, and also archeological studies [1-7]. As a result, an efficient way of calculating scattered field is important for ground-penetrating radar applications.

Many different techniques have been developed for two-dimensional scattering from buried objects. Especially, a large number of exact and numerical techniques are related to the assumption of a flat interface, because of the reduction of mathematical and computational complexity. For example, Uzunoglu et al. have computed the scattered electric field from underground tunnels using a Green's function approach, and analyzed the scattered amplitude for various observation angles [8]. Kanellopoulos et al. have used the same analytical approach for conducting wires buried in earth [9]. Also, Born approximation and Sommerfield integrals with fast evaluation methods have been the other ways to build an analytical solution for buried scatterer [10-12]. Naqvi et al. have used plane wave expansion and excitation of current on a cylinder for the scattered electric field from a conducting cylinder deeply buried in a dielectric half-space [13]. Another analytical method containing plane wave representation has been developed by Ahmed et al. [14].

In case the surface of the half-space is rough, Cottis and Kanellopoulos assume a sinusoidal interface and use an integral equation combined with the extended boundary condition approach for the scattering from a buried circular cylinder in [15] and [16]. An analytical solution of the scattering problem from a dielectric cylinder buried beneath a slightly rough surface is developed by Lawrence and Sarabandi [17]. Altuncu et al. present a method using the Green's function of the half-space with rough boundary where the cylindrical bodies are located [18].

1.2 The Aim of the Thesis

The aim of this thesis is to obtain a fast and simple solution method for the complex problem of calculation of the scattered fields from a cylindrical object buried under a rough surface. This new solution technique is outlined for TM_z scattering from a cylindrical object buried in a lossy half-space. The surface equivalence principle and a perturbation method are employed to form a set of EFIEs for the currents on the object and the portion of the surface most strongly interacting with the object. Then, MoM is used to solve the EFIEs in the frequency domain to obtain the scattered electric field, and inverse Fourier transform is utilized to get the time domain signals.

1.3 Hypothesis

The idea behind the new solution technique is that if a target is close to the surface, the electromagnetic fields will be nearly identical to that without the target, except within the region of finite extent near the target [19, 20]. Thus, the current on the surface will be affected only in a finite portion of the surface near the target. Therefore, the perturbation equivalent currents are approximated to zero outside a finite region above the object. The EFIEs are solved in the frequency domain using MoM, and transformed into the time domain using IFT.

CHAPTER 2

COMPUTATION OF TM$_z$ SCATTERING FROM A CYLINDRICAL DIELECTRIC OBJECT

2.1 Introduction

The problem of electromagnetic scattering from a two-dimensional, dielectric, and cylindrical object of arbitrary cross section is considered. First, the analytical solution of the problem is obtained. Then, the surface equivalence principle is used for the numerical solution of the same problem. Numerical solution method is outlined for the case of arbitrary cross-section, and specialized for circular cross-section. Finally, computed results of these two solutions are compared.

2.2 Analytical Solution

The scattered electric field from a dielectric cylindrical object of circular cross section is calculated by expressing the plane waves by cylindrical wave functions [21, 22]. As shown in Figure 2.1, TM$_z$ polarized incident wave $\left(\vec{E}^i\right)$ is assumed to be incident with the incidence angle of ϕ_i on the object having a radius r_a. The surface of the object is represented by S_c.

The plane waves can be represented by an infinite sum of cylindrical wave functions, and the incident electric field [21, 22]

$$\vec{E}^i = \hat{z}E_z^i = \hat{z}E_0 \sum_{n=-\infty}^{+\infty} j^{-n} J_n\left(k_0\rho\right) e^{jn\phi} \tag{2.1}$$

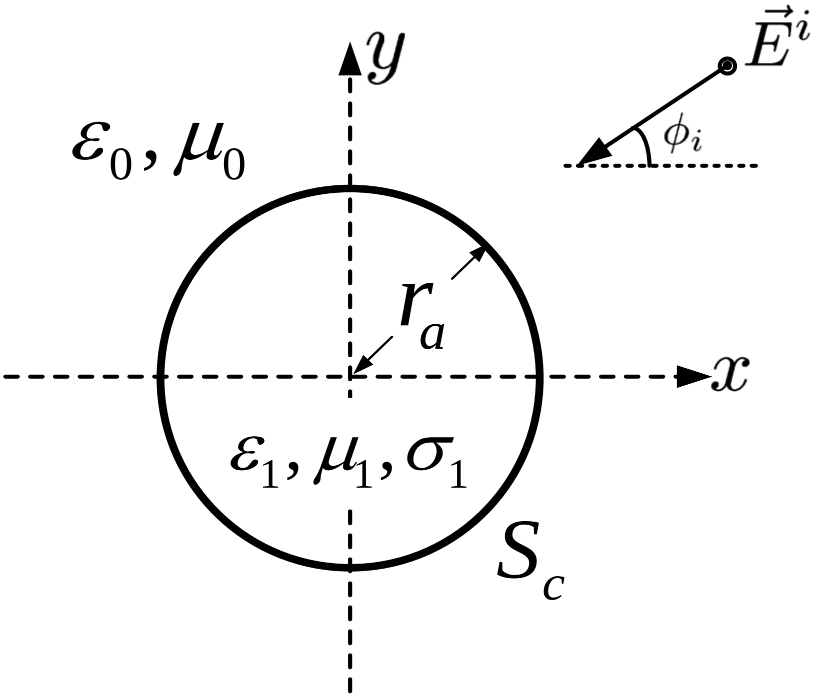

Figure 2. 1 An infinitely long cylindrical object of circular cross-section.

since it must be periodic in ϕ and finite at $\rho = 0$, where ρ is the magnitude of the two-dimensional position vector. Here, k_0 is the free-space wave number. The position vector

$$\vec{\rho} = x\hat{x} + y\hat{y} \tag{2.2}$$

The scattered electric field in the region exterior to the cylinder

$$\vec{E}^s = \hat{z}E_0 \sum_{n=-\infty}^{+\infty} j^{-n} a_n H_n^{(2)}\left(k_0\rho\right) e^{jn\phi} \tag{2.3}$$

and the total field in the cylinder

$$\vec{E}^t = \hat{z}E_0 \sum_{n=-\infty}^{+\infty} j^{-n} b_n J_n\left(k_1\rho\right) e^{jn\phi} \tag{2.4}$$

where $k_1 = \omega\sqrt{\mu_1 \varepsilon_{c1}}$, and $\varepsilon_{c1} = \varepsilon_1 \left(1 - j\dfrac{\sigma_1}{\omega\varepsilon_1}\right)$. The magnetic field can be computed from the electric field (E-field), and therefore [21, 22]

$$\vec{H}^i = -\frac{1}{j\omega\mu_0} \nabla \times \vec{E}^i = \hat{\phi}\frac{E_0}{j\eta_0} \sum_{n=-\infty}^{+\infty} j^{-n} J_n'\left(k_0\rho\right) e^{jn\phi} \tag{2.5}$$

$$\vec{H}^s = -\frac{1}{j\omega\mu_0}\nabla\times\vec{E}^s = \hat{\phi}\frac{E_0}{j\eta_0}\sum_{n=-\infty}^{+\infty} j^{-n}a_n H_n'^{(2)}\left(k_0\rho\right)e^{jn\phi} \tag{2.6}$$

$$\vec{H}^t = -\frac{1}{j\omega\mu_1}\nabla\times\vec{E}^t = \hat{\phi}\frac{E_0}{j\eta_1}\sum_{n=-\infty}^{+\infty} j^{-n}b_n J_n'\left(k_1\rho\right)e^{jn\phi} \tag{2.7}$$

where $\eta_0 = \sqrt{\mu_0 / \varepsilon_0}$ and $\eta_1 = \sqrt{\mu_1 / \varepsilon_{c1}}$ are the intrinsic impedance of free half-space and lossy dielectric, respectively. The unknown coefficients a_n and b_n can be found by applying the boundary condition of

$$\vec{E}_z^i\left(r_a,\phi\right)+\vec{E}_z^s\left(r_a,\phi\right)=\vec{E}_z^t\left(r_a,\phi\right) \tag{2.8}$$

$$\vec{H}_\phi^i\left(r_a,\phi\right)+\vec{H}_\phi^s\left(r_a,\phi\right)=\vec{H}_\phi^t\left(r_a,\phi\right) \tag{2.9}$$

More explicitly, for the tangential electric and magnetic field on the boundary [21,22]

$$E_0\sum_{n=-\infty}^{+\infty} j^{-n}J_n\left(k_0r_a\right)e^{jn\phi} + E_0\sum_{n=-\infty}^{+\infty} j^{-n}a_nH_n^{(2)}\left(k_0r_a\right)e^{jn\phi} = E_0\sum_{n=-\infty}^{+\infty} j^{-n}b_nJ_n\left(k_1r_a\right)e^{jn\phi} \tag{2.10}$$

$$\begin{aligned}\frac{E_0}{j\eta_0}\sum_{n=-\infty}^{+\infty} j^{-n}J_n'\left(k_0r_a\right)e^{jn\phi} + \frac{E_0}{j\eta_0}\sum_{n=-\infty}^{+\infty} j^{-n}a_nH_n'^{(2)}\left(k_0r_a\right)e^{jn\phi} \\ = \frac{E_0}{j\eta_1}\sum_{n=-\infty}^{+\infty} j^{-n}b_nJ_n'\left(k_1r_a\right)e^{jn\phi}\end{aligned} \tag{2.11}$$

Taking advantage of the orthogonality of Bessel functions

$$E_0 j^{-n}J_n\left(k_0r_a\right)+E_0 j^{-n}a_nH_n^{(2)}\left(k_0r_a\right)=E_0 j^{-n}b_nJ_n\left(k_1r_a\right) \tag{2.12}$$

$$\frac{E_0}{\eta_0} j^{-n}J_n'\left(k_0r_a\right)+\frac{E_0}{\eta_0} j^{-n}a_nH_n'^{(2)}\left(k_0r_a\right)=\frac{E_0}{\eta_1} j^{-n}b_nJ_n'\left(k_1r_a\right) \tag{2.13}$$

Solving the equations (2.12) and (2.13), the unknown coefficients a_n and b_n

$$a_n = \frac{\eta_1 J_n'\left(k_0r_a\right)J_n\left(k_1r_a\right)-\eta_0 J_n\left(k_0r_a\right)J_n'\left(k_1r_a\right)}{\eta_0 J_n'\left(k_1r_a\right)H_n^{(2)}\left(k_0r_a\right)-\eta_1 J_n\left(k_1r_a\right)H_n'^{(2)}\left(k_0r_a\right)} \tag{2.14}$$

$$b_n = \eta_1\frac{J_n'\left(k_0r_a\right)H_n^{(2)}\left(k_0r_a\right)-J_n\left(k_0r_a\right)H_n'^{(2)}\left(k_0r_a\right)}{\eta_0 J_n'\left(k_1r_a\right)H_n^{(2)}\left(k_0r_a\right)-\eta_1 J_n\left(k_1r_a\right)H_n'^{(2)}\left(k_0r_a\right)} \tag{2.15}$$

The scattered E-field is calculated by using a_n coefficient. Large argument approximation of the Hankel function for far-field calculation [21, 22]

$$\lim_{k_0\rho\to\infty} H_0^{(2)}\left(k_0\rho\right) \cong \sqrt{\frac{2j}{k_0\pi}}\frac{e^{-jk_0\rho}}{\sqrt{\rho}} \tag{2.16}$$

Thus, the scattered E-field in the far zone

$$\vec{E}^s = \hat{z}E_0\sqrt{\frac{2j}{k_0\pi}}\frac{e^{-jk_0\rho}}{\sqrt{\rho}}\sum_{n=-\infty}^{+\infty} j^{-n}a_n e^{jn\phi} \tag{2.17}$$

2.3 Numerical Solution

Although there are exact solutions for scattering by cylinders of circular and elliptical cross-section, calculation of scattered fields from cylinders of arbitrary cross-section are obtained by numerical methods [23-25]. Here, to analyze the accuracy of the numerical solution, the surface equivalence principle and MoM are used for the same problem.

2.3.1 The Surface Equivalence Principle

In the surface equivalence principle, actual sources such as an antenna are replaced by equivalent sources [21-25]. The fields outside an imaginary closed surface are obtained by replacing the electric and magnetic equivalent currents radiating in unbounded media and satisfying the boundary conditions. If the currents are selected so that the fields inside the closed surface are zero or any other value and the field at an arbitrary point outside is determined, this is called external equivalence. In external equivalence principle, the whole space parameters are chosen as the parameters of the exterior medium. If the currents are selected so that the fields outside the closed surface are zero or any other value and the field at an arbitrary point inside is determined, this is called internal equivalence. In internal equivalence principle, the whole space parameters are chosen as the parameters of the interior medium [25].

2.3.1.1 **Theory**

The surface equivalence principle is used to solve the scattered E-field by a two-dimensional cylindrical object of arbitrary cross section as shown in Figure 2.2.

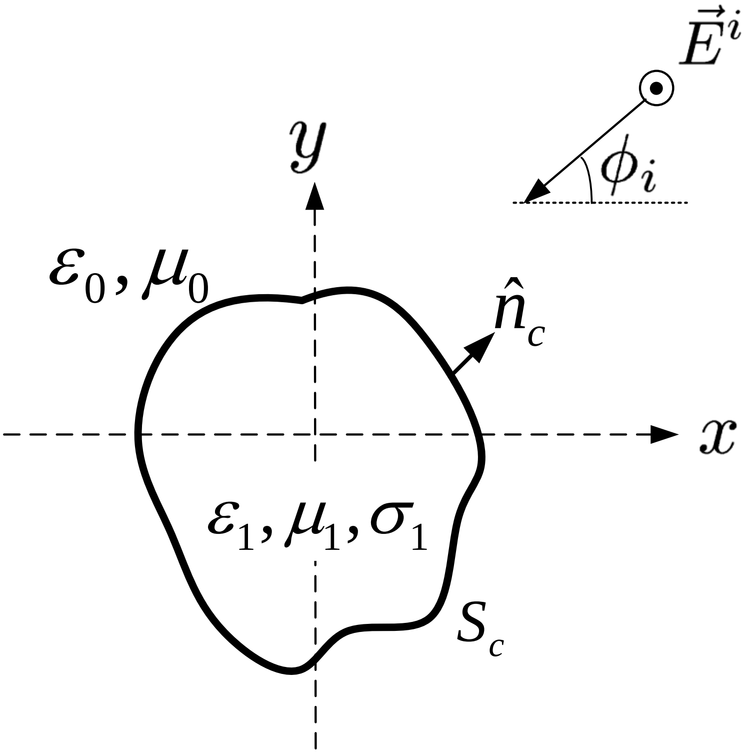

Figure 2. 2 An infinitely long cylindrical object of arbitrary cross-section.

In Figure 2.2, $\hat{n}_c$ is the outward unit normal vector to S_c. The incident field is a TM$_z$ plane wave with angle ϕ_i from the horizontal

$$\vec{E}^i\left(x,y\right)=\hat{z}\,E_0\,e^{jk_0\left(x\cos\phi_i+y\sin\phi_i\right)} \tag{2.18}$$

Figure 2.3 shows the external equivalence principle applied to the problem in Figure 2.2. The whole space parameters are chosen as $\left(\varepsilon_0,\mu_0\right)$ [26, 27]. The surface is replaced by surface electric $(\vec{J}_c)$ and magnetic $(\vec{M}_c)$ currents

$$\vec{J}_c=\hat{n}_c\times\vec{H}\Big|_{S_c^+} \tag{2.19}$$

$$\vec{M}_c=\vec{E}\Big|_{S_c^+}\times\hat{n}_c \tag{2.20}$$

At any point outside the surface, the total fields are $\vec{E}$ and $\vec{H}$. The total fields are zero under the surface

$$\vec{E}^s_{ext}\left(\vec{J}_c,\vec{M}_c\right)\Big|_{S_c^-}=\left(-\vec{E}^i\right)\Big|_{S_c^-} \tag{2.21}$$

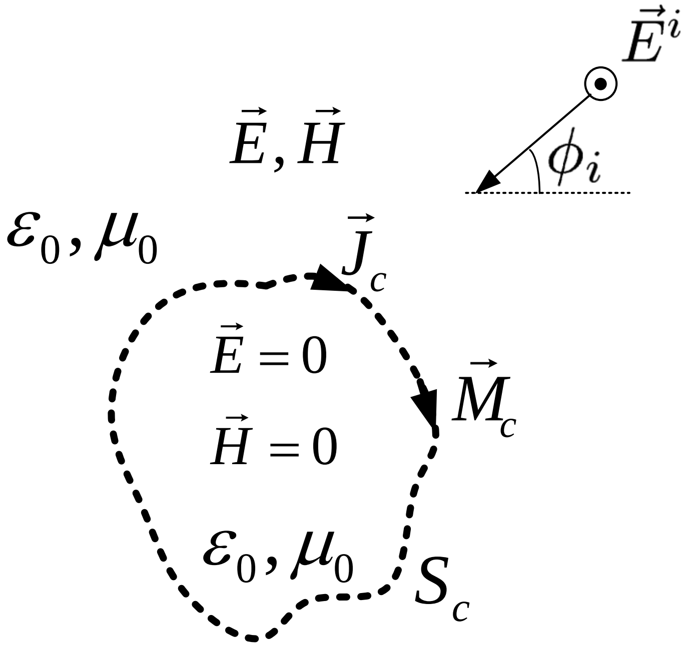

Figure 2. 3 The external equivalence principle applied to the problem in Figure 2.2.

Here, *ext* means external and S_c^- represents the surface just inside S_c. Then, the internal equivalence principle is applied in Figure 2.4 to the problem shown in Figure 2.2. Therefore, the whole space parameters are chosen as $(\varepsilon_1,\mu_1,\sigma_1)$ [26, 27]. The surface is replaced by $(-\vec{J}_c)$ and $(-\vec{M}_c)$. The total fields are zero at any point external to S_c

$$\vec{E}_{int}^{s}\left(-\vec{J}_c,-\vec{M}_c\right)\Big|_{S_c^+}=0 \tag{2.22}$$

Here, *int* means internal, and S_c^+ represents the surface just outside S_c.

In other words, there are two equations (2.21) and (2.22) to be solved by using MoM and two unknown currents to calculate the scattered field. The E-field is expressed in terms of electric and magnetic potential functions [23], and equations (2.21) and (2.22) can be rewritten as

$$-j\omega A_z^{ext}\left(\vec{J}_c\right)-\frac{1}{\varepsilon_0}\left[\nabla\times\vec{F}^{ext}\left(\vec{M}_c\right)\right]_z=-E_z^i,\ S_c^- \tag{2.23}$$

$$-j\omega A_z^{int}\left(-\vec{J}_c\right)-\frac{1}{\varepsilon_{c1}}\left[\nabla\times\vec{F}^{int}\left(-\vec{M}_c\right)\right]_z=0,\ S_c^+ \tag{2.24}$$

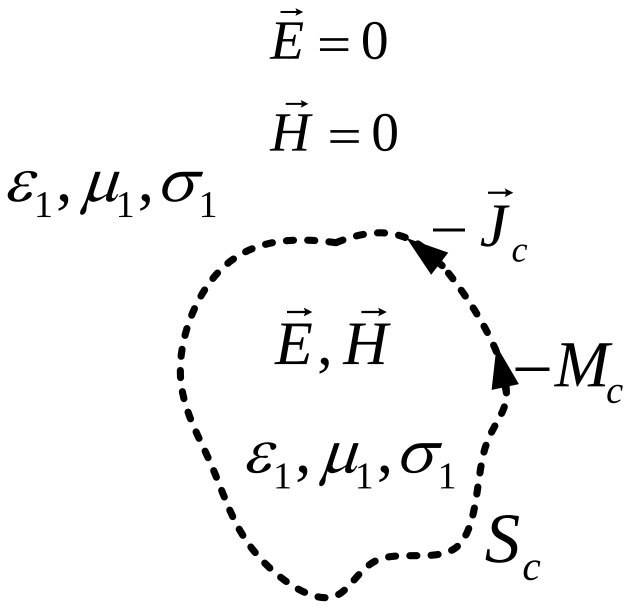

Figure 2. 4 The internal equivalence principle applied to the problem in Figure 2.2.

where $\vec{A}$ and $\vec{F}$ denote the magnetic and electric vector potential, respectively. They are given by the following line integrals

$$\vec{A}(\vec{\rho}) = \frac{\mu}{4j}\int_{C_j} \vec{J}(\vec{\rho}\,')H_0^{(2)}\left(k|\vec{\rho}-\vec{\rho}\,'|\right)dl' \tag{2.25}$$

$$\vec{F}(\vec{\rho}) = \frac{\varepsilon}{4j}\int_{C_m} \vec{M}(\vec{\rho}\,')H_0^{(2)}\left(k|\vec{\rho}-\vec{\rho}\,'|\right) dl' \tag{2.26}$$

where $\vec{\rho}\,'$ is a two-dimensional position vector for source points

$$\vec{\rho}\,' = x'\hat{x} + y'\hat{y} \tag{2.27}$$

The contours over $\vec{J}$ and $\vec{M}$ are C_j and C_m, respectively. The two equations (2.23) and (2.24) are solved numerically using MoM for two unknown surface currents ($\vec{J}_c, \vec{M}_c$).

2.3.1.2 **MoM Solution**

The currents on the surfaces of S_d and S_c are approximated by linear segments as shown in Figure 2.5.

$$\vec{J}_c(\vec{\rho}\,') = \hat{z}\sum_{i=1}^{N_c} I_i^c P_i^c(\vec{\rho}\,') \tag{2.28}$$

$$\vec{M}_c\left(\vec{\rho}'\right) = \sum_{i=1}^{N_c} \hat{\tau}_i K_i^c P_i^c\left(\vec{\rho}'\right) \tag{2.29}$$

where N_c is the number of segments on S_c. I_i^c and K_i^c are the unknown values of electric and magnetic current on the ith segment of S_c, respectively. The unit vector in the circumferential direction tangent to the ith segment of S_c is denoted by $\hat{\tau}_i$, and the unit vector in the z-direction is denoted by $\hat{z}$. Pulse functions (P^c) are chosen as the expansion functions and defined as unity on segment C_{ci}.

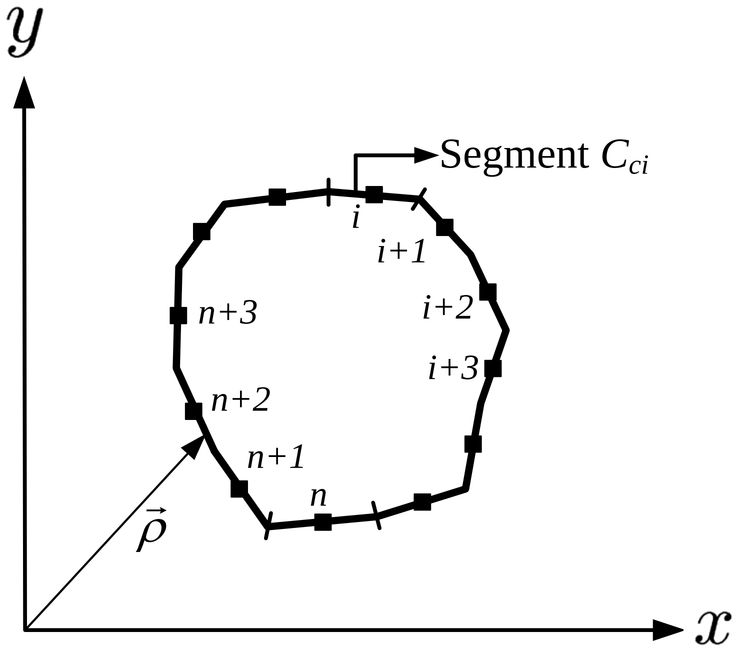

Figure 2. 5 Linear segmentation of the cylindrical object.

Using equation (2.26) and (2.29), it is explained in detail in Appendix A and can be shown that

$$\frac{1}{\varepsilon_0}\nabla\times\vec{F}^{ext}\left(\vec{M}_c\right) = \frac{jk_0}{4}\sum_{i=1}^{N_c} K_i^c \int_{C_{ci}} H_1^{(2)}\left(k_0\left|\vec{\rho}-\vec{\rho}'\right|\right)\frac{\hat{n}_i^c\cdot\left(\vec{\rho}-\vec{\rho}'\right)}{\left|\vec{\rho}-\vec{\rho}'\right|}dl' \tag{2.30}$$

Equations (2.23) and (2.24) can be rewritten using point matching at N_c points on the surface, the coupled EFIEs become

$$
\begin{aligned}
&-\frac{\omega\mu_0}{4}\sum_{i=1}^{N_c} I_i^c \int_{C_{ci}} H_0^{(2)}\left(k_0\left|\vec{\rho}-\vec{\rho}'\right|\right)dl' \\
&\qquad -\frac{jk_0}{4}\sum_{i=1}^{N_c} K_i^c \int_{C_{ci}} H_1^{(2)}\left(k_0\left|\vec{\rho}-\vec{\rho}'\right|\right)\frac{\hat{n}_i^c\cdot\left(\vec{\rho}-\vec{\rho}'\right)}{\left|\vec{\rho}-\vec{\rho}'\right|}dl' = -E_z^i,\ S_c^-
\end{aligned}
\tag{2.31}
$$

$$
\begin{aligned}
&\frac{\omega\mu_1}{4}\sum_{i=1}^{N_c} I_i^c \int_{C_{ci}} H_0^{(2)}\left(k_1\left|\vec{\rho}-\vec{\rho}'\right|\right)dl' \\
&\qquad +\frac{jk_1}{4}\sum_{i=1}^{N_c} K_i^c \int_{C_{ci}} H_1^{(2)}\left(k_1\left|\vec{\rho}-\vec{\rho}'\right|\right)\frac{\hat{n}_i^c\cdot\left(\vec{\rho}-\vec{\rho}'\right)}{\left|\vec{\rho}-\vec{\rho}'\right|}dl' = 0,\ S_c^+
\end{aligned}
\tag{2.32}
$$

where $H_0^{(2)}$ is the zeroth-order Hankel function of the second kind, and $H_1^{(2)}$ is the first-order Hankel function of the second kind. After pulse weighting functions are used to transform these EFIEs to linear equations, they can be written in matrix form

$$
\begin{bmatrix} Z_{C1} & Z_{M1} \\ Z_{C2} & Z_{M2} \end{bmatrix}\begin{bmatrix} I^c \\ K^c \end{bmatrix} = \begin{bmatrix} V_c \\ 0 \end{bmatrix}
\tag{2.33}
$$

Here, Z_{C1}, Z_{C2}, Z_{M1}, and Z_{M2} are the square sub matrixes of $N_c \times N_c$. The element in the *i*th row and the *n*th column of these matrixes is equal to the E-field at the midpoint of the *n*th segment of S_c, produced by electric and magnetic currents lying on the *i*th segment of S_c. The left hand side of the equation is the column sub vectors containing the unknown expansion coefficients. The right hand side of the equation contains the incident field on S_c. The *i*th element of V_c is the incident field at the middle of the *i*th segment of S_c.

The self terms $\left(\vec{\rho}=\vec{\rho}'\right)$ should be calculated carefully, because the argument of the Hankel functions becomes very small and the integration of the Hankel function becomes difficult to compute numerically. Therefore, the self-terms should be approximated by using the Hankel function terms for small arguments [28] as shown in Appendix B.

$$
\int_{C_{ci}} H_0^{(2)}\left(k\ \left|\vec{\rho}-\vec{\rho}'\right|\right)dl' \cong \Delta^c\left[1-j\frac{2}{\pi}\left(\ln\left(\frac{k\gamma}{4}\Delta^c\right)-1\right)\right]
\tag{2.34}
$$

$$
\int_{C_{ci}} H_1^{(2)}\left(k\ \left|\vec{\rho}-\vec{\rho}'\right|\right)\frac{\hat{n}_i^c\cdot\left(\vec{\rho}-\vec{\rho}'\right)}{\left|\vec{\rho}-\vec{\rho}'\right|}dl' \cong \frac{2j}{k}
\tag{2.35}
$$

where Δ^c is the length of the segment on S_c and $\gamma = 1.781$.

The unknown expansion coefficients are solved and the far scattered field can be computed by using $\vec{J}_c$ and $\vec{M}_c$

$$\begin{aligned} E_z^s = & -\frac{\omega\mu_0}{4}\sqrt{\frac{2j}{k_0\pi}}\frac{e^{-jk_0\rho}}{\sqrt{\rho}}\sum_{i=1}^{N_c} I_i^c e^{-jk_0\left(x'\cos\phi_s + y'\sin\phi_s\right)}\Delta_i^c \\ & + \frac{jk_0}{4}\sqrt{\frac{2j}{k_0\pi}}\frac{e^{-jk_0\rho}}{\sqrt{\rho}}\sum_{i=1}^{N_c} K_i^c e^{-jk_0\left(x'\cos\phi_s + y'\sin\phi_s\right)}\Delta_i^c \end{aligned} \tag{2.36}$$

where ϕ_s is the scattering angle.

2.4 Numerical Results

In the two-dimensional case, the scattering radar cross section is given by [29]

$$\sigma\left(\phi_s\right) = \lim_{\rho\to\infty} 2\pi\rho\left|\frac{E_z^s\left(\rho,\phi_s\right)}{E_z^i}\right|^2 \tag{2.37}$$

Figure 2.6 shows the scattering cross section of a circular dielectric cylinder calculated by both analytical and numerical methods. There are three different numerical results obtained by changing the points per free-space wavelength (ppw) used to represent the currents on the object. In figures, free-space wavelength is indicated by (λ_0). As it is seen that the ppw increases, there is an excellent agreement between the analytical and numerical solutions.

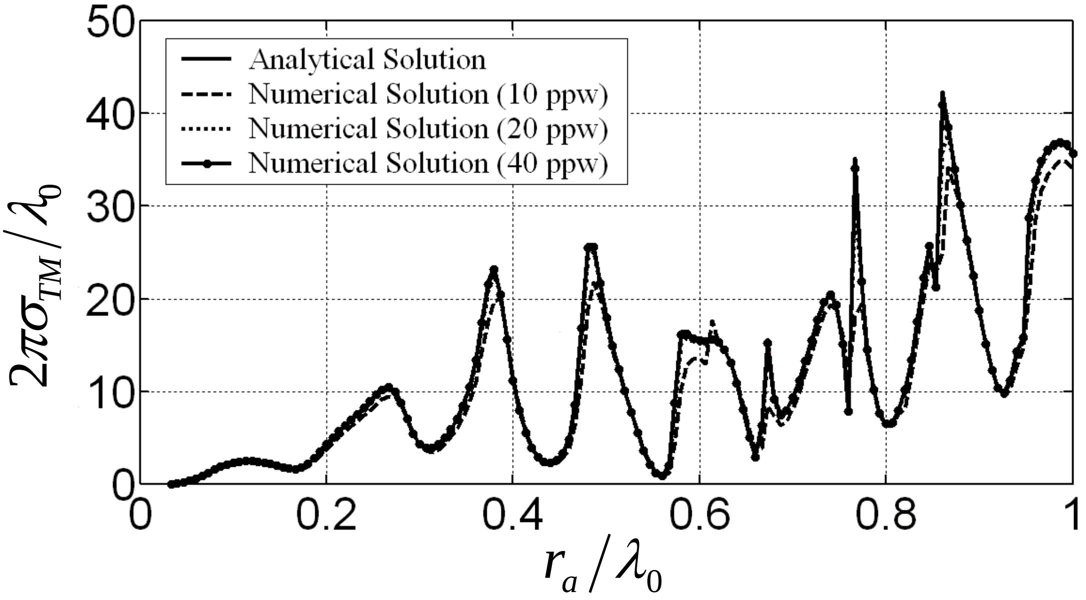

Figure 2. 6 Scattering cross section of a circular dielectric cylinder for $f = 1$ GHz, $\phi_i = \phi_s = 20^\circ$, $\varepsilon_1 = 4\varepsilon_0$ F/m, $\mu_1 = \mu_0$ H/m and $\sigma_1 = 0.0$ Sm^{-1}.

CHAPTER 3

COMPUTATION OF TM$_z$ SCATTERING FROM A CYLINDRICAL OBJECT COATED WITH A DIELECTRIC MATERIAL

3.1 Introduction

In this chapter, the problem of electromagnetic scattering from a two-dimensional cylinder of arbitrary cross section coated with a dielectric material is considered. First, the analytical and numerical solutions of the problem relating to the conducting cylindrical object coated with a dielectric material are given, and then computed results of these two solutions are compared for the case of circular cross-section. Then, these steps are also applied for the problem relating to the dielectric cylindrical object coated with a dielectric material.

3.2 Scattering from a Conducting Cylindrical Object Coated with a Dielectric Material

3.2.1 Analytical Solution

The scattered E-field from a conducting cylindrical object coated with a dielectric material is calculated by expressing the plane waves by cylindrical wave functions. As shown in Figure 3.1, conducting and dielectric objects have circular cross-section. The radius and the surface of the coated cylinder are r_b and S_d; respectively.

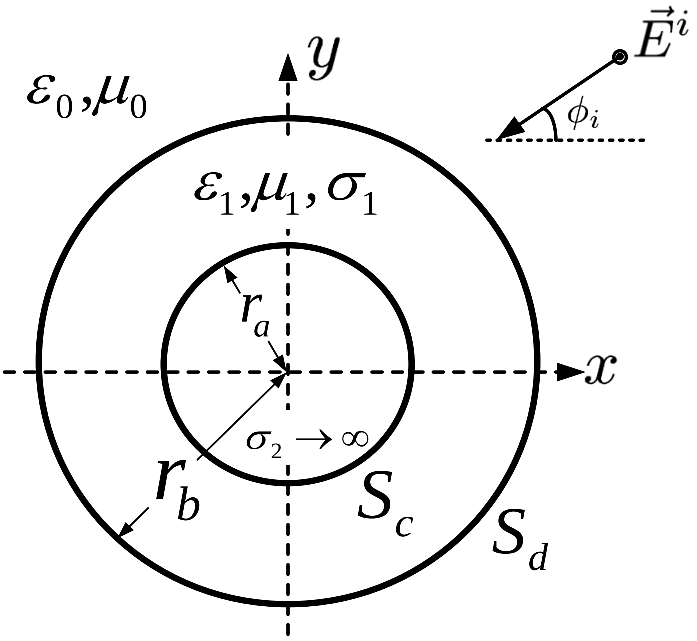

Figure 3. 1 A conducting cylindrical object of circular cross-section coated with a dielectric cylindrical object of circular cross-section

As mentioned in chapter 2, the incident E-field [21, 22]

$$\vec{E}^i = \hat{z}E_z^i = \hat{z}E_0 \sum_{n=-\infty}^{+\infty} j^{-n} J_n\left(k_0\rho\right) e^{jn\phi} \tag{3.1}$$

The scattered E-field in the region exterior to the dielectric cylinder

$$\vec{E}^s = \hat{z}E_0 \sum_{n=-\infty}^{+\infty} j^{-n} a_n H_n^{(2)}\left(k_0\rho\right) e^{jn\phi} \tag{3.2}$$

and the total field in the dielectric cylinder

$$\vec{E}^t = \hat{z}E_0 \sum_{n=-\infty}^{+\infty} j^{-n} b_n J_n\left(k_1\rho\right) e^{jn\phi} + \hat{z}E_0 \sum_{n=-\infty}^{+\infty} j^{-n} c_n Y_n\left(k_1\rho\right) e^{jn\phi} \tag{3.3}$$

The magnetic field can be computed from the E-field, and therefore [21, 22]

$$\vec{H}^i = -\frac{1}{j\omega\mu_0} \nabla \times \vec{E}^i = \hat{\phi}\frac{E_0}{j\eta_0} \sum_{n=-\infty}^{+\infty} j^{-n} J_n'\left(k_0\rho\right) e^{jn\phi} \tag{3.4}$$

$$\vec{H}^s = -\frac{1}{j\omega\mu_0} \nabla \times \vec{E}^s = \hat{\phi}\frac{E_0}{j\eta_0} \sum_{n=-\infty}^{+\infty} j^{-n} a_n H_n'^{(2)}\left(k_0\rho\right) e^{jn\phi} \tag{3.5}$$

$$\vec{H}^t = -\frac{1}{j\omega\mu_1} \nabla \times \vec{E}^t = \hat{\phi}\frac{E_0}{j\eta_1} \sum_{n=-\infty}^{+\infty} j^{-n} b_n J_n'\left(k_1\rho\right) e^{jn\phi} + \hat{\phi}\frac{E_0}{j\eta_1} \sum_{n=-\infty}^{+\infty} j^{-n} b_n Y_n'\left(k_1\rho\right) e^{jn\phi} \tag{3.6}$$

The unknown coefficients a_n, b_n and c_n can be found by applying the boundary condition of

$$\vec{E}_z^i\left(r_b,\phi\right)+\vec{E}_z^s\left(r_b,\phi\right)=\vec{E}_z^t\left(r_b,\phi\right) \tag{3.7}$$

$$\vec{H}_\phi^i\left(r_b,\phi\right)+\vec{H}_\phi^s\left(r_b,\phi\right)=\vec{H}_\phi^t\left(r_b,\phi\right) \tag{3.8}$$

$$\vec{E}_\phi^t\left(r_a,\phi\right)=0 \tag{3.9}$$

More explicitly, for the tangential electric and magnetic field on the boundary [21, 22]

$$\begin{aligned} E_0\sum_{n=-\infty}^{+\infty} j^{-n}J_n\left(k_0r_b\right)e^{jn\phi}+E_0\sum_{n=-\infty}^{+\infty} j^{-n}a_nH_n^{(2)}\left(k_0r_b\right)e^{jn\phi} &= E_0\sum_{n=-\infty}^{+\infty} j^{-n}b_nJ_n\left(k_1r_b\right)e^{jn\phi} \\ &+E_0\sum_{n=-\infty}^{+\infty} j^{-n}c_nY_n\left(k_1r_b\right)e^{jn\phi} \end{aligned} \tag{3.10}$$

$$\begin{aligned} \frac{E_0}{j\eta_0}\sum_{n=-\infty}^{+\infty} j^{-n}J_n'\left(k_0r_b\right)e^{jn\phi}+\frac{E_0}{j\eta_0}\sum_{n=-\infty}^{+\infty} j^{-n}a_nH_n'^{(2)}\left(k_0r_b\right)e^{jn\phi} &= \\ \frac{E_0}{j\eta_1}\sum_{n=-\infty}^{+\infty} j^{-n}b_nJ_n'\left(k_1r_b\right)e^{jn\phi}+\frac{E_0}{j\eta_1}\sum_{n=-\infty}^{+\infty} j^{-n}b_nY_n'\left(k_1r_b\right)e^{jn\phi} \end{aligned} \tag{3.11}$$

$$E_0\sum_{n=-\infty}^{+\infty} j^{-n}b_nJ_n\left(k_1r_a\right)e^{jn\phi}+E_0\sum_{n=-\infty}^{+\infty} j^{-n}c_nY_n\left(k_1r_a\right)e^{jn\phi}=0 \tag{3.12}$$

Taking advantage of the orthogonality of Bessel functions

$$E_0j^{-n}J_n\left(k_0r_b\right)+E_0j^{-n}a_nH_n^{(2)}\left(k_0r_b\right)=E_0j^{-n}b_nJ_n\left(k_1r_b\right)+E_0j^{-n}c_nY_n\left(k_1r_b\right) \tag{3.13}$$

$$\frac{E_0}{\eta_0}j^{-n}J_n'\left(k_0r_b\right)+\frac{E_0}{\eta_0}j^{-n}a_nH_n'^{(2)}\left(k_0r_b\right)=\frac{E_0}{\eta_1}j^{-n}b_nJ_n'\left(k_1r_b\right)+\frac{E_0}{\eta_1}j^{-n}c_nY_n'\left(k_1r_b\right) \tag{3.14}$$

$$E_0j^{-n}b_nJ_n\left(k_1r_a\right)+E_0j^{-n}c_nY_n\left(k_1r_a\right)=0$$

(3.15)

Solving the equations (3.13), (3.14) and (3.15), the unknown coefficients a_n, b_n and c_n are calculated and the scattered E-field is calculated by using a_n coefficient [21, 22]

$$\vec{E}^s=\hat{z}E_0\sqrt{\frac{2j}{k_0\pi}}\frac{e^{-jk_0\rho}}{\sqrt{\rho}}\sum_{n=-\infty}^{+\infty} j^{-n}a_ne^{jn\phi} \tag{3.16}$$

3.2.2 Numerical Solution

To analyze the accuracy of numerical solution of this problem, the surface equivalence principle and MoM are used.

3.2.2.1 Theory

The surface equivalence principle is used to find the total field at an external point of the problem shown in Figure 3.2. It has two steps containing two equivalent and simpler problems. Figure 3.3 shows the external equivalence problem. The whole space parameters are chosen as (ε_0, μ_0). The surface is replaced the equivalent surface electric current by $\vec{J}_d$ and the equivalent surface magnetic current $\vec{M}_d$ [26, 27]

$$\vec{J}_d = \hat{n}_d \times \vec{H}\Big|_{S_d^+} \tag{3.17}$$

$$\vec{M}_d = \vec{E}\Big|_{S_d^+} \times \hat{n}_d \tag{3.18}$$

where $\hat{n}_d$ is the outward unit normal vector to S_d.

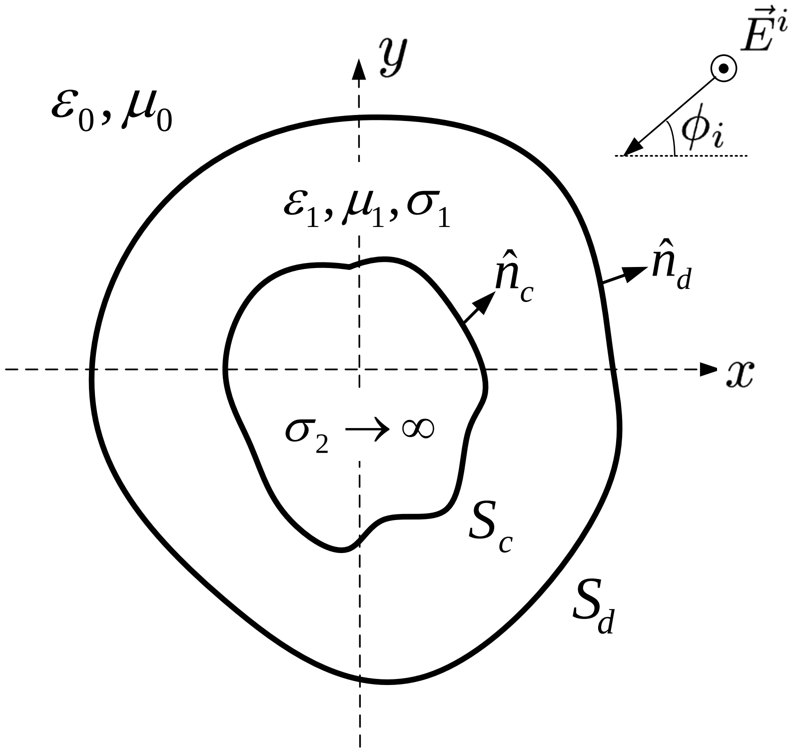

Figure 3. 2 An infinitely long conducting cylindrical object of arbitrary cross-section coated with a dielectric cylindrical object of arbitrary cross-section

At any point outside the surface, the total fields are $\vec{E}$ and $\vec{H}$. The total field is zero inside S_d denoted S_d^-

$$\vec{E}^s_{ext}\left(\vec{J}_d,\vec{M}_d\right)\Big|_{S_d^-}=\left(-\vec{E}^i\right)\Big|_{S_d^-} \tag{3.19}$$

Figure 3.4 shows the internal equivalence problem. The whole space parameters are chosen as $(\varepsilon_1,\mu_1,\sigma_1)$. The total field is zero on both S_d^+ and S_c^-

$$\vec{E}^s_{int}\left(-\vec{J}_d,-\vec{M}_d,\vec{J}_c\right)\Big|_{S_d^+}=0 \tag{3.20}$$

$$\vec{E}^s_{int}\left(-\vec{J}_d,-\vec{M}_d,\vec{J}_c\right)\Big|_{S_c^-}=0 \tag{3.21}$$

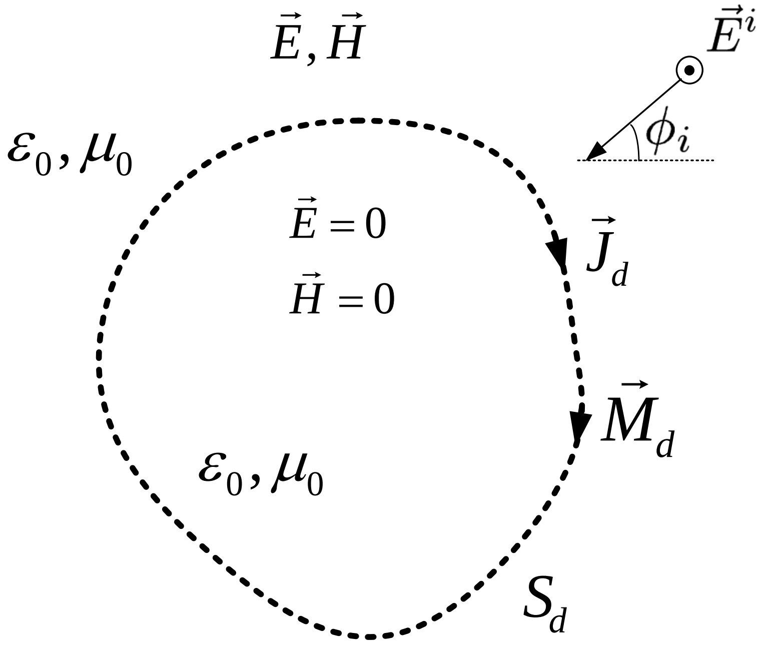

Figure 3. 3 The external equivalence principle applied to the problem in Figure 3.2.

where S_d^+ represents the surface just outside S_d.

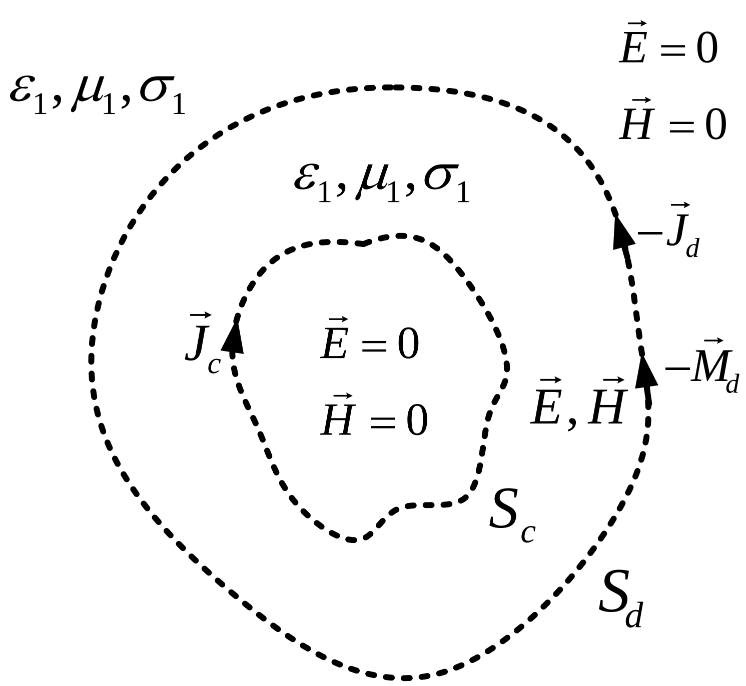

Figure 3. 4 The internal equivalence principle applied to the problem in Figure 3.2.

In other words, there are three equations (3.19), (3.20) and (3.21) to be solved by using MoM and three unknown currents to calculate the scattered field. The E-field is expressed in terms of electric and magnetic potential functions, and equations (3.19), (3.20) and (3.21) can be rewritten as [26, 27]

$$-j\omega A_z^{ext}\left(\vec{J}_d\right)-\frac{1}{\varepsilon_0}\left[\nabla\times\vec{F}^{ext}\left(\vec{M}_d\right)\right]_z=-E_z^i,\ S_d^- \tag{3.22}$$

$$-j\omega A_z^{int}\left(-\vec{J}_d\right)-\frac{1}{\varepsilon_{c1}}\left[\nabla\times\vec{F}^{int}\left(-\vec{M}_d\right)\right]_z-j\omega A_z^{int}\left(\vec{J}_c\right)=0,\ S_d^+ \tag{3.23}$$

$$-j\omega A_z^{int}\left(-\vec{J}_d\right)-\frac{1}{\varepsilon_{c1}}\left[\nabla\times\vec{F}^{int}\left(-\vec{M}_d\right)\right]_z-j\omega A_z^{int}\left(\vec{J}_c\right)=0,\ S_c^- \tag{3.24}$$

Three equations (3.22)-(3.24) are solved numerically using MoM for three unknown surface currents ($\vec{J}_d,\vec{M}_d,\vec{J}_c$).

3.2.3 MoM Solution

The currents on the surfaces of S_d and S_c are approximated by linear segments [26, 27]

$$\vec{J}_d\left(\vec{\rho}'\right)=\hat{z}\sum_{i=1}^{N_d}I_i^dP_i^d\left(\vec{\rho}'\right) \tag{3.25}$$

$$\vec{M}_d(\vec{\rho}') = \sum_{i=1}^{N_d} \hat{\tau}_i K_i^d P_i^d(\vec{\rho}') \tag{3.26}$$

$$\vec{J}_c(\vec{\rho}') = \hat{z}\sum_{i=1}^{N_c} I_i^c P_i^c(\vec{\rho}') \tag{3.27}$$

where N_d is the number of segments on S_d. I_i^d and K_i^d are the unknown values of electric and magnetic current on the ith segment of S_d, respectively.

Equations (3.22)-(3.24) can be rewritten using equations (3.25)-(3.27)

$$\begin{aligned} &-\frac{\omega\mu_0}{4}\sum_{i=1}^{N_d} I_i^d \int_{C_{di}} H_0^{(2)}\left(k_0|\vec{\rho}-\vec{\rho}'|\right)dl' \\ &\qquad -\frac{jk_0}{4}\sum_{i=1}^{N_d} K_i^d \int_{C_{di}} H_1^{(2)}\left(k_0|\vec{\rho}-\vec{\rho}'|\right)\frac{\hat{n}_i^d\cdot(\vec{\rho}-\vec{\rho}')}{|\vec{\rho}-\vec{\rho}'|}dl' = -E_z^i,\ S_d^- \end{aligned} \tag{3.28}$$

$$\begin{aligned} &\frac{\omega\mu_1}{4}\sum_{i=1}^{N_d} I_i^d \int_{C_{di}} H_0^{(2)}\left(k_1|\vec{\rho}-\vec{\rho}'|\right)dl' \\ &\qquad +\frac{jk_1}{4}\sum_{i=1}^{N_d} K_i^d \int_{C_{di}} H_1^{(2)}\left(k_1|\vec{\rho}-\vec{\rho}'|\right)\frac{\hat{n}_i^d\cdot(\vec{\rho}-\vec{\rho}')}{|\vec{\rho}-\vec{\rho}'|}dl' \\ &\qquad\qquad +\frac{\omega\mu_1}{4}\sum_{i=1}^{N_c} I_i^c \int_{C_{ci}} H_0^{(2)}\left(k_1|\vec{\rho}-\vec{\rho}'|\right)dl' = 0,\ S_d^+ \end{aligned} \tag{3.29}$$

$$\begin{aligned} &\frac{\omega\mu_1}{4}\sum_{i=1}^{N_d} I_i^d \int_{C_{di}} H_0^{(2)}\left(k_1|\vec{\rho}-\vec{\rho}'|\right)dl' \\ &\qquad +\frac{jk_1}{4}\sum_{i=1}^{N_d} K_i^d \int_{C_{di}} H_1^{(2)}\left(k_1|\vec{\rho}-\vec{\rho}'|\right)\frac{\hat{n}_i^d\cdot(\vec{\rho}-\vec{\rho}')}{|\vec{\rho}-\vec{\rho}'|}dl' \\ &\qquad\qquad +\frac{\omega\mu_1}{4}\sum_{i=1}^{N_c} I_i^c \int_{C_{ci}} H_0^{(2)}\left(k_1|\vec{\rho}-\vec{\rho}'|\right)dl' = 0,\ S_c^- \end{aligned} \tag{3.30}$$

where C_d is the contour representing of S_d.

The unknown expansion coefficients are solved and the far scattered field can be computed using $\vec{J}_d$ and $\vec{M}_d$

$$E_z^s = -\frac{\omega\mu_0}{4}\sqrt{\frac{2j}{k_0\pi}}\frac{e^{-jk_0\rho}}{\sqrt{\rho}}\sum_{i=1}^{N_d} I_i^d e^{-jk_0\left(x'\cos\phi_s + y'\sin\phi_s\right)}\Delta_i^d + \frac{jk_0}{4}\sqrt{\frac{2j}{k_0\pi}}\frac{e^{-jk_0\rho}}{\sqrt{\rho}}\sum_{i=1}^{N_d} K_i^d e^{-jk_0\left(x'\cos\phi_s + y'\sin\phi_s\right)}\Delta_i^d \tag{3.31}$$

where Δ^d is the length of the segment on S_d.

3.3 Scattering from a Dielectric Cylindrical Object Coated with a Dielectric Material

3.3.1 Analytical Solution

As shown in Figure 3.5, both of the dielectric objects have circular cross-section. The incident fields, the scattered fields in the region exterior to the cylinder having radius r_b, and the total fields in the cylinder having radius r_b are calculated by expressing the plane waves by cylindrical wave functions as shown in equations (3.1)-(3.6).

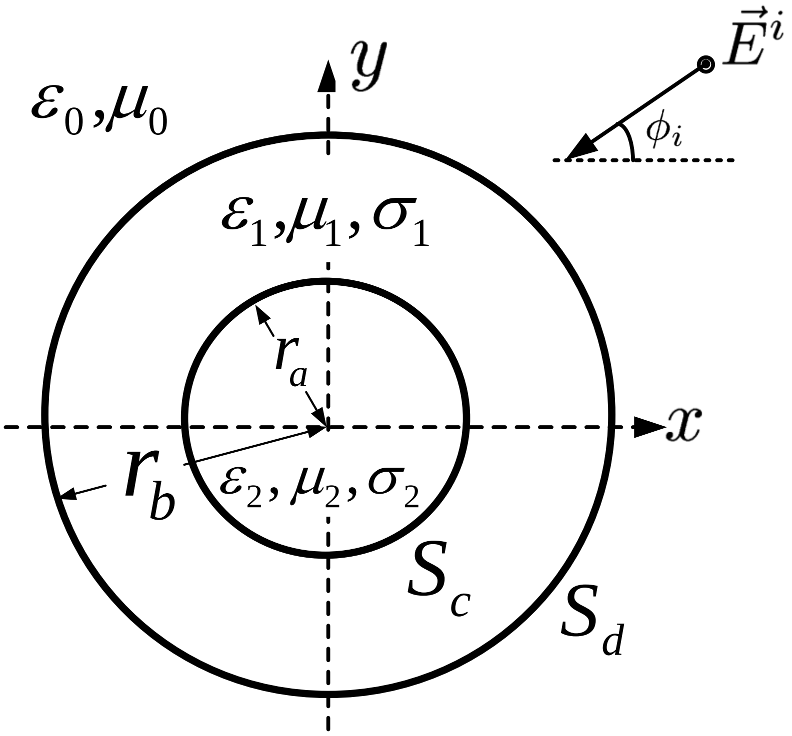

Figure 3. 5 A dielectric cylindrical object of circular cross-section coated with a dielectric cylindrical object of circular cross-section

The total field in the cylinder having radius r_a [21, 22]

$$\vec{E}^{t2} = \hat{z}E_0 \sum_{n=-\infty}^{+\infty} j^{-n} d_n J_n\left(k_2\rho\right) e^{jn\phi} \tag{3.32}$$

The magnetic field can be computed from the E-field, and therefore

$$\vec{H}^{t2} = -\frac{1}{j\omega\mu_2} \nabla \times \vec{E}^{t2} = \hat{\phi}\frac{E_0}{j\eta_2} \sum_{n=-\infty}^{+\infty} j^{-n} d_n J_n'\left(k_2\rho\right) e^{jn\phi} \tag{3.33}$$

The unknown coefficients a_n, b_n, c_n and d_n can be found by applying the boundary condition of

$$\vec{E}_z^{i}\left(r_b,\phi\right) + \vec{E}_z^{s}\left(r_b,\phi\right) = \vec{E}_z^{t1}\left(r_b,\phi\right) \tag{3.34}$$

$$\vec{H}_\phi^{i}\left(r_b,\phi\right) + \vec{H}_\phi^{s}\left(r_b,\phi\right) = \vec{H}_\phi^{t1}\left(r_b,\phi\right) \tag{3.35}$$

$$\vec{E}_\phi^{t1}\left(r_b,\phi\right) = \vec{E}_\phi^{t2}\left(r_a,\phi\right) \tag{3.36}$$

$$\vec{H}_\phi^{t1}\left(r_b,\phi\right) = \vec{H}_\phi^{t2}\left(r_a,\phi\right) \tag{3.37}$$

More explicitly, for the tangential electric and magnetic field on the boundary [21, 22]

$$\begin{aligned} E_0 \sum_{n=-\infty}^{+\infty} j^{-n} J_n\left(k_0 r_b\right) e^{jn\phi} + E_0 \sum_{n=-\infty}^{+\infty} j^{-n} a_n H_n^{(2)}\left(k_0 r_b\right) e^{jn\phi} \\ = E_0 \sum_{n=-\infty}^{+\infty} j^{-n} b_n J_n\left(k_1 r_b\right) e^{jn\phi} + E_0 \sum_{n=-\infty}^{+\infty} j^{-n} c_n Y_n\left(k_1 r_b\right) e^{jn\phi} \end{aligned} \tag{3.38}$$

$$\begin{aligned} \frac{E_0}{j\eta_0} \sum_{n=-\infty}^{+\infty} j^{-n} J_n'\left(k_0 r_b\right) e^{jn\phi} + \frac{E_0}{j\eta_0} \sum_{n=-\infty}^{+\infty} j^{-n} a_n H_n'^{(2)}\left(k_0 r_b\right) e^{jn\phi} \\ = \frac{E_0}{j\eta_1} \sum_{n=-\infty}^{+\infty} j^{-n} b_n J_n'\left(k_1 r_b\right) e^{jn\phi} + \frac{E_0}{j\eta_1} \sum_{n=-\infty}^{+\infty} j^{-n} b_n Y_n'\left(k_1 r_b\right) e^{jn\phi} \end{aligned} \tag{3.39}$$

$$\begin{aligned} E_0 \sum_{n=-\infty}^{+\infty} j^{-n} b_n J_n\left(k_1 r_a\right) e^{jn\phi} + E_0 \sum_{n=-\infty}^{+\infty} j^{-n} c_n Y_n\left(k_1 r_a\right) e^{jn\phi} \\ = E_0 \sum_{n=-\infty}^{+\infty} j^{-n} d_n J_n\left(k_2 r_a\right) e^{jn\phi} \end{aligned} \tag{3.40}$$

$$\frac{E_0}{j\eta_1}\sum_{n=-\infty}^{+\infty} j^{-n} b_n J_n'\left(k_1 r_a\right) e^{jn\phi} + \frac{E_0}{j\eta_1}\sum_{n=-\infty}^{+\infty} j^{-n} c_n Y_n'\left(k_1 r_a\right) e^{jn\phi} = \frac{E_0}{j\eta_2}\sum_{n=-\infty}^{+\infty} j^{-n} d_n J_n'\left(k_2 r_a\right) e^{jn\phi} \tag{3.41}$$

Taking advantage of the orthogonality of Bessel functions

$$E_0 j^{-n} J_n\left(k_0 r_b\right) + E_0 j^{-n} a_n H_n^{(2)}\left(k_0 r_b\right) = E_0 j^{-n} b_n J_n\left(k_1 r_b\right) + E_0 j^{-n} c_n Y_n\left(k_1 r_b\right) \tag{3.42}$$

$$\frac{E_0}{\eta_0} j^{-n} J_n'\left(k_0 r_b\right) + \frac{E_0}{\eta_0} j^{-n} a_n H_n'^{(2)}\left(k_0 r_b\right) = \frac{E_0}{\eta_1} j^{-n} b_n J_n'\left(k_1 r_b\right) + \frac{E_0}{\eta_1} j^{-n} c_n Y_n'\left(k_1 r_b\right) \tag{3.43}$$

$$E_0 j^{-n} b_n J_n\left(k_1 r_a\right) + E_0 j^{-n} c_n Y_n\left(k_1 r_a\right) = E_0 j^{-n} d_n J_n\left(k_2 r_a\right) \tag{3.44}$$

$$\frac{E_0}{\eta_1} j^{-n} b_n J_n'\left(k_1 r_a\right) + \frac{E_0}{\eta_1} j^{-n} c_n Y_n'\left(k_1 r_a\right) = \frac{E_0}{\eta_2} j^{-n} d_n J_n'\left(k_2 r_a\right) \tag{3.45}$$

Solving the equations (3.42)-(3.45), the unknown coefficients a_n, b_n, c_n and d_n are calculated and the scattered E-field is calculated by using a_n coefficient and equation 3.16.

3.3.2 Numerical Solution

The surface equivalence principle and MoM are used to solve this problem numerically.

3.3.2.1 Theory

The surface equivalence principle is used to find the total field at an external point of the problem shown in Figure 3.6.

Figure 3.7 shows the external equivalence principle applied to the problem in Figure 3.6. The total fields are zero under the surface

$$\vec{E}_{ext}^{s}\left(\vec{J}_d, \vec{M}_d\right)\Big|_{S_d^-} = \left(-\vec{E}^i\right)\Big|_{S_d^-} \tag{3.46}$$

Figure 3.8 shows the internal equivalence problem. The total field is zero on both S_d^+ and S_c^-

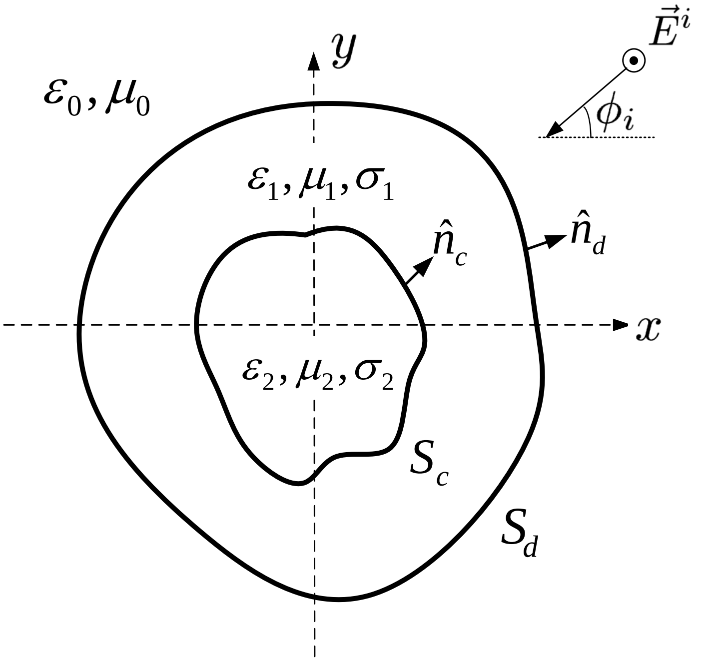

Figure 3. 6 An infinitely long dielectric cylindrical object of arbitrary cross-section coated with a dielectric cylindrical object of arbitrary cross-section

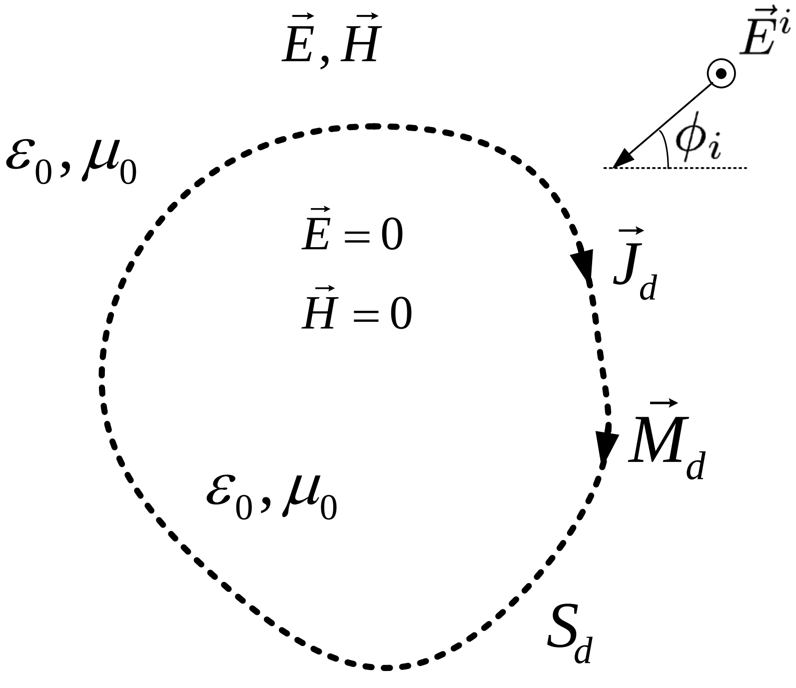

Figure 3. 7 The external equivalence principle applied to the problem in Figure 3.6.

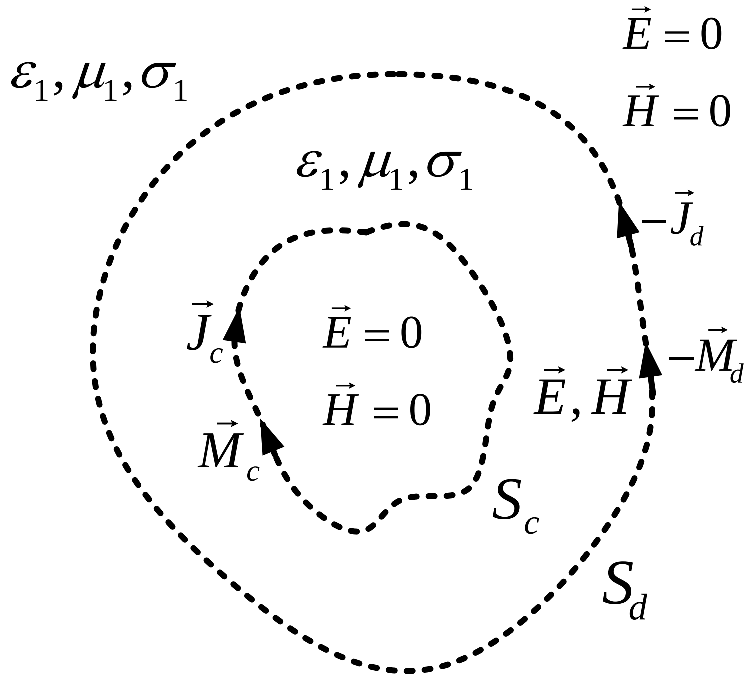

Figure 3. 8 The internal equivalence principle applied to the problem in Figure 3.6.

$$\vec{E}^{s}_{int}\left(-\vec{J}_d,-\vec{M}_d,\vec{J}_c,\vec{M}_c\right)\Big|_{S_d^+}=0 \tag{3.47}$$

$$\vec{E}^{s}_{int}\left(-\vec{J}_d,-\vec{M}_d,\vec{J}_c,\vec{M}_c\right)\Big|_{S_c^-}=0 \tag{3.48}$$

Figure 3.9 shows the internal equivalence problem for the points inside of the cylinder. The total field is zero on both S_c^+ that represents the surface just outside S_c .

$$\vec{E}^{s}_{int}\left(-\vec{J}_c,-\vec{M}_c\right)\Big|_{S_c^+}=0 \tag{3.49}$$

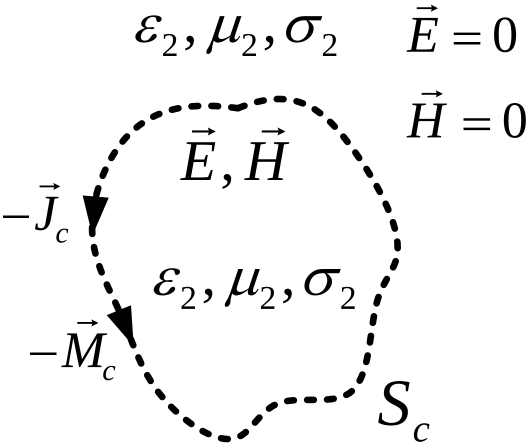

Figure 3. 9 The internal equivalence principle for the points inside of the cylinder applied to the problem in Figure 3.6.

In other words, there are four equations (3.46)-(3.49) to be solved by using MoM and four unknown currents to calculate the scattered field. The E-field is expressed in terms of electric and magnetic potential functions, and equations (3.46)-(3.49) can be rewritten as [26, 27]

$$-j\omega A_z^{ext}\left(\vec{J}_d\right)-\frac{1}{\varepsilon_0}\left[\nabla\times\vec{F}^{ext}\left(\vec{M}_d\right)\right]_z=-E_z^i,\ S_d^- \tag{3.50}$$

$$-j\omega A_z^{int}\left(-\vec{J}_d\right)-\frac{1}{\varepsilon_{c1}}\left[\nabla\times\vec{F}^{int}\left(-\vec{M}_d\right)\right]_z \\ -j\omega A_z^{int}\left(\vec{J}_c\right)-\frac{1}{\varepsilon_{c1}}\left[\nabla\times\vec{F}^{int}\left(-\vec{M}_c\right)\right]_z=0,\ S_d^+ \tag{3.51}$$

$$-j\omega A_z^{int}\left(-\vec{J}_d\right)-\frac{1}{\varepsilon_{c1}}\left[\nabla\times\vec{F}^{int}\left(-\vec{M}_d\right)\right]_z \\ -j\omega A_z^{int}\left(\vec{J}_c\right)-\frac{1}{\varepsilon_{c1}}\left[\nabla\times\vec{F}^{int}\left(-\vec{M}_c\right)\right]_z=0,\ S_c^- \tag{3.52}$$

$$-j\omega A_z^{int}\left(\vec{J}_c\right)-\frac{1}{\varepsilon_{c2}}\left[\nabla\times\vec{F}^{int}\left(-\vec{M}_c\right)\right]_z=0,\ S_c^+ \tag{3.53}$$

where $\varepsilon_{c2}=\varepsilon_2\left(1-j\frac{\sigma_2}{\omega\varepsilon_2}\right)$. Four equations (3.51)-(3.54) are solved numerically using MoM for four unknown surface currents ($\vec{J}_d,\vec{M}_d,\vec{J}_c,\vec{M}_c$).

3.3.3 MoM Solution

The currents on the surfaces of S_d and S_c are approximated by linear segments [26, 27]

$$\vec{J}_d\left(\vec{\rho}'\right)=\hat{z}\sum_{i=1}^{N_d}I_i^dP_i^d\left(\vec{\rho}'\right) \tag{3.54}$$

$$\vec{M}_d\left(\vec{\rho}'\right)=\sum_{i=1}^{N_d}\hat{\tau}_iK_i^dP_i^d\left(\vec{\rho}'\right) \tag{3.55}$$

$$\vec{J}_c\left(\vec{\rho}'\right)=\hat{z}\sum_{i=1}^{N_c}I_i^cP_i^c\left(\vec{\rho}'\right) \tag{3.56}$$

$$\vec{M}_c\left(\vec{\rho}'\right)=\sum_{i=1}^{N_c}\hat{\tau}_i K_i^c P_i^c\left(\vec{\rho}'\right) \tag{3.57}$$

Equations (3.50)-(3.53) can be rewritten using equations (3.54)-(3.57)

$$\begin{aligned}
&-\frac{\omega\mu_0}{4}\sum_{i=1}^{N_d} I_i^d \int_{C_{di}} H_0^{(2)}\left(k_0\left|\vec{\rho}-\vec{\rho}'\right|\right)dl' \\
&\qquad -\frac{jk_0}{4}\sum_{i=1}^{N_d} K_i^d \int_{C_{di}} H_1^{(2)}\left(k_0\left|\vec{\rho}-\vec{\rho}'\right|\right)\frac{\hat{n}_i^d\cdot\left(\vec{\rho}-\vec{\rho}'\right)}{\left|\vec{\rho}-\vec{\rho}'\right|}dl' = -E_z^i\,,\ S_d^-
\end{aligned} \tag{3.58}$$

$$\begin{aligned}
&\frac{\omega\mu_1}{4}\sum_{i=1}^{N_d} I_i^d \int_{C_{di}} H_0^{(2)}\left(k_0\left|\vec{\rho}-\vec{\rho}'\right|\right)dl' \\
&\quad +\frac{jk_0}{4}\sum_{i=1}^{N_d} K_i^d \int_{C_{di}} H_1^{(2)}\left(k_0\left|\vec{\rho}-\vec{\rho}'\right|\right)\frac{\hat{n}_i^d\cdot\left(\vec{\rho}-\vec{\rho}'\right)}{\left|\vec{\rho}-\vec{\rho}'\right|}dl' \\
&\quad +\frac{\omega\mu_1}{4}\sum_{i=1}^{N_c} I_i^c \int_{C_{ci}} H_0^{(2)}\left(k_1\left|\vec{\rho}-\vec{\rho}'\right|\right)dl' \\
&\quad +\frac{jk_1}{4}\sum_{i=1}^{N_c} K_i^c \int_{C_{ci}} H_1^{(2)}\left(k_1\left|\vec{\rho}-\vec{\rho}'\right|\right)\frac{\hat{n}_i^c\cdot\left(\vec{\rho}-\vec{\rho}'\right)}{\left|\vec{\rho}-\vec{\rho}'\right|}dl' = 0,\ S_d^+
\end{aligned} \tag{3.59}$$

$$\begin{aligned}
&\frac{\omega\mu_1}{4}\sum_{i=1}^{N_d} I_i^d \int_{C_{di}} H_0^{(2)}\left(k_0\left|\vec{\rho}-\vec{\rho}'\right|\right)dl' \\
&\quad +\frac{jk_0}{4}\sum_{i=1}^{N_d} K_i^d \int_{C_{di}} H_1^{(2)}\left(k_0\left|\vec{\rho}-\vec{\rho}'\right|\right)\frac{\hat{n}_i^d\cdot\left(\vec{\rho}-\vec{\rho}'\right)}{\left|\vec{\rho}-\vec{\rho}'\right|}dl' \\
&\quad +\frac{\omega\mu_1}{4}\sum_{i=1}^{N_c} I_i^c \int_{C_{ci}} H_0^{(2)}\left(k_1\left|\vec{\rho}-\vec{\rho}'\right|\right)dl' \\
&\quad +\frac{jk_1}{4}\sum_{i=1}^{N_c} K_i^c \int_{C_{ci}} H_1^{(2)}\left(k_1\left|\vec{\rho}-\vec{\rho}'\right|\right)\frac{\hat{n}_i^c\cdot\left(\vec{\rho}-\vec{\rho}'\right)}{\left|\vec{\rho}-\vec{\rho}'\right|}dl' = 0,\ S_c^-
\end{aligned} \tag{3.60}$$

$$\begin{aligned}
&-\frac{\omega\mu_2}{4}\sum_{i=1}^{N_c} I_i^c \int_{C_{ci}} H_0^{(2)}\left(k_2\left|\vec{\rho}-\vec{\rho}'\right|\right)dl' \\
&\qquad -\frac{jk_2}{4}\sum_{i=1}^{N_c} K_i^c \int_{C_{ci}} H_1^{(2)}\left(k_2\left|\vec{\rho}-\vec{\rho}'\right|\right)\frac{\hat{n}_i^c\cdot\left(\vec{\rho}-\vec{\rho}'\right)}{\left|\vec{\rho}-\vec{\rho}'\right|}dl' = 0,\ S_c^+
\end{aligned} \tag{3.61}$$

where $k_2=\omega\sqrt{\mu_2\varepsilon_{c2}}$ .The unknown expansion coefficients are solved and the far scattered field can be computed using equation (3.31).

3.4 Numerical Results

Scattering cross section of a circular perfectly conducting cylindrical object coated with a dielectric material and a circular dielectric cylindrical object coated with a dielectric material are shown in Figure 3.10. and 3.11, respectively. The results are obtained by using both analytical and numerical methods. The ppw is chosen as 20, and a good agreement is observed between the two methods.

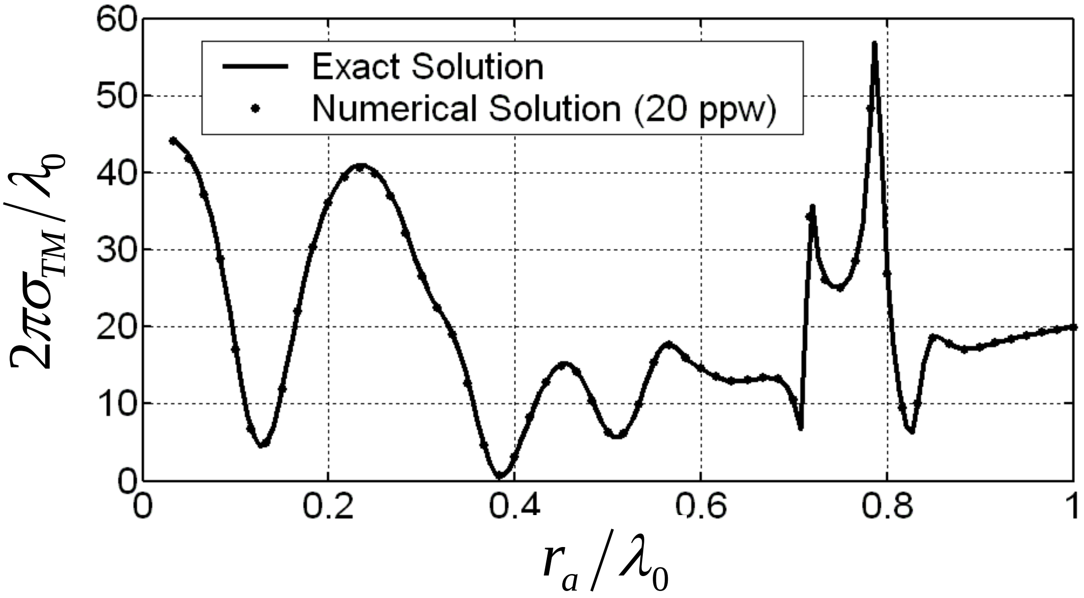

Figure 3. 10 Scattering cross section of a circular perfectly conducting cylindrical object coated with a dielectric material for $f = 1\,\text{GHz}$, $\phi_i = \phi_s = 20^\circ$, $\varepsilon_1 = 4\varepsilon_0$ F/m, $\mu_1 = \mu_0$ H/m, $r_b = \lambda_0$ and $\sigma_1 = 0.0$ Sm^{-1}

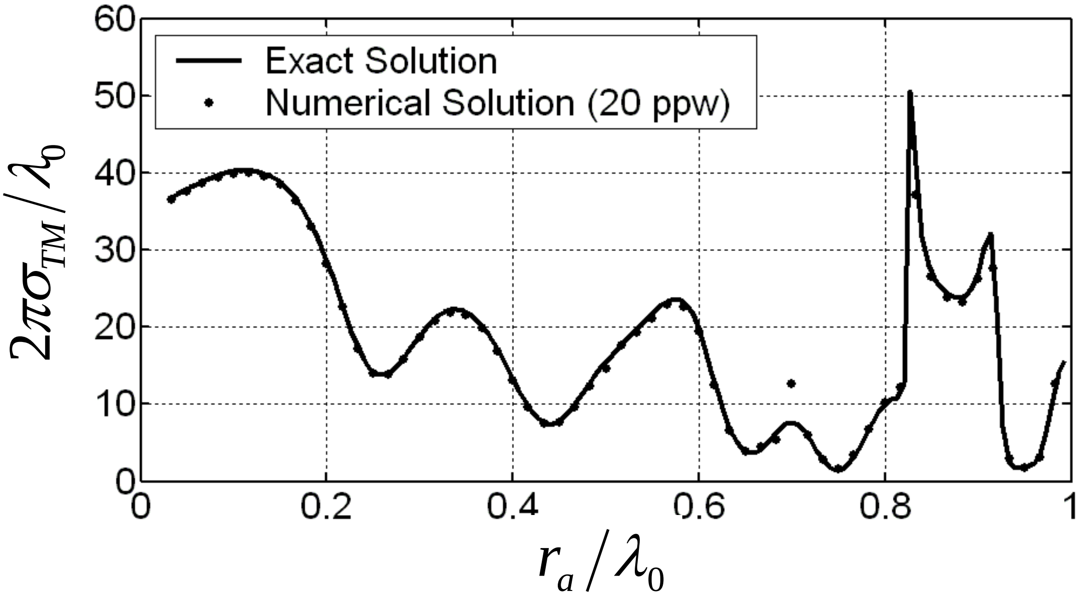

Figure 3. 11 Scattering cross section of a circular dielectric cylindrical object coated with a dielectric material for $f = 1\,\text{GHz}$, $\phi_i = \phi_s = 20^\circ$, $\varepsilon_1 = 4\varepsilon_0$ F/m, $\varepsilon_2 = 2\varepsilon_0$ F/m, $\mu_1 = \mu_2 = \mu_0$ H/m, $r_b = \lambda_0$ and $\sigma_1 = \sigma_2 = 0.0$ Sm^{-1}

CHAPTER 4

COMPUTATION OF TM$_z$ SCATTERING FROM AN OBJECT BURIED IN A MEDIUM WITH A FLAT SURFACE BY A PERTURBATION METHOD

4.1 Introduction

In this chapter, a new numerical solution method is presented for the electromagnetic field scattered by a cylindrical object with an arbitrary cross-section buried in a lossy dielectric half-space. The dielectric half-space is considered to be flat, and the method is outlined for TM$_z$ polarized incident wave. The surface equivalence principle and a perturbation method are utilized to form a set of electric field integral equations (EFIEs) for the currents on the object and the portion of the surface most strongly interacting with the object. To obtain the scattered E-field, the EFIEs are solved in the frequency domain using MoM.

4.2 Scattering from a Conducting Cylindrical Object Buried in a Medium with a Flat Surface

4.2.1 Theory

The geometry of the problem is shown in Figure 4.1. A perfectly conducting (PEC) object is located h_c below the surface. The distance between y-axis and the object axis is indicated by x_c.

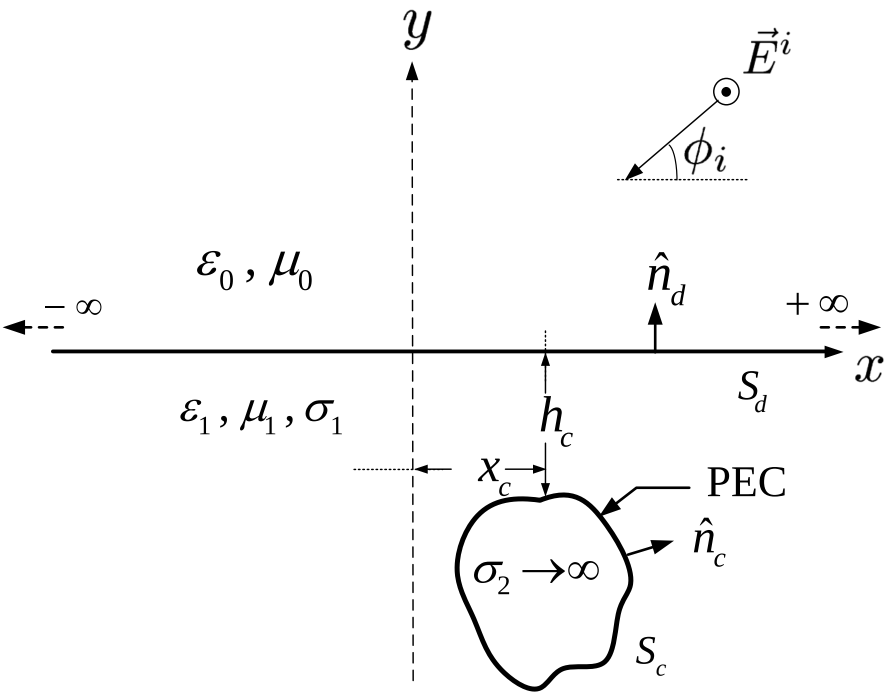

Figure 4. 1 The geometry of the problem

The scattered E-field $(\vec{E}^s)$ can be written as the sum of the scattered field from the PEC object and the flat surface

$$\vec{E}^s = \vec{E}^S + \vec{E}^T \tag{4.1}$$

S and T indicate surface and object, respectively. The scattered E-field from the surface can be written as

$$\vec{E}^S = \vec{E}^I + \vec{E}^P \tag{4.2}$$

where $\vec{E}^P$ is the perturbational field produced by the difference, or perturbation currents $\vec{J}_d^p$ and $\vec{M}_d^p$, and $\vec{E}^I$ is the field due to currents $\vec{J}^I$ and $\vec{M}^I$ on the surface which is impressed by the incident field without the object present. Therefore, the difference currents can be defined as $\vec{J}_d^p = \vec{J}^S - \vec{J}^I$ and $\vec{M}_d^p = \vec{M}^S - \vec{M}^I$. Here, $\vec{J}^S$ and $\vec{M}^S$ represent the equivalent currents on the surface. Then, substituting equation (4.2) into the equation (4.1) gives

$$\vec{E}^s = \vec{E}^I + \vec{E}^P + \vec{E}^T \tag{4.3}$$

The unknown currents are the equivalent perturbation currents on the surface and the induced current on the object. These currents are obtained by using the surface equivalence principle.

Before applying the surface equivalence principle to the original problem, the scattered E-field $\vec{E}^I$ should be obtained when the flat surface is the only scatterer. Therefore, the flat surface is chosen to be the only scatterer shown in Figure 4.2.

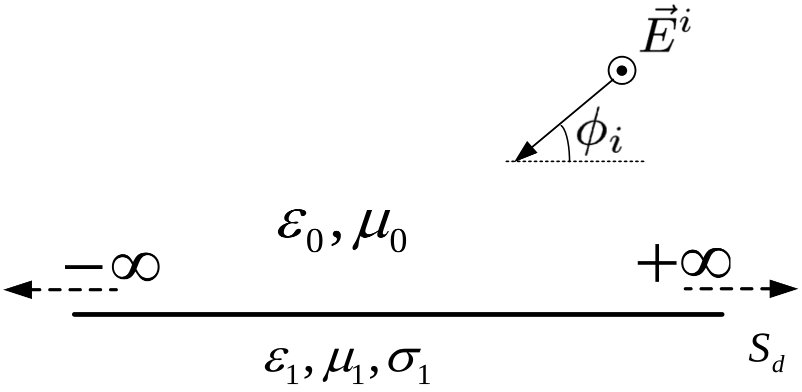

Figure 4. 2 The flat surface as a scatterer

Figure 4.3 shows the external equivalence principle applied to the problem in Figure 4.2. The whole space parameters are chosen as (ε_0, μ_0). The surface is replaced by surface electric $(\vec{J}^I)$ and magnetic $(\vec{M}^I)$ currents. At any point outside the surface, the total fields are $\vec{E}$ and $\vec{H}$. The total fields are zero under the surface

$$\left(\vec{E}^i + \vec{E}^I_{ext}\right)\Big|_{S_d^-} = 0 \tag{4.4}$$

$$\left(\vec{H}^i + \vec{H}^I_{ext}\right)\Big|_{S_d^-} = 0 \tag{4.5}$$

Then, the internal equivalence principle is applied in Figure 4.4 to the problem shown in Figure 4.2. Therefore, the whole space parameters are chosen as $(\varepsilon_1, \mu_1, \sigma_1)$. The surface is replaced by $(-\vec{J}^I)$ and $(-\vec{M}^I)$ currents.

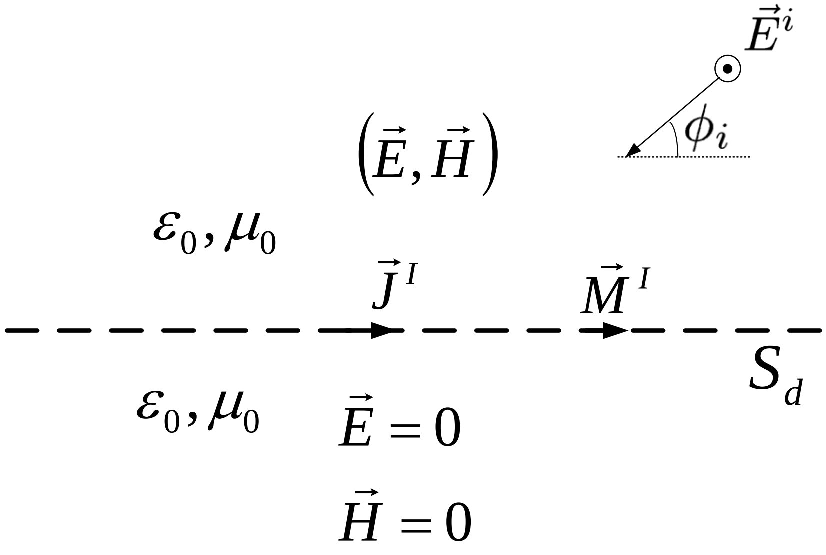

Figure 4. 3 External equivalence applied to the problem in Figure 4.2

The total fields are zero at any point external to S_d

$$\left(\vec{E}_{int}^I\right)\Big|_{S_d^+}=0 \tag{4.6}$$

$$\left(\vec{H}_{int}^I\right)\Big|_{S_d^+}=0 \tag{4.7}$$

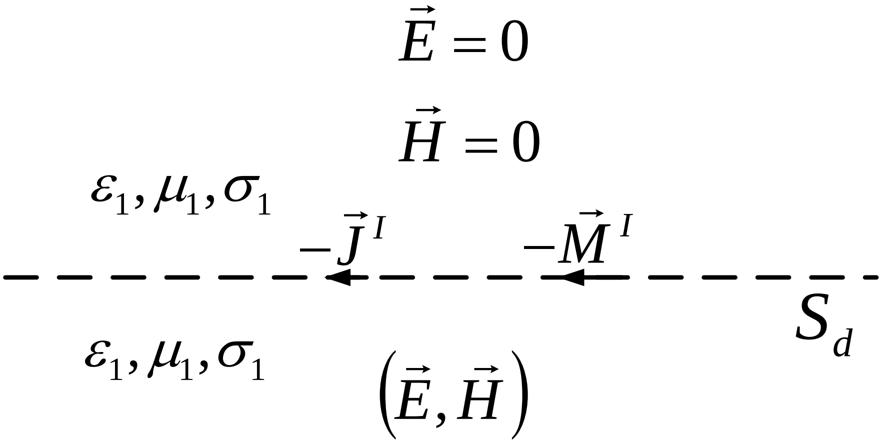

Figure 4. 4. Internal equivalence applied to the problem in Figure 4.2

Now, with the knowledge of scattered E-fields on the surface when there is not any object, the original problem in Figure 4.1 can be solved. Initially, the external equivalence principle is applied in Figure 4.5. The total field outside the surface is the sum of the incident and scattered field

$$\vec{E} = \vec{E}^i + \vec{E}^s \tag{4.8}$$

$$\vec{H} = \vec{H}^i + \vec{H}^s \tag{4.9}$$

and the scattered E-field is

$$\vec{E}^s = \vec{E}^I_{ext} + \vec{E}^P_{ext} \tag{4.10}$$

In Figure 4.5, $\vec{J}^p_d$ and $\vec{M}^p_d$ are the perturbation currents

$$\vec{J}^p_d = \hat{n}_d \times \vec{H}^P \Big|_{S_d^+} \tag{4.11}$$

$$\vec{M}^p_d = \vec{E}^P \Big|_{S_d^+} \times \hat{n}_d \tag{4.12}$$

The total field is zero just inside the surface S_d

$$\left(\vec{E}^s = -\vec{E}^i\right)\Big|_{S_d^-} \tag{4.13}$$

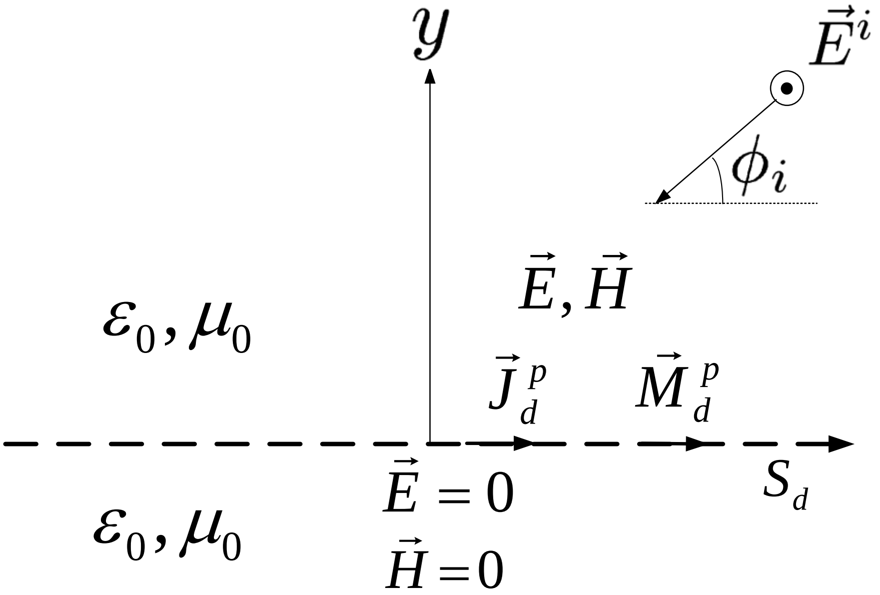

Figure 4. 5 The external equivalence principle applied to the problem in Figure 4.1

Then, the field caused by perturbation currents becomes

$$\left(\vec{E}^P_{ext}\right)\Big|_{S_d^-} = \left(-\vec{E}^I_{ext} - \vec{E}^i\right)\Big|_{S_d^-} \tag{4.14}$$

Now, equation (4.4) is used in equation (4.14), then the value of the perturbation field on S_d^- becomes

$$\vec{E}_{ext}^P\left(\vec{J}_d^p, \vec{M}_d^p\right)\Big|_{S_d^-} = 0 \tag{4.15}$$

Then, the internal equivalence principle is applied in Figure 4.6 to the problem shown in Figure 4.1. There is no incident wave, and the total fields under the surface contain just the scattered fields

$$\vec{E} = \vec{E}^s \tag{4.16}$$

$$\vec{H} = \vec{H}^s \tag{4.17}$$

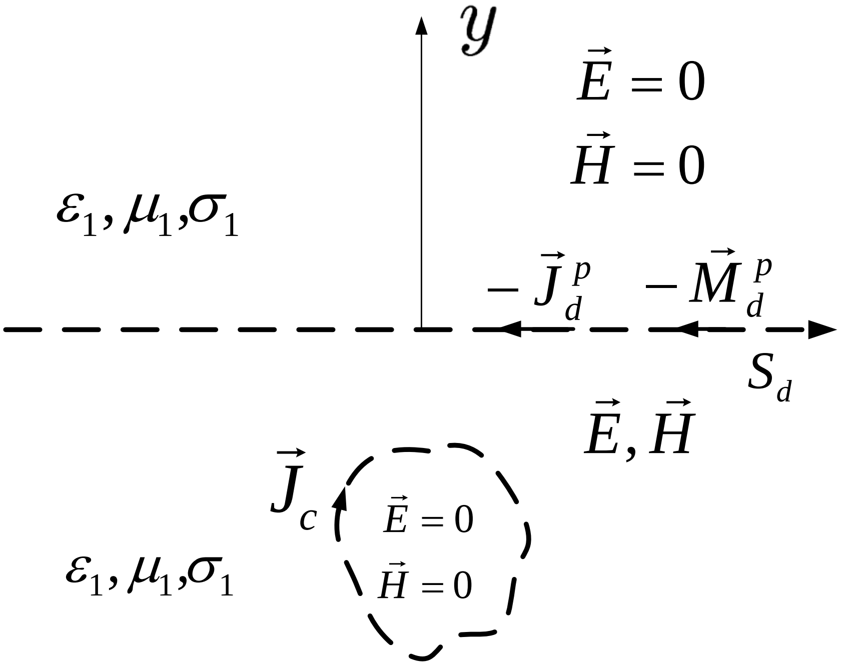

Figure 4. 6 The internal equivalence principle applied to the problem in Figure 4.1

The scattered E-field is expressed

$$\vec{E}^s = \vec{E}_{int}^I + \vec{E}_{int}^P + \vec{E}^T \tag{4.18}$$

The total E-field is zero outside S_d

$$\vec{E}_{int}^P\left(-\vec{J}_d^p, -\vec{M}_d^p\right)\Big|_{S_d^+} + \vec{E}^T\left(\vec{J}_c\right)\Big|_{S_d^+} = \left(-\vec{E}_{int}^I\right)\Big|_{S_d^+} \tag{4.19}$$

After equation (4.6) is used in equation (4.19), the scattered E-field on S_d^+ becomes

$$\vec{E}_{int}^{P}\left(-\vec{J}_{d}^{\,p},-\vec{M}_{d}^{\,p}\right)\Big|_{S_d^+}+\vec{E}^{T}\left(\vec{J}_{c}\right)\Big|_{S_d^+}=0 \tag{4.20}$$

The total field is also zero inside S_c

$$\vec{E}_{int}^{P}\left(-\vec{J}_{d}^{\,p},-\vec{M}_{d}^{\,p}\right)\Big|_{S_c^-}+\vec{E}^{T}\left(\vec{J}_{c}\right)\Big|_{S_c^-}=\left(-\vec{E}_{int}^{I}\right)\Big|_{S_c^-} \tag{4.21}$$

$\vec{E}_{int}^{I}$ on S_c^- is the E-field value on the object points when the object is absent. Therefore, this E-field can be obtained analytically in a closed form as

$$\vec{E}_{int}^{I}=\hat{z}\,T\,E_0 e^{jk_1\left(x\sin\phi_t+y\cos\phi_t\right)} \tag{4.22}$$

The transmission coefficient is indicated by T

$$T=\frac{2\eta_1\cos\phi_i}{\eta_1\cos\phi_i+\eta_0\cos\phi_t} \tag{4.23}$$

Here, ϕ_t is the transmission angle and defined by Snell's law;

$$\phi_t=\sin^{-1}\left(\sqrt{\frac{\varepsilon_0\mu_0}{\varepsilon_{c1}\mu_1}}\cos\phi_i\right) \tag{4.24}$$

In other words, there are three equations (4.15), (4.20) and (4.21) to be solved by using MoM and three unknown currents to calculate the scattered field.

The E-field is expressed in terms of electric and magnetic potential functions, and equations (4.15), (4.20) and (4.21) can be rewritten as;

$$-j\omega A_z^{ext}\left(\vec{J}_d^{\,p}\right)-\frac{1}{\varepsilon_0}\left[\nabla\times\vec{F}^{ext}\left(\vec{M}_d^{\,p}\right)\right]_z=0,\ S_d^- \tag{4.25}$$

$$-j\omega A_z^{int}\left(-\vec{J}_d^{\,p}\right)-j\omega A_z^{int}\left(\vec{J}_c\right)-\frac{1}{\varepsilon_{c1}}\left[\nabla\times\vec{F}^{int}\left(-\vec{M}_d^{\,p}\right)\right]_z=0,\ S_d^+ \tag{4.26}$$

$$-j\omega A_z^{int}\left(-\vec{J}_d^{\,p}\right)-j\omega A_z^{int}\left(\vec{J}_c\right)-\frac{1}{\varepsilon_{c1}}\left[\nabla\times\vec{F}^{int}\left(-\vec{M}_d^{\,p}\right)\right]_z=-\left[\vec{E}_{int}^{I}\right]_z,\ S_c^- \tag{4.27}$$

Three equations (4.25)-(4.27) are solved numerically using MoM for three unknown surface currents ($\vec{J}_d^{\,p},\vec{M}_d^{\,p},\vec{J}_c$). The currents on the surfaces of S_d and S_c are approximated by linear segments

$$\vec{J}_c(\vec{\rho}') = \hat{z}\sum_{i=1}^{N_c} I_i^c P_i^c(\vec{\rho}') \tag{4.28}$$

$$\vec{J}_d^{\,p}(\vec{\rho}') = \hat{z}\sum_{i=1}^{N_d} I_i^d P_i^d(\vec{\rho}') \tag{4.29}$$

$$\vec{M}_d^{\,p}(\vec{\rho}') = \sum_{i=1}^{N_d} \hat{\tau}_i K_i^d P_i^d(\vec{\rho}') \tag{4.30}$$

Equations (4.25)-(4.27) can be rewritten using equations (4.28)-(4.30)

$$\begin{aligned} &-\frac{\omega\mu_0}{4}\sum_{i=1}^{N_d} I_i^d \int_{C_{di}} H_0^{(2)}\left(k_0\left|\vec{\rho}-\vec{\rho}'\right|\right)dl' \\ &\qquad -\frac{jk_0}{4}\sum_{i=1}^{N_d} K_i^d \int_{C_{di}} H_1^{(2)}\left(k_0\left|\vec{\rho}-\vec{\rho}'\right|\right)\frac{\hat{n}_i^d\cdot(\vec{\rho}-\vec{\rho}')}{\left|\vec{\rho}-\vec{\rho}'\right|}dl' = 0,\ S_d^- \end{aligned} \tag{4.31}$$

$$\begin{aligned} &\frac{\omega\mu_1}{4}\sum_{i=1}^{N_d} I_i^d \int_{C_{di}} H_0^{(2)}\left(k_1\left|\vec{\rho}-\vec{\rho}'\right|\right)dl' - \frac{\omega\mu_1}{4}\sum_{i=1}^{N_c} I_i^c \int_{C_{ci}} H_0^{(2)}\left(k_1\left|\vec{\rho}-\vec{\rho}'\right|\right)dl' \\ &\qquad +\frac{jk_1}{4}\sum_{i=1}^{N_d} K_i^d \int_{C_{di}} H_1^{(2)}\left(k_1\left|\vec{\rho}-\vec{\rho}'\right|\right)\frac{\hat{n}_i^d\cdot(\vec{\rho}-\vec{\rho}')}{\left|\vec{\rho}-\vec{\rho}'\right|}dl' = 0,\ S_d^+ \end{aligned} \tag{4.32}$$

$$\begin{aligned} &\frac{\omega\mu_1}{4}\sum_{i=1}^{N_d} I_i^d \int_{C_{di}} H_0^{(2)}\left(k_1\left|\vec{\rho}-\vec{\rho}'\right|\right)dl' - \frac{\omega\mu_1}{4}\sum_{i=1}^{N_c} I_i^c \int_{C_{ci}} H_0^{(2)}\left(k_1\left|\vec{\rho}-\vec{\rho}'\right|\right)dl' \\ &\qquad +\frac{jk_1}{4}\sum_{i=1}^{N_d} K_i^d \int_{C_{di}} H_1^{(2)}\left(k_1\left|\vec{\rho}-\vec{\rho}'\right|\right)\frac{\hat{n}_i^d\cdot(\vec{\rho}-\vec{\rho}')}{\left|\vec{\rho}-\vec{\rho}'\right|}dl' = -E_{int}^I,\ S_c^- \end{aligned} \tag{4.33}$$

Then, pulse weighting functions are used to transform these EFIEs to linear equations. These linear equations are solved to obtain the unknown currents, and the far scattered field can be computed using only $\vec{J}_d^{\,p}$ and $\vec{M}_d^{\,p}$.

4.3 Scattering from a Dielectric Cylindrical Object Buried in a Medium with a Flat Surface

4.3.1 Theory

A dielectric object is located under the flat surface as shown in Figure 4.7. The unknown currents are the equivalent perturbation currents on the surface and the induced currents on the object. These currents are obtained by using the surface

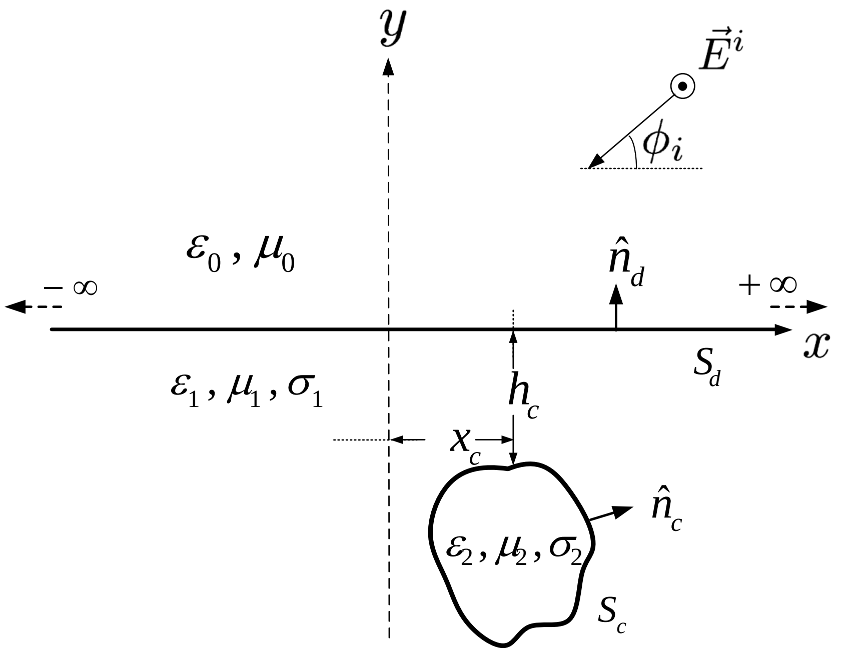

Figure 4. 7 The geometry of the problem

equivalence principle.

The original problem in Figure 4.7 can be solved with the knowledge of $\vec{E}^I$ explained in Chapter 4.2.1. Initially, the external equivalence principle is applied in Figure 4.8. The total field outside the surface is the sum of the incident, and scattered field

$$\vec{E} = \vec{E}^i + \vec{E}^s \tag{4.34}$$

$$\vec{H} = \vec{H}^i + \vec{H}^s \tag{4.35}$$

and the scattered E-field is

$$\vec{E}^s = \vec{E}^I_{ext} + \vec{E}^P_{ext} \tag{4.36}$$

The total field is zero just inside the surface S_d

$$\left(\vec{E}^s = -\vec{E}^i\right)\Big|_{S_d^-} \tag{4.37}$$

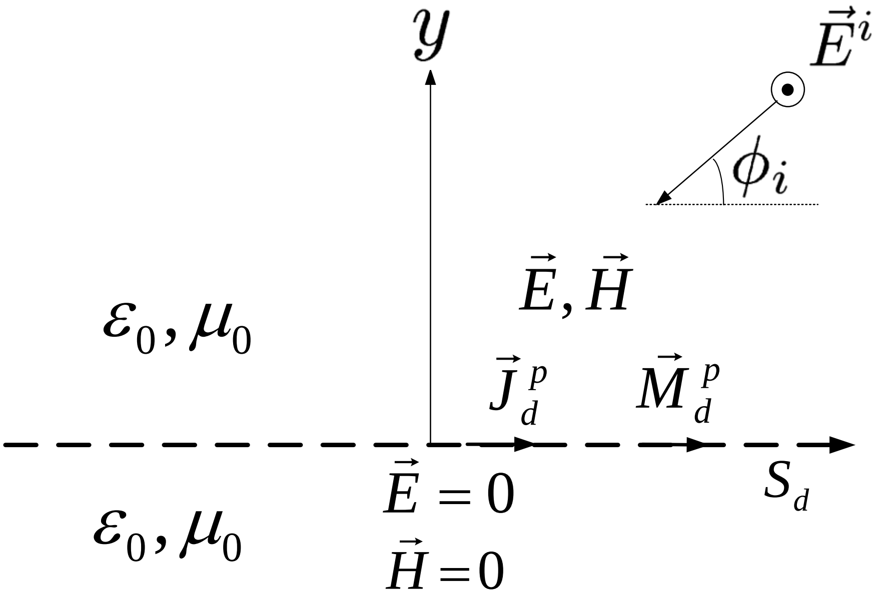

Figure 4. 8 The external equivalence principle applied to the problem in Figure 4.7

Then, the field caused by perturbation currents becomes

$$\left(\vec{E}^P_{ext}\right)\Big|_{S_d^-} = \left(-\vec{E}^I_{ext} - \vec{E}^i\right)\Big|_{S_d^-} \tag{4.38}$$

Now, equation (4.4) is used in equation (4.38), then the value of the perturbation field on S_d^- becomes

$$\vec{E}^P_{ext}\left(\vec{J}^p_d,\vec{M}^p_d\right)\Big|_{S_d^-} = 0 \tag{4.39}$$

Then, the internal equivalence principle is applied in Figure 4.9 to the problem shown in Figure 4.7. There is no incident wave, and the total fields under the surface contain just the scattered fields

$$\vec{E} = \vec{E}^s \tag{4.40}$$

$$\vec{H} = \vec{H}^s \tag{4.41}$$

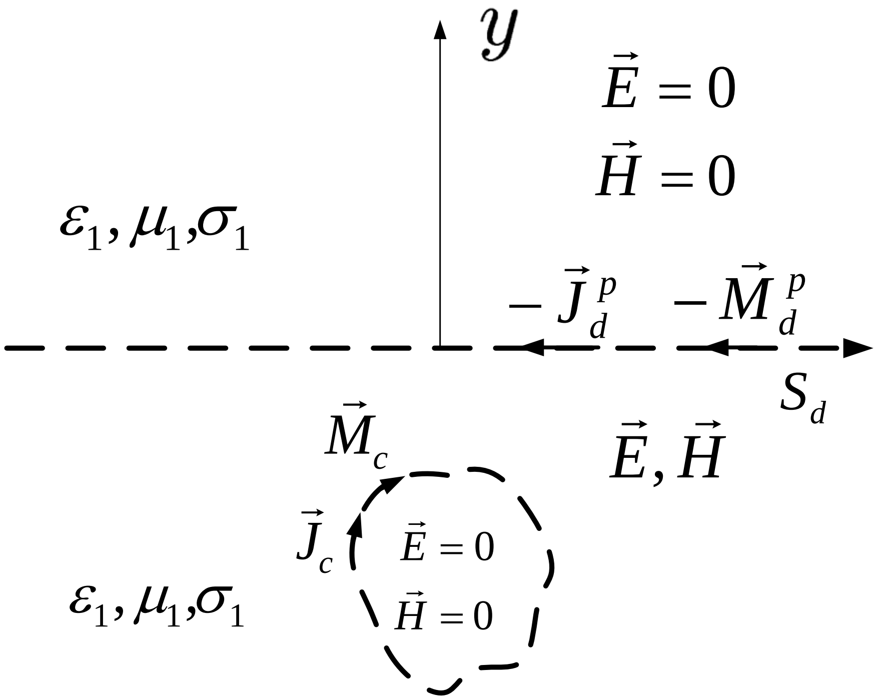

Figure 4. 9 The internal equivalence principle applied to the problem in Figure 4.7

The scattered E-field is expressed;

$$\vec{E}^s=\vec{E}_{int}^I+\vec{E}_{int}^P+\vec{E}^T \tag{4.42}$$

The total E-field is zero outside S_d

$$\vec{E}_{int}^P\left(-\vec{J}_d^p,-\vec{M}_d^p\right)\Big|_{S_d^+}+\vec{E}^T\left(\vec{J}_c,\vec{M}_c\right)\Big|_{S_d^+}=\left(-\vec{E}_{int}^I\right)\Big|_{S_d^+} \tag{4.43}$$

After equation (4.6) is used in equation (4.43), the scattered E-field on S_d^+ becomes,

$$\vec{E}_{int}^P\left(-\vec{J}_d^p,-\vec{M}_d^p\right)\Big|_{S_d^+}+\vec{E}^T\left(\vec{J}_c,\vec{M}_c\right)\Big|_{S_d^+}=0 \tag{4.44}$$

The total field is also zero inside S_c ,

$$\vec{E}_{int}^P\left(-\vec{J}_d^p,-\vec{M}_d^p\right)\Big|_{S_c^-}+\vec{E}^T\left(\vec{J}_c,\vec{M}_c\right)\Big|_{S_c^-}=\left(-\vec{E}_{int}^I\right)\Big|_{S_c^-} \tag{4.45}$$

Figure 4.10 shows the equivalence principle for the points inside of the cylinder applied to the problem in Figure 4.7. The whole space parameters are chosen as $\left(\varepsilon_2,\mu_2,\sigma_2\right)$.

The total field is zero on S_c^+

$$\vec{E}_{int}^{T}\left(-\vec{J}_c,-\vec{M}_c\right)\Big|_{S_c^+}=0 \tag{4.46}$$

Here, *int* means internal to the cylinder.

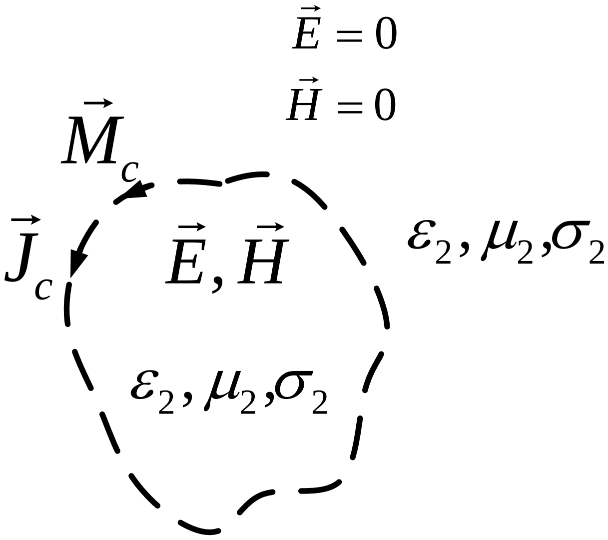

Figure 4. 10 The equivalence principle for the points inside of the cylinder applied to the problem in Figure 4.7

In other words, there are four equations (4.39), (4.44), (4.45) and (4.46) to be solved by using MoM and four unknown currents to calculate the scattered field.

The E-field is expressed in terms of electric and magnetic potential functions, and equations (4.39), (4.44), (4.45) and (4.46) can be rewritten as;

$$-j\omega A_z^{ext}\left(\vec{J}_d^{\,p}\right)-\frac{1}{\varepsilon_0}\left[\nabla\times\vec{F}^{ext}\left(\vec{M}_d^{\,p}\right)\right]_z=0,\ S_d^- \tag{4.47}$$

$$-j\omega A_z^{int}\left(-\vec{J}_d^{\,p}\right)-j\omega A_z^{int}\left(\vec{J}_c\right)-\frac{1}{\varepsilon_{c1}}\left[\nabla\times\vec{F}^{int}\left(-\vec{M}_d^{\,p}\right)\right]_z=0,\ S_d^+ \tag{4.48}$$

$$-j\omega A_z^{int}\left(-\vec{J}_d^{\,p}\right)-j\omega A_z^{int}\left(\vec{J}_c\right)-\frac{1}{\varepsilon_{c1}}\left[\nabla\times\vec{F}^{int}\left(-\vec{M}_d^{\,p}\right)\right]_z=-\left[\vec{E}_{int}^{I}\right]_z,\ S_c^- \tag{4.49}$$

$$-j\omega A_z^{int}\left(-\vec{J}_c\right)-\frac{1}{\varepsilon_{c2}}\left[\tilde{N}\times\vec{F}^{int}\left(-\vec{M}_c\right)\right]_z=0,\ S_c^+ \tag{4.50}$$

Four equations (4.47)-(4.50) are solved numerically using MoM for four unknown surface currents ($\vec{J}_d^{\,p},\vec{M}_d^{\,p},\vec{J}_c,\vec{M}_c$). The currents on the surfaces of S_d and S_c are approximated by linear segments

$$\vec{J}_c\left(\vec{\rho}'\right)=\hat{z}\sum_{i=1}^{N_c} I_i^c P_i^c\left(\vec{\rho}'\right) \tag{4.51}$$

$$\vec{J}_d^{\,p}\left(\vec{\rho}'\right)=\hat{z}\sum_{i=1}^{N_d} I_i^d P_i^d\left(\vec{\rho}'\right) \tag{4.52}$$

$$\vec{M}_d^{\,p}\left(\vec{\rho}'\right)=\sum_{i=1}^{N_d} \hat{\tau}_i K_i^d P_i^d\left(\vec{\rho}'\right) \tag{4.53}$$

$$\vec{M}_c\left(\vec{\rho}'\right)=\sum_{i=1}^{N_c} \hat{\tau}_i K_i^c P_i^c\left(\vec{\rho}'\right) \tag{4.54}$$

Equations (4.47)-(4.50) can be rewritten using equations (4.51)-(4.54)

$$\begin{aligned}&-\frac{\omega\mu_0}{4}\sum_{i=1}^{N_d} I_i^d \int_{C_{di}} H_0^{(2)}\left(k_0\left|\vec{\rho}-\vec{\rho}'\right|\right)dl' \\ &\qquad -\frac{jk_0}{4}\sum_{i=1}^{N_d} K_i^d \int_{C_{di}} H_1^{(2)}\left(k_0\left|\vec{\rho}-\vec{\rho}'\right|\right)\frac{\hat{n}_i^d\cdot\left(\vec{\rho}-\vec{\rho}'\right)}{\left|\vec{\rho}-\vec{\rho}'\right|}dl'=0,\ S_d^-\end{aligned} \tag{4.55}$$

$$\begin{aligned}&\frac{\omega\mu_1}{4}\sum_{i=1}^{N_d} I_i^d \int_{C_{di}} H_0^{(2)}\left(k_1\left|\vec{\rho}-\vec{\rho}'\right|\right)dl'-\frac{\omega\mu_1}{4}\sum_{i=1}^{N_c} I_i^c \int_{C_{ci}} H_0^{(2)}\left(k_1\left|\vec{\rho}-\vec{\rho}'\right|\right)dl' \\ &\qquad +\frac{jk_1}{4}\sum_{i=1}^{N_d} K_i^d \int_{C_{di}} H_1^{(2)}\left(k_1\left|\vec{\rho}-\vec{\rho}'\right|\right)\frac{\hat{n}_i^d\cdot\left(\vec{\rho}-\vec{\rho}'\right)}{\left|\vec{\rho}-\vec{\rho}'\right|}dl'=0,\ S_d^+\end{aligned} \tag{4.56}$$

$$\begin{aligned}&\frac{\omega\mu_1}{4}\sum_{i=1}^{N_d} I_i^d \int_{C_{di}} H_0^{(2)}\left(k_1\left|\vec{\rho}-\vec{\rho}'\right|\right)dl'-\frac{\omega\mu_1}{4}\sum_{i=1}^{N_c} I_i^c \int_{C_{ci}} H_0^{(2)}\left(k_1\left|\vec{\rho}-\vec{\rho}'\right|\right)dl' \\ &\qquad +\frac{jk_1}{4}\sum_{i=1}^{N_d} K_i^d \int_{C_{di}} H_1^{(2)}\left(k_1\left|\vec{\rho}-\vec{\rho}'\right|\right)\frac{\hat{n}_i^d\cdot\left(\vec{\rho}-\vec{\rho}'\right)}{\left|\vec{\rho}-\vec{\rho}'\right|}dl'=-E_{int}^I,\ S_c^-\end{aligned} \tag{4.57}$$

$$\begin{aligned}&-\frac{\omega\mu_2}{4}\sum_{i=1}^{N_c} I_i^c \int_{C_{ci}} H_0^{(2)}\left(k_2\left|\vec{\rho}-\vec{\rho}'\right|\right)dl' \\ &\qquad -\frac{jk_2}{4}\sum_{i=1}^{N_c} K_i^c \int_{C_{ci}} H_1^{(2)}\left(k_2\left|\vec{\rho}-\vec{\rho}'\right|\right)\frac{n_i^c\cdot\left(\vec{\rho}-\vec{\rho}'\right)}{\left|\vec{\rho}-\vec{\rho}'\right|}dl'=0,\ S_c^+\end{aligned} \tag{4.58}$$

Then, pulse weighting functions are used to transform these EFIEs to linear equations. These linear equations are solved to obtain the unknown currents, and the far scattered field can be computed using only $\vec{J}_d^{\,p}$ and $\vec{M}_d^{\,p}$.

4.4 Numerical Results

If it is not indicated otherwise; for all MoM solutions, the value of 20 ppw is used to represent the currents on the object and the surface. The object is chosen to be a cylinder with circular cross-section of radius r_a (Figure 4.11).

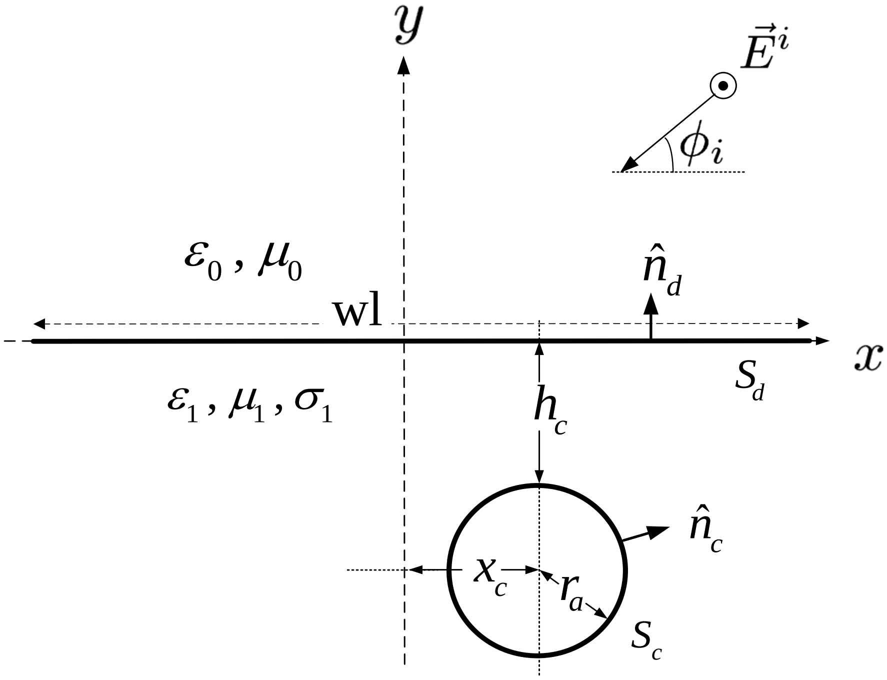

Figure 4. 11 The geometry used for the numerical results

The perturbation currents' behaviours are investigated in Figure 4.12 and 4.13 to validate the assumption that the equivalent currents on the surface will be affected only in a finite portion of the surface near the object. As expected, when the object is buried deeper, the perturbation currents spread along the surface. Therefore, it is important to select the truncation width (wl) carefully.

To investigate the effect of the conductivity of the half-space, different conductivities are used and shown in Figure 4.14 and 4.15. It is seen that the amplitude of the perturbation currents decreases when the loss of the ground increases.

After establishing the validity of our assumption, it is also necessary to determine accuracy of the method. This can be done by choosing the space parameters under the flat surface as (ε_0, μ_0). Thus, the scattered field is expected to behave like a PEC or dielectric cylinder. The scattered E-field is first solved by perturbation method, and then by analytical method. Then, these two results are compared in Figure 4.16 and 4.17.

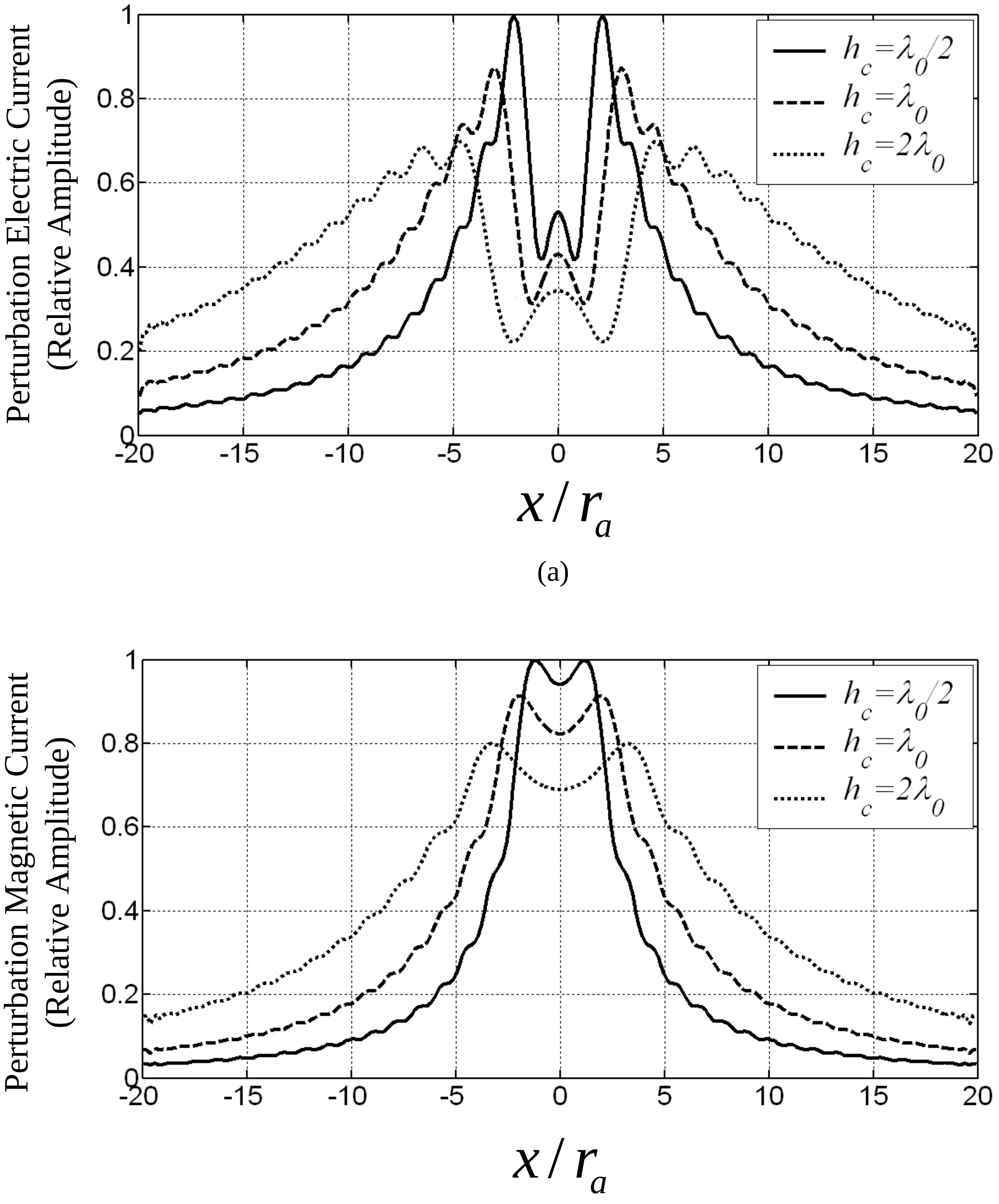

(a)

(b)

Figure 4. 12 Perturbation (a) electric currents normalized with 0.0016 A/m and (b) magnetic currents normalized with 0.2968 V/m on the flat surface above the PEC object for f=1 GHz, $\phi_i = \phi_s = 90^\circ$, $r_a = \lambda_0 / 3$ m, $x_c/r_a = 0.0$, $\varepsilon_1 = 15\varepsilon_0$ F/m, $\mu_1 = \mu_0$ H/m and $\sigma_1 = 0.0$ Sm^{-1}

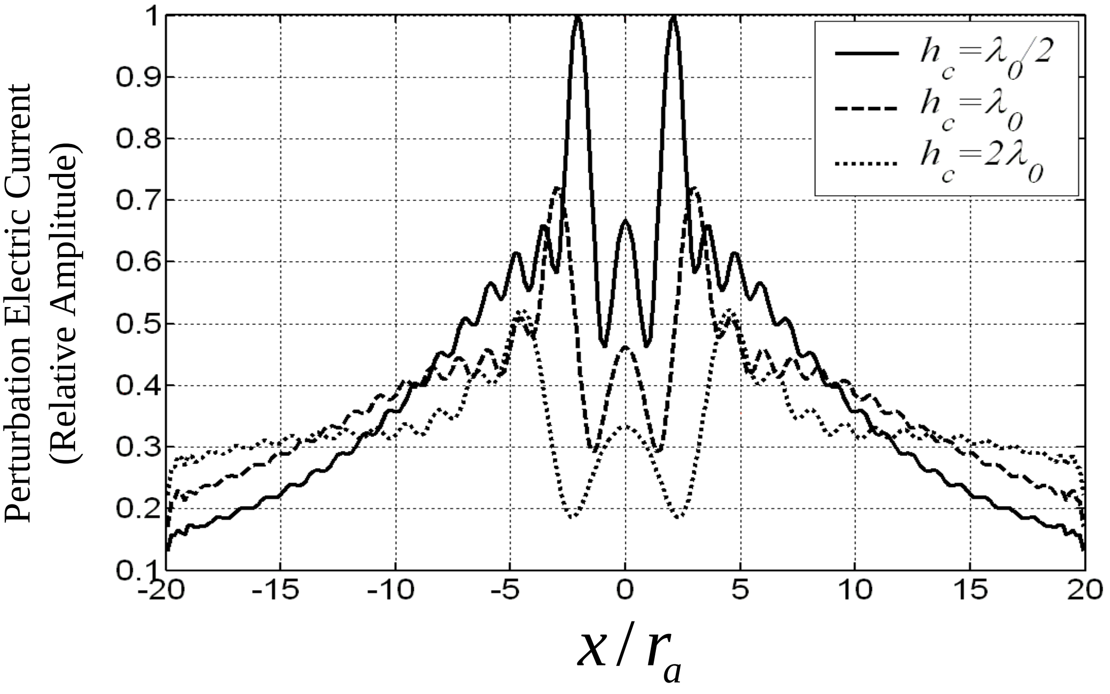

(a)

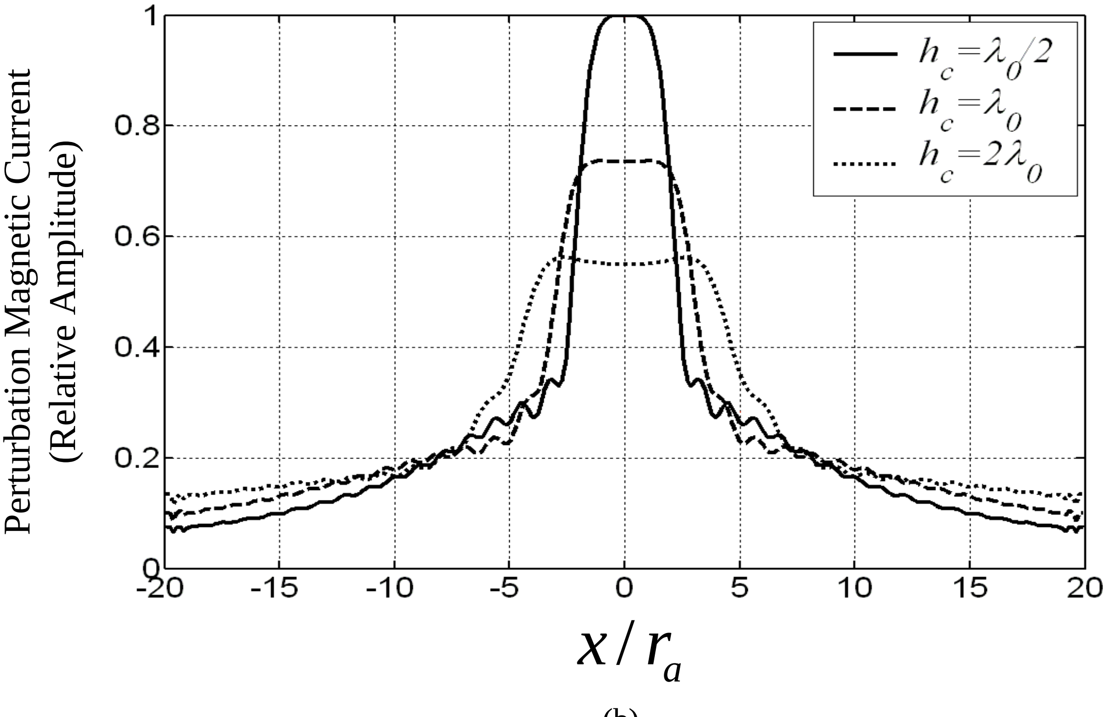

(b)

Figure 4. 13 Perturbation (a) electric currents normalized with 0.00073 A/m and (b) magnetic currents normalized with 0.16 V/m on the flat surface above the dielectric object for *f*=1 GHz, $\phi_i = \phi_s = 90^\circ$, $r_a = \lambda_0 / 3$ m, $x_c/r_a = 0.0$, $\varepsilon_1 = 15\varepsilon_0$ F/m, $\varepsilon_2 = 4\varepsilon_0$ F/m, $\mu_1 = \mu_2 = \mu_0$ H/m and $\sigma_1 = \sigma_2 = 0.0$ Sm^{-1}

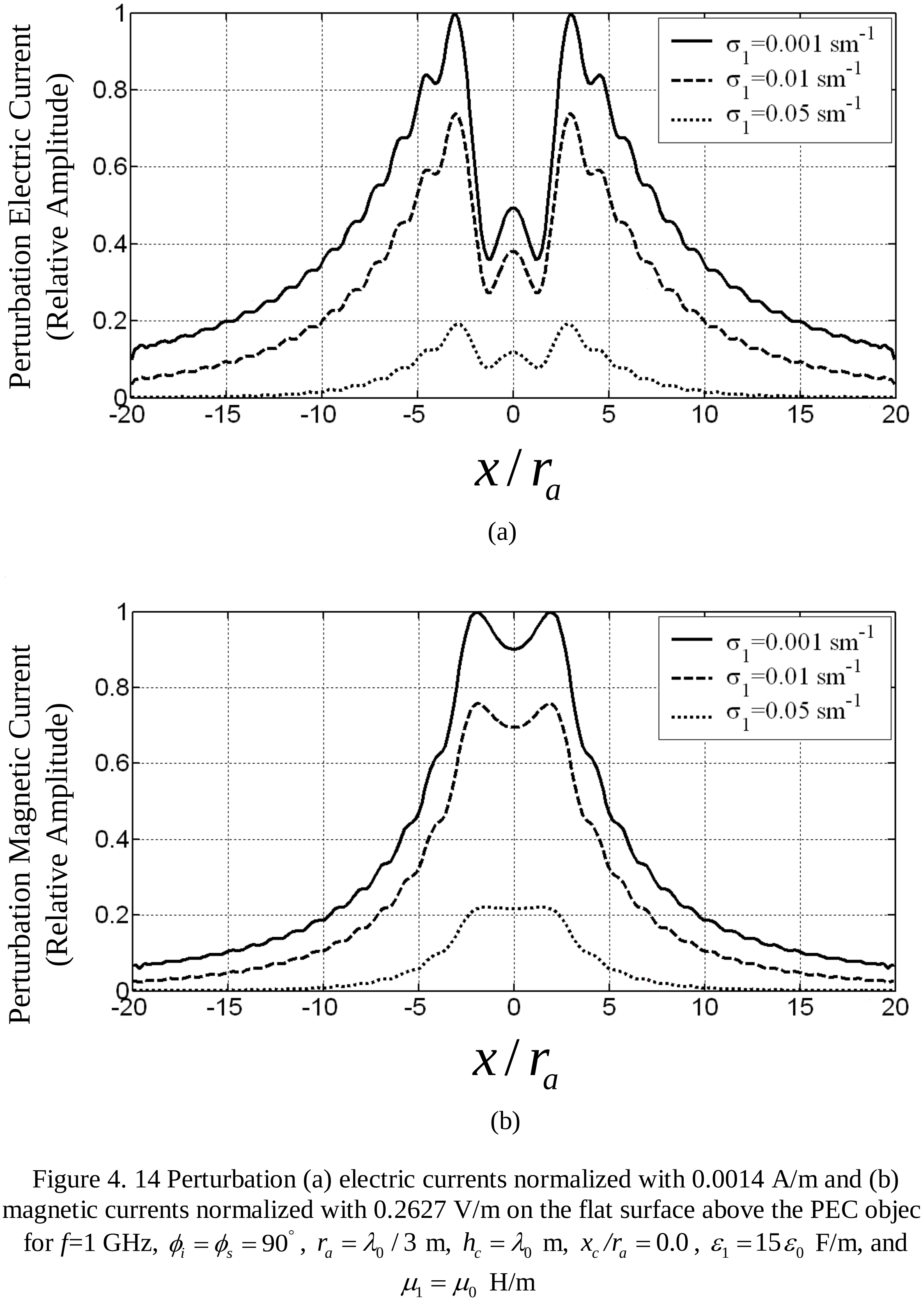

Figure 4. 14 Perturbation (a) electric currents normalized with 0.0014 A/m and (b) magnetic currents normalized with 0.2627 V/m on the flat surface above the PEC object for f=1 GHz, $\phi_i = \phi_s = 90^\circ$, $r_a = \lambda_0 / 3$ m, $h_c = \lambda_0$ m, $x_c/r_a = 0.0$, $\varepsilon_1 = 15\varepsilon_0$ F/m, and $\mu_1 = \mu_0$ H/m

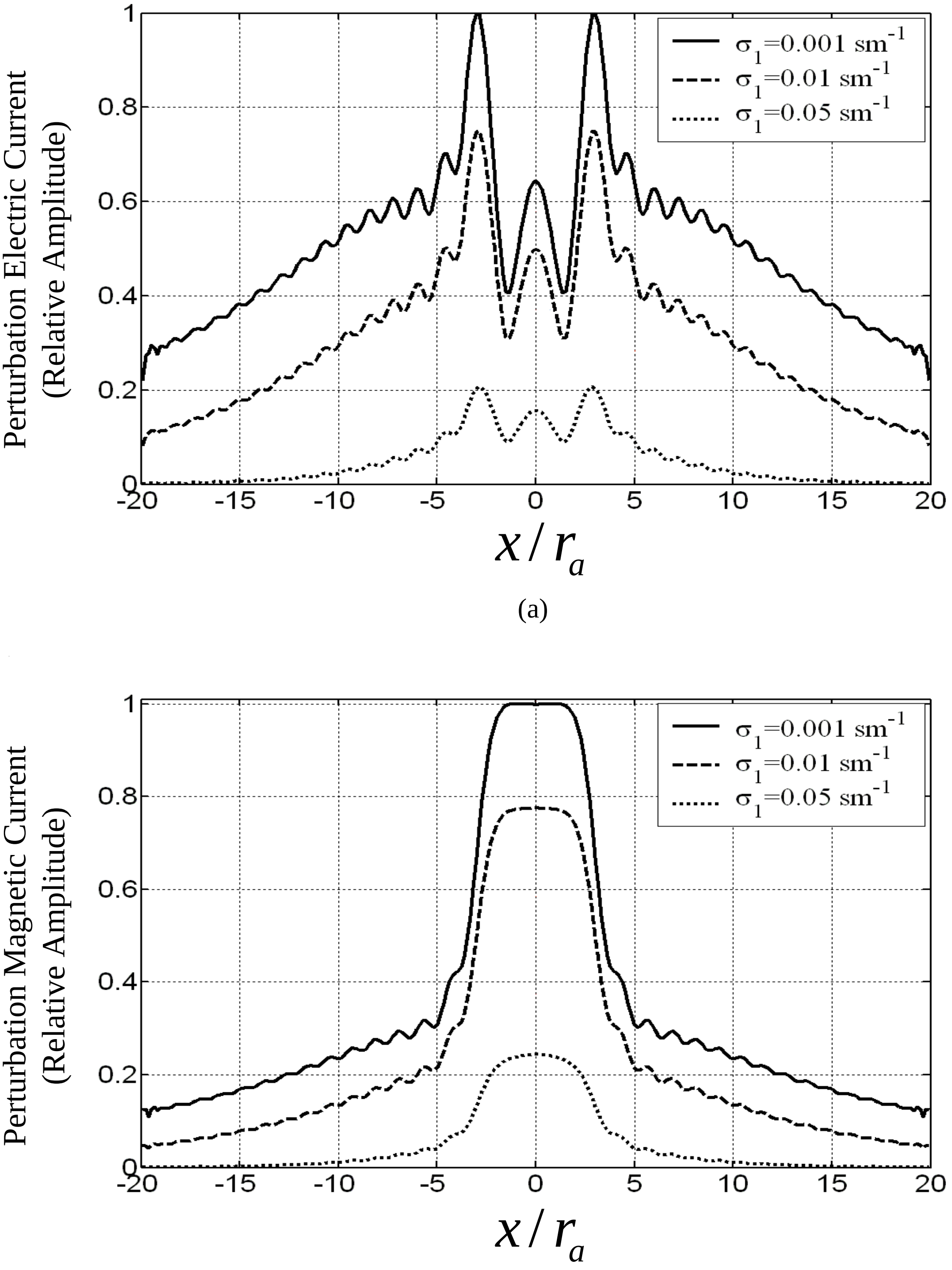

(a)

(b)

Figure 4. 15 Perturbation (a) electric currents normalized with 0.00051 A/m and (b) magnetic currents normalized with 0.12 V/m on the flat surface above the dielectric object for *f*=1 GHz, $\phi_i = \phi_s = 90^{\circ}$, $r_a = \lambda_0 / 3$ m, $h_c = \lambda_0$ m, $x_c/r_a = 0.0$, $\varepsilon_1 = 15\varepsilon_0$ F/m, $\varepsilon_2 = 4\varepsilon_0$ F/m, and $\mu_1 = \mu_2 = \mu_0$ H/m

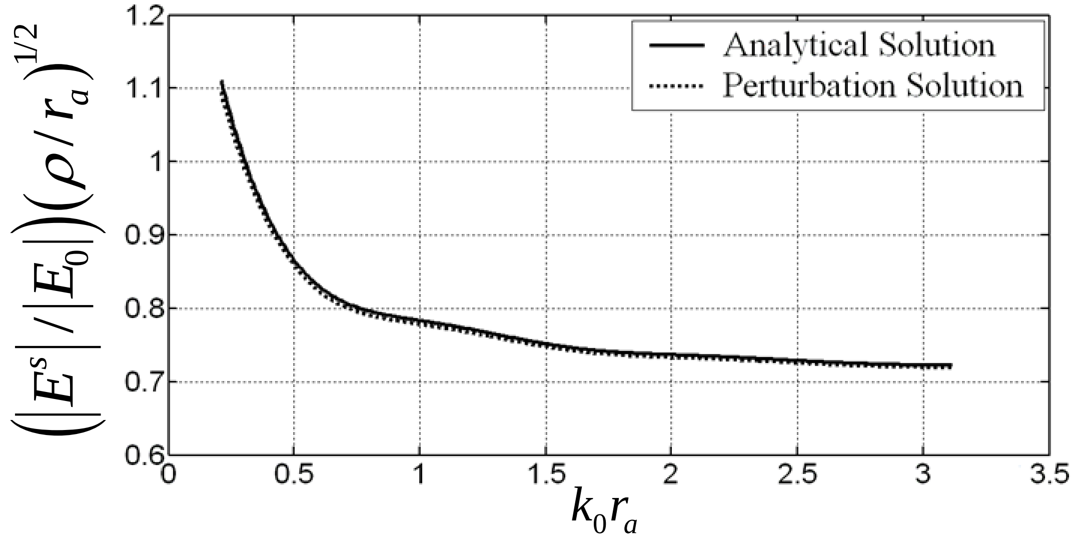

(a)

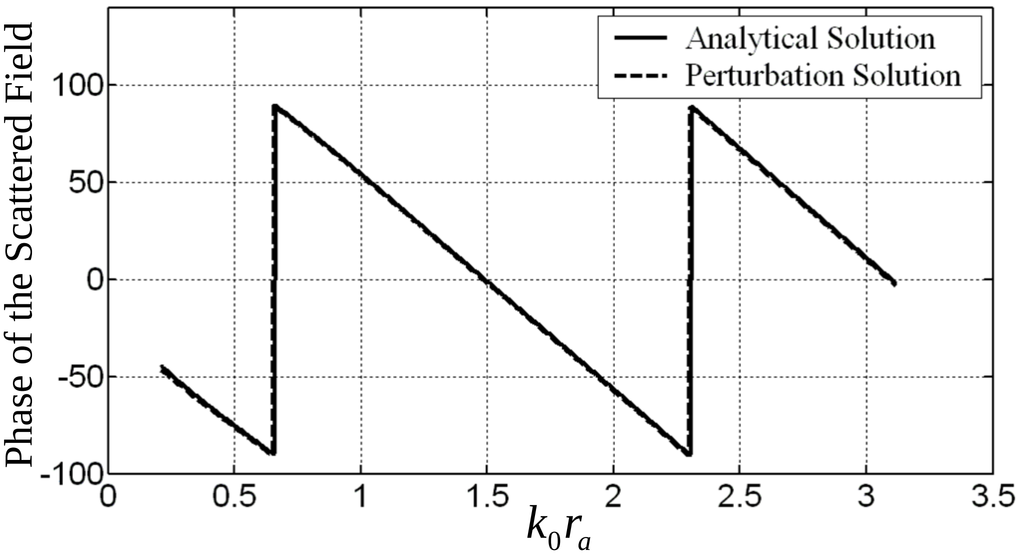

(b)

Figure 4. 16 Scattered field from the PEC object (a) normalized amplitude and (b) phase for $r_a = 0.01$m, $\phi_i = \phi_s = 90^\circ$, $h_c/r_a = 1.0$, $x_c / r_a = 0.0$, $\mathrm{wl}/r_a = 500$, $\varepsilon_1 = \varepsilon_0$ F/m, $\sigma_1 = 0.0$ Sm^{-1} and $\mu_1 = \mu_0$ H/m

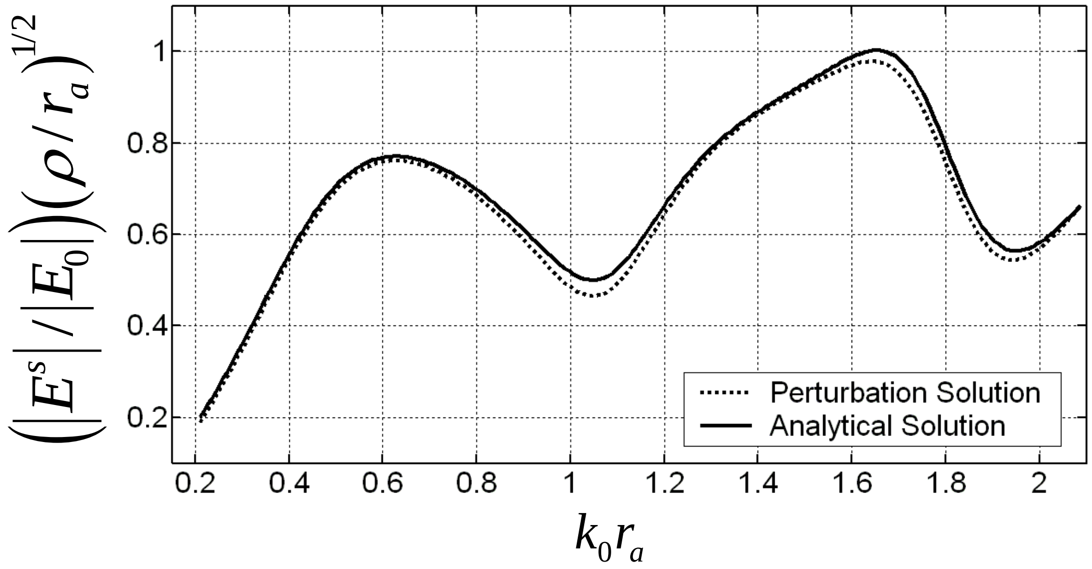

(a)

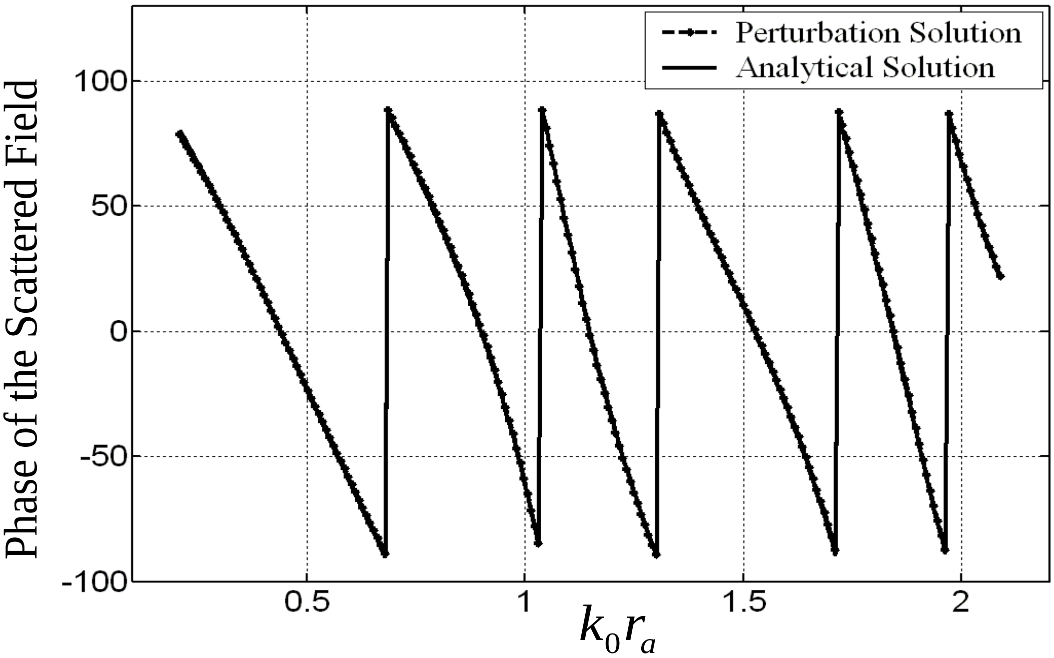

(b)

Figure 4. 17 Scattered field from the dielectric object (a) normalized amplitude and (b) phase for $r_a = 0.01\text{m}$, $\phi_i = \phi_s = 90^\circ$, $h_c/r_a = 1.0$, $x_c/r_a = 0.0$, $\text{wl}/r_a = 500$, $\varepsilon_1 = \varepsilon_0$ F/m, $\varepsilon_2 = 4\varepsilon_0$ F/m, $\sigma_1 = \sigma_2 = 0.0$ Sm^{-1} and $\mu_1 = \mu_2 = \mu_0$ H/m

The root-mean square error (E_{RMS}) between the perturbation method and the analytical solution is calculated by using

$$E_{RMS}(\%) = \sqrt{\frac{\left|E^A - E^P\right|^2}{\left|E^A\right|^2}} \tag{5.34}$$

where E^A and E^P show analytical and perturbation solutions; respectively. Then, the RMS error is calculated and shown in Figure 4.18. It is seen that the solution becomes more accurate for increasing truncation width and ppw.

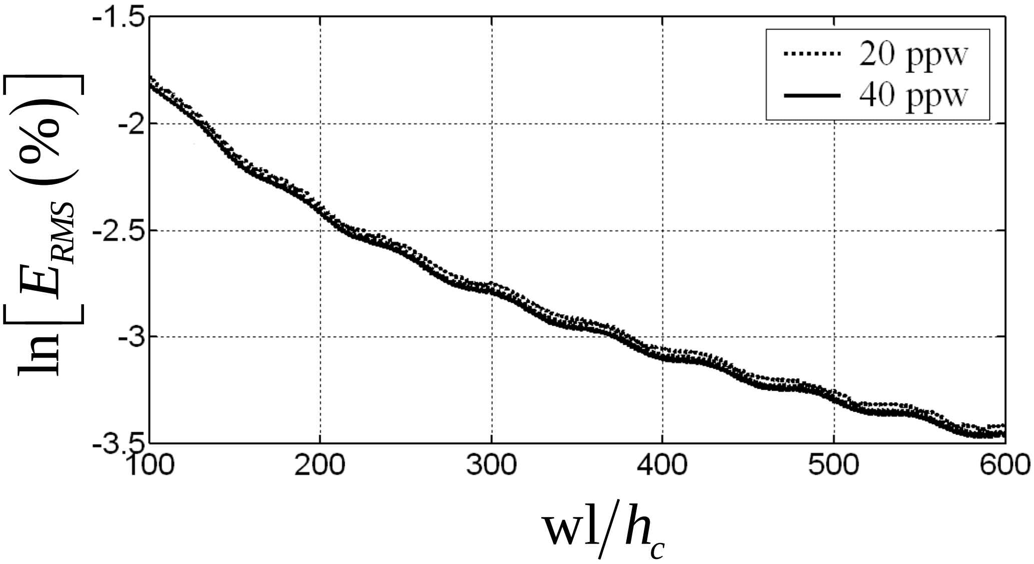

Figure 4. 18 The approximation difference of the method applied to the PEC object for *f*=1 GHz, $\phi_i = \phi_s = 90^\circ$, $r_a = 0.01$ m, $h_c / r_a = 1.0$, $x_c / r_a = 0.0$, $\varepsilon_1 = \varepsilon_0$ F/m, $\sigma_1 = 0.0$ Sm^{-1} and $\mu_1 = \mu_0$ H/m

To validate the perturbation method for lossy half-space, the solution for the PEC object buried under a flat surface is compared to the results in [9] including Green's function approach. The comparison is shown in Figure 4.19. Increasing truncation width makes the solution to converge the result of Green's function approach.

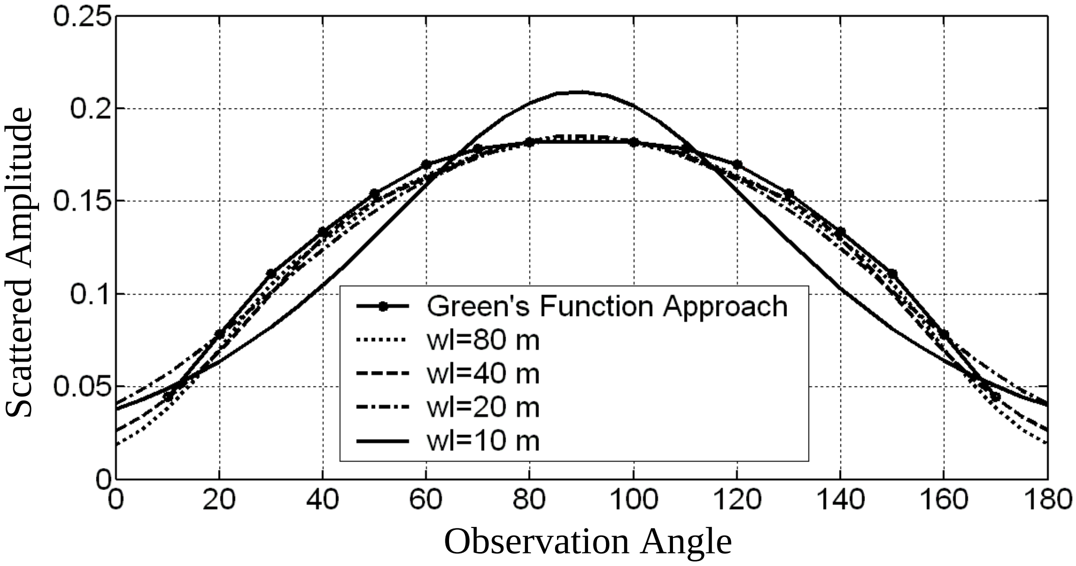

Figure 4. 19 Scattered amplitude from a PEC cylindrical scatterer with circular cross-section for *f*=30 MHz, $r_a = 0.3$ m, $h_c = 1.7$ m, $x_c / r_a = 0.0$, $\varepsilon_1 = 15\varepsilon_0$ F/m, $\mu_1 = \mu_0$ H/m, $\phi_i = 60^\circ$, and $\sigma_1 = 0.01$ Sm^{-1}

After determining the method's accuracy, the PEC object is chosen as a cylinder with elliptical cross-section in Figure 4.20. The effect of the incident angle is noticeable on the scattered amplitude in Figure 4.21. There is a reduction of the magnitude of the scattered field as the incident angle deviates from 90°. Also, if the object depth h_c increases, the scattered field magnitude reduces as shown in Figure 4.22.

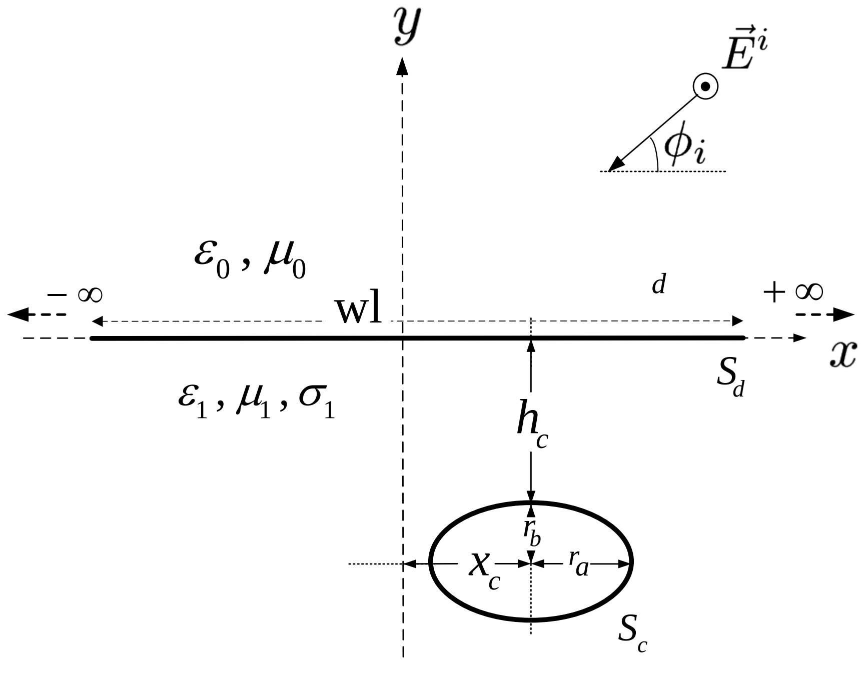

Figure 4. 20 A cylindrical object with elliptical cross-section

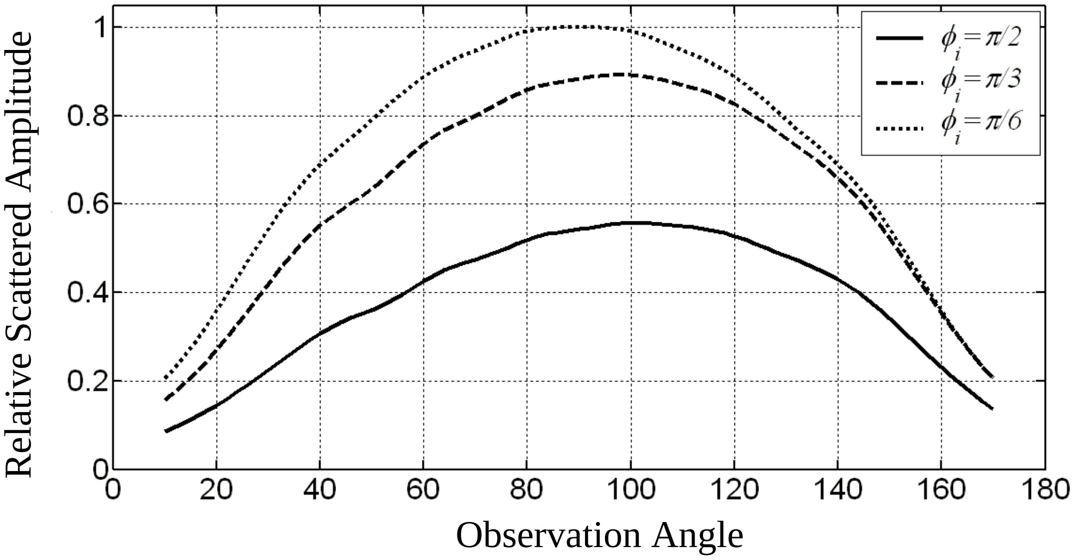

Figure 4. 21 Relative scattered amplitude from a PEC cylindrical object with elliptical cross-section for f=1 GHz, $r_a = 0.2$ m, $r_b = 0.1$ m, $h_c / r_b = 1.0$, $x_c / r_a = 0.0$, $\varepsilon_1 = 15\varepsilon_0$ F/m, $\mu_1 = \mu_0$ H/m and $\sigma_1 = 0.01$ Sm^{-1}

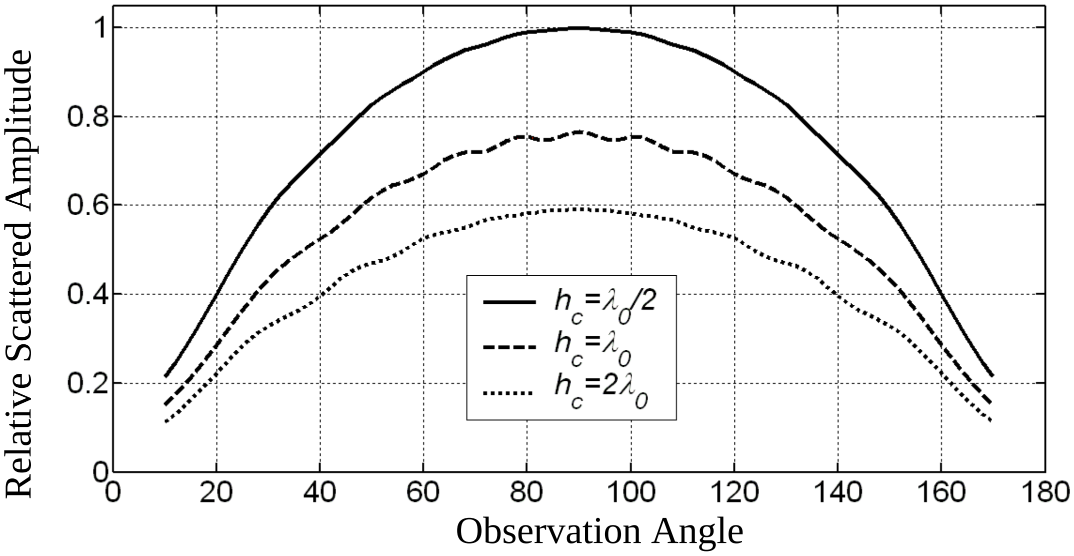

Figure 4. 22 Relative scattered amplitude from a PEC cylindrical object with elliptical cross-section for f=1 GHz, $\phi_i = 90^\circ$, $r_a = 0.2$ m, $r_b = 0.1$ m, $x_c / r_a = 0.0$, $\varepsilon_1 = 15\varepsilon_0$ F/m, $\mu_1 = \mu_0$ H/m and $\sigma_1 = 0.01$ Sm^{-1}

In Figure 4.23, the object is chosen as a cylinder having different dielectric constant. The scattered energy is concentrated around a scattering angle of 90° even for very small incident angle. It is also observed that the difference between the dielectric constant (ε_{r2} is the relative dielectric constant of the object) of the cylinder and the medium is effective on the scattered field amplitude.

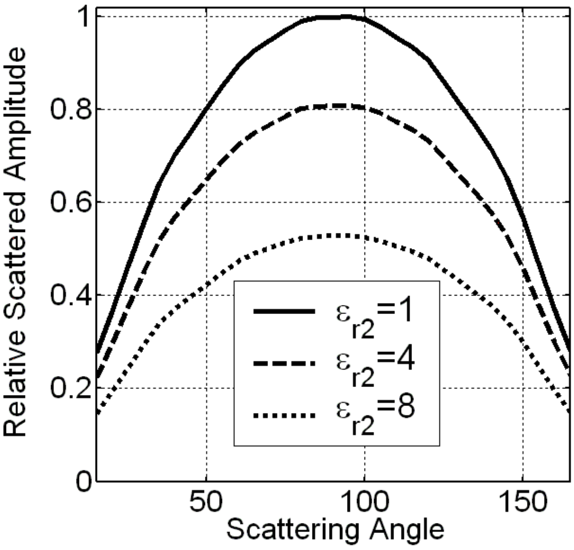

Figure 4. 23 Scattered amplitude from a dielectric cylindrical scatterer with circular cross-section for $r_a = 0.01$ m, $h_c = 0.01$ m, $x_c / r_a = 0.0$, $\varepsilon_1 = 15\varepsilon_0$ F/m, $\mu_1 = \mu_2 = \mu_0$ H/m, $\phi_i = 30^\circ$, $\sigma_1 = 0.01$ Sm^{-1} and $\sigma_2 = 0.0$ Sm^{-1}

CHAPTER 5

COMPUTATION OF TM$_z$ SCATTERING FROM AN OBJECT BURIED IN A MEDIUM WITH A PERIODIC SURFACE BY A PERTURBATION METHOD

5.1 Introduction

In this chapter, electromagnetic scattering from a cylindrical object of arbitrary cross-section buried in a lossy dielectric half-space having a periodic surface (Figure 5.1) is investigated by the perturbation method. The surface equivalence principle and the perturbation method are employed to form a set of EFIEs for the currents on the object and the portion of the surface most strongly interacting with the object. Then, MoM is used to solve the EFIEs in the frequency domain to obtain the scattered electric.

5.2 Theory

The electric field value on the object points when the object is absent ($\vec{E}_{int}^{I}$ on S_c^-) is calculated by using the transmission coefficient for the flat surface problem. But for a rough surface, this electric field can be obtained by an integral equation formulation [30, 31]. Continuity of tangential $\vec{E}$ and $\vec{H}$ on the surface lead to

$$E_{z2} = E_{z1} = E_z \tag{5.1}$$

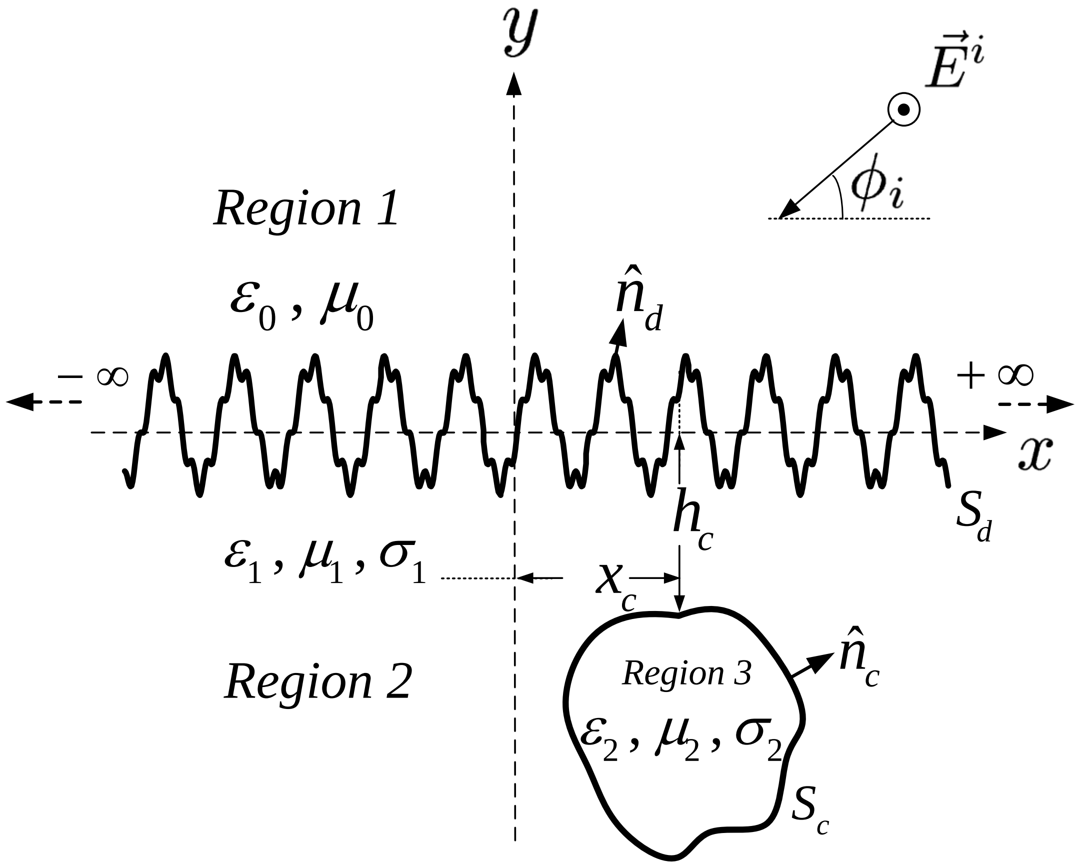

Figure 5. 1 Geometry of cylindrical object buried inside a lossy half-space with periodic surface

$$\frac{\partial E_{z2}}{\partial n_d} = \frac{\mu_1}{\mu_0}\frac{\partial E_{z1}}{\partial n_d} = \frac{\mu_1}{\mu_0}\frac{\partial E_z}{\partial n_d} \tag{5.2}$$

For calculating the field in Region 2, Region 1 is replaced with the equivalent polarization currents $\vec{J}_{eq}^{(1)} = j\omega\left(\varepsilon_0 - \varepsilon_{c1}\right)\vec{E}_1$ in a medium having wave number k_1. Applying 2-D Green's theorem, the field in Region 2 includes just scattered field

$$E_{z2}\left(\vec{\rho}\right) = -\int_{C_p}\left[E_{z2}\left(\vec{\rho}'\right)\frac{\partial G_2\left(\vec{\rho},\vec{\rho}'\right)}{\partial n_d'} - G_2\left(\vec{\rho},\vec{\rho}'\right)\frac{\partial E_{z2}\left(\vec{\rho}'\right)}{\partial n_d'}\right]dl' \tag{5.3}$$

where C_p is the surface contour in its first period, and the periodic Green's function

$$G_2\left(\vec{\rho},\vec{\rho}'\right) = -\frac{j}{2w_p}\sum_{n=-\infty}^{\infty}\frac{e^{-j\beta_n\left(x-x'\right)}e^{-jq_{2n}\left(y-y'\right)}}{q_{2n}} \tag{5.4}$$

where w_p is the length of one period, $\beta_n = \beta + 2n\pi / w_p$, $q_{2n}^2 = k_1^2 - \beta_n^2$, and $\beta = k_1 \sin\phi_i$.

For the field in Region 1, Region 2 is replaced with the equivalent polarization currents $\vec{J}_{eq}^{(2)} = j\omega(\varepsilon_{c1} - \varepsilon_0)\vec{E}_2$ in a medium having wave number k_0. The field in Region 1 includes both scattered field and the incident field

$$E_{z1}(\vec{\rho}) = E^i(\vec{\rho}) + \int_{C_p}\left[E_{z1}(\vec{\rho}')\frac{\partial G_1(\vec{\rho},\vec{\rho}')}{\partial n_d'} - G_1(\vec{\rho},\vec{\rho}')\frac{\partial E_{z1}(\vec{\rho}')}{\partial n_d'}\right]dl' \qquad (5.5)$$

After using equations (5.1) and (5.2) in equation (5.3) and (5.5)

$$E_z(\vec{\rho}) = -\int_{C_p}\left[E_z(\vec{\rho}')\frac{\partial G_2(\vec{\rho},\vec{\rho}')}{\partial n_d'} - G_2(\vec{\rho},\vec{\rho}')\frac{\mu_1}{\mu_0}\frac{\partial E_z(\vec{\rho}')}{\partial n_d'}\right]dl' \qquad (5.6)$$

$$E_z(\vec{\rho}) = E^i(\vec{\rho}) + \int_{C_p}\left[E_z(\vec{\rho}')\frac{\partial G_1(\vec{\rho},\vec{\rho}')}{\partial n_d'} - G_1(\vec{\rho},\vec{\rho}')\frac{\partial E_z(\vec{\rho}')}{\partial n_d'}\right]dl' \qquad (5.7)$$

When $\vec{\rho}$ is a point on the surface

$$\frac{E_z(\vec{\rho})}{2} = -PV\int_{C_p}\left[E_z(\vec{\rho}')\frac{\partial G_2(\vec{\rho},\vec{\rho}')}{\partial n_d'} - G_2(\vec{\rho},\vec{\rho}')\frac{\mu_1}{\mu_0}\frac{\partial E_z(\vec{\rho}')}{\partial n_d'}\right]dl' \qquad (5.8)$$

$$\frac{E_z(\vec{\rho})}{2} = E^i(\vec{\rho}) + PV\int_{C_p}\left[E_z(\vec{\rho}')\frac{\partial G_1(\vec{\rho},\vec{\rho}')}{\partial n_d'} - G_1(\vec{\rho},\vec{\rho}')\frac{\mu_1}{\mu_0}\frac{\partial E_z(\vec{\rho}')}{\partial n_d'}\right]dl' \qquad (5.9)$$

where *PV* indicates principal value sense integration at field points $\vec{\rho}' = \vec{\rho}$. Equation (5.8) and (5.9) is a pair of integral equations. These equations can be solved numerically by MoM to calculate the unknown field and its normal derivative. Then, the field in Region 2 is obtained by

$$E_{z2}(\vec{\rho}) = -\int_{C_p}\left[E_z(\vec{\rho}')\frac{\partial G_2(\vec{\rho},\vec{\rho}')}{\partial n_d'} - G_2(\vec{\rho},\vec{\rho}')\frac{\mu_1}{\mu_0}\frac{\partial E_z(\vec{\rho}')}{\partial n_d'}\right]dl' \qquad (5.10)$$

where E_{z2} is equal to $\vec{E}_{int}^{I}$.

There are four equations that are mentioned in equations (4.47)-(4.50) to be solved by using MoM and four unknown currents to calculate the scattered field.

5.3 Numerical Results

For simplicity, the boundary interface $y(x)$ defined by

$$y(x) = h_p \cos\left(2\pi x/w_p\right) \tag{5.11}$$

where h_p and w_p are the height and width of one period of the surface. The object is chosen to be a dielectric cylinder with circular cross-section of radius r_a as shown in Figure 5.2.

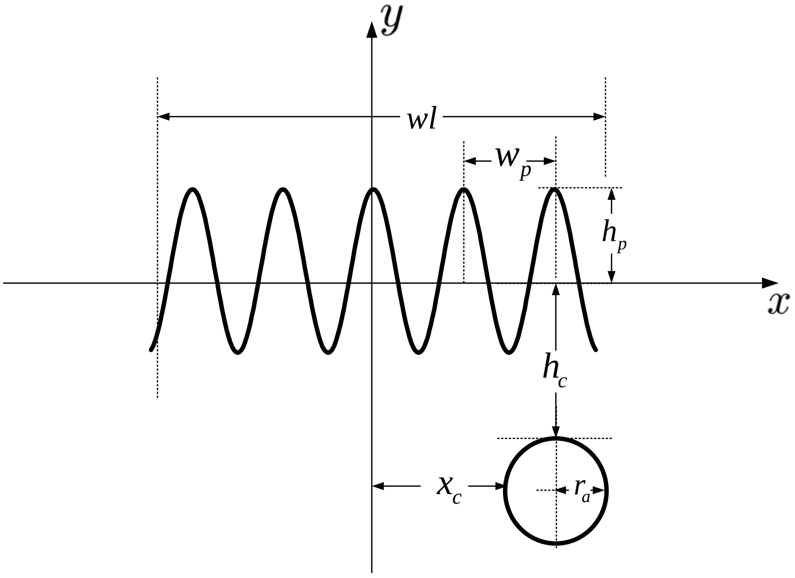

Figure 5. 2 The geometry used for the numerical results

The perturbation currents' behaviours are investigated in Figure 5.3 to validate the assumption that the equivalent current on the surface will be affected only in a finite portion of the surface near the object. As expected, when the object is buried deeper, the perturbation currents spread along the surface. Also, because of the conductivity of the half-space, the interactions between the cylinder and the periodic surface reduce. Therefore, the amplitudes of the perturbation currents decrease.

To determine the accuracy of the method, the space parameters under the surface are chosen as (ε_0, μ_0). Thus, the scattered field is expected to behave like a dielectric cylinder. The scattered E-field is first solved by perturbation method, and then by analytical method. Then, these two results are compared in Figure 5.4.

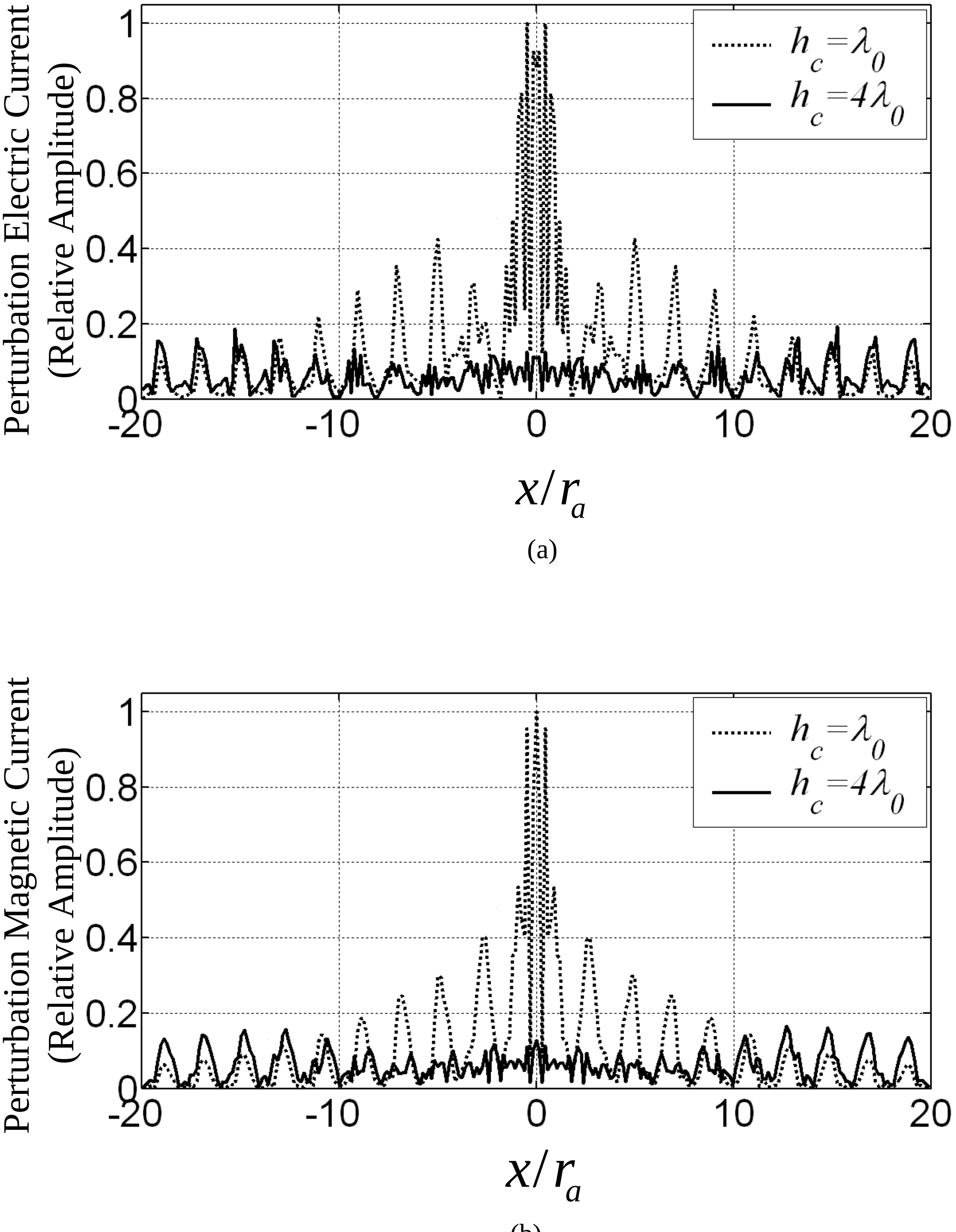

(a)

(b)

Figure 5. 3 Perturbation (a) electric currents normalized with 0.0045 A/m and (b) magnetic currents normalized with 0.91 V/m on the surface for $f=1$ GHz, $\phi_i=\phi_s=90^\circ$, $r_a=\lambda_0/3$ m, $wl/r_a=40$, $w_p=2\lambda_0/3$ m, $h_p/w_p=0.25$, $x_c/r_a=0.0$, $\varepsilon_1=15\varepsilon_0$ F/m, $\varepsilon_2=2.25\varepsilon_0$ F/m, $\mu_1=\mu_2=\mu_0$ H/m, $\sigma_1=0.001$ Sm^{-1} and $\sigma_2=0.0$ Sm^{-1}

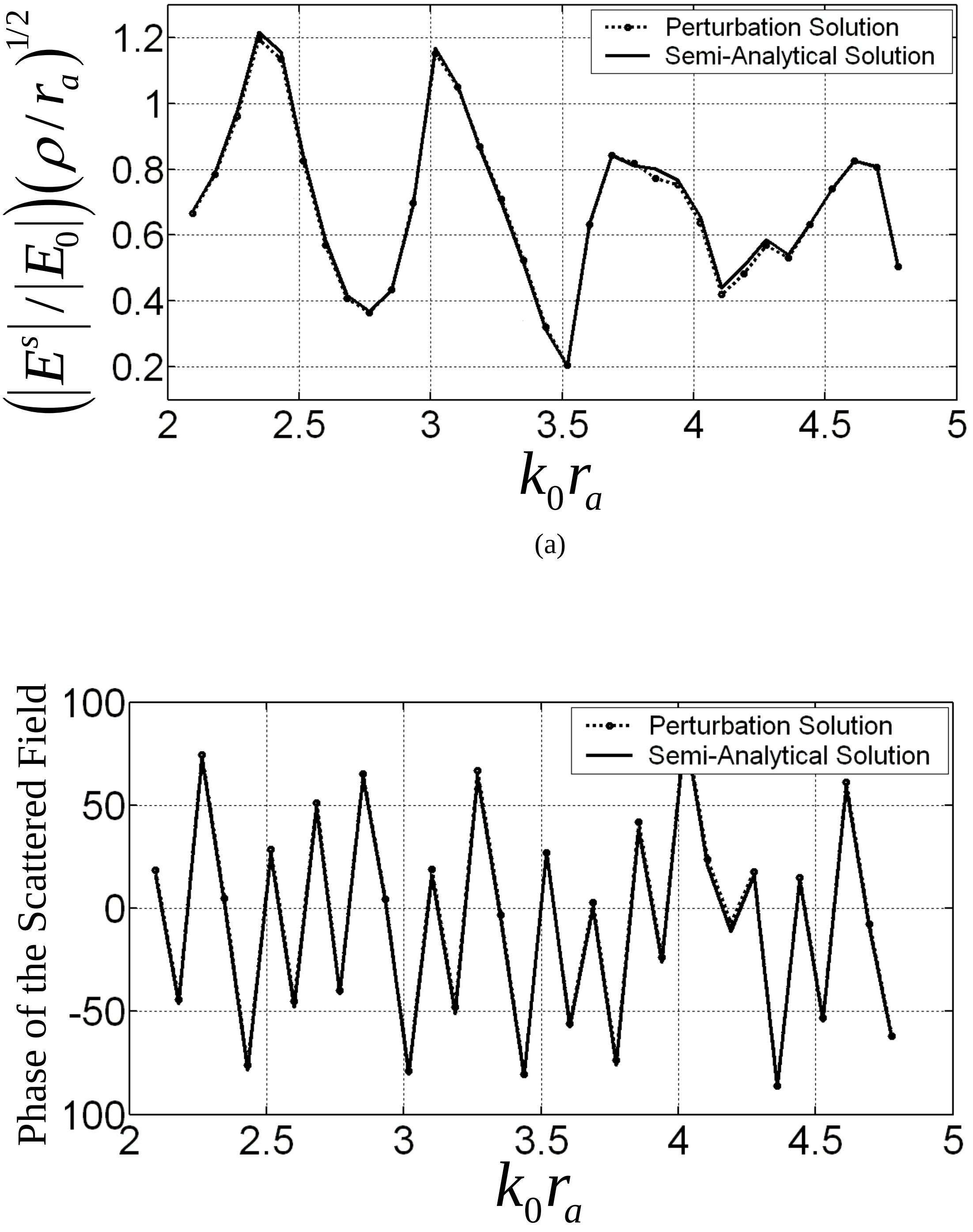

(a)

(b)

Figure 5. 4 Scattered field (a) normalized amplitude and (b) phase for $\phi_i = \phi_s = 90^\circ$, $r_a = 0.1$ m, $w_p = 0.2$ m, $h_p / w_p = 0.25$, $x_c / r_a = 0.0$, $h_c / r_a = 5.0$, $wl / r_a = 50$, $\varepsilon_1 = \varepsilon_0$ F/m, $\varepsilon_2 = 4\varepsilon_0$ F/m, $\mu_1 = \mu_2 = \mu_0$ H/m, and $\sigma_1 = \sigma_2 = 0.0$ Sm^{-1}

The RMS error is calculated for different number of point per wavelength (ppw), and shown in Figure 5.5. It is seen that the solution becomes more accurate for increasing truncation width and ppw. The convergence of the method with respect to ppw is similar to typical integral equations based approaches [32].

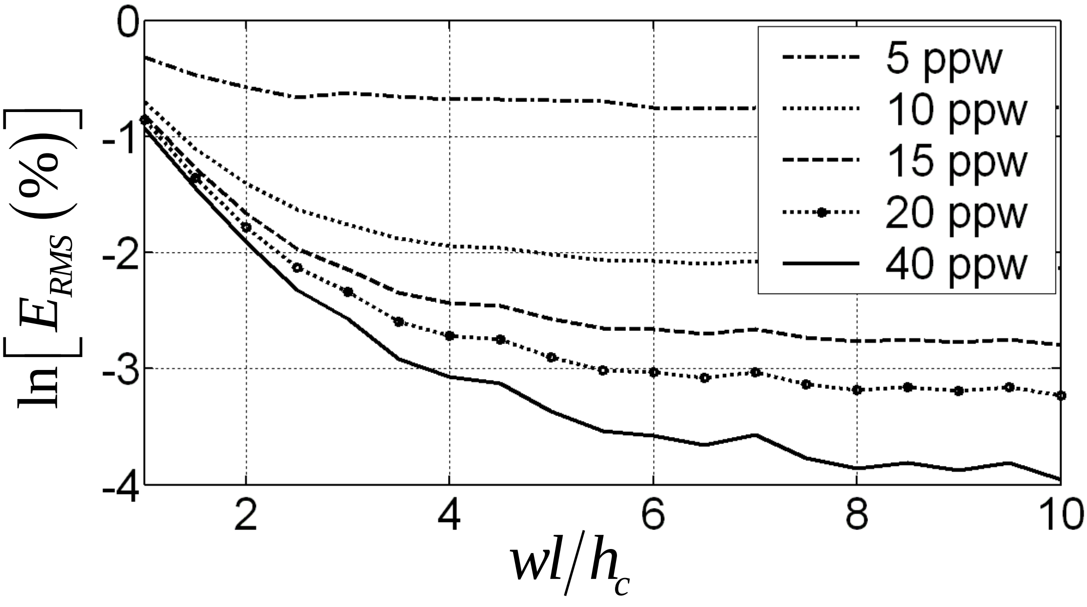

Figure 5. 5 The approximation difference for $f = 1$ GHz, $\phi_i = \phi_s = 90^\circ$, $r_a = \lambda_0/3$ m, $w_p = 2\lambda_0/3$ m, $h_p/w_p = 0.25$, $x_c / r_a = 1.0$, $h_c / \mathrm{r}_a = 5.0$, $\varepsilon_1 = \varepsilon_0$ F/m, $\varepsilon_2 = 4\varepsilon_0$ F/m, $\mu_1 = \mu_2 = \mu_0$ H/m, and $\sigma_1 = \sigma_2 = 0.0$ Sm^{-1}

Also, the results of the proposed method are compared with another method by considering a dielectric circular cylinder buried beneath a sinusoidal slightly rough surface. Then, the parameters are chosen as exactly the same with those given in [17]. The surface represents by $y(x) = h_p \cos\left(2\pi x/w_p\right)$. Figure 5.6-5.13 demonstrate the effect of a sinusoidal surface for $f = 400$ MHz, $\phi_i = 30^\circ$, $h_p = 0.0064\lambda_0$, $x_c / r_a = 0.0$, $h_c = 1.3\lambda_0$, $wl/h_c = 10$, $\varepsilon_{c1} = (4 - j0.01)\varepsilon_0$ F/m, $\varepsilon_2 = 2.25\varepsilon_0$ F/m, $\mu_1 = \mu_2 = \mu_0$ H/m, and $\sigma_2 = 0.0$ Sm^{-1}. Obviously, radar cross section (RCS) of these examples in Figure 5.6-5.13 matches those given in [17].

The period of the surface is varied from $0.25\lambda_0$ to $2\lambda_0$ in Figure 5.6-5.9. The scattering pattern for $w_p = 0.25\lambda_0$ is almost identical to that of a flat surface as seen in Figure 5.6. In Figure 5.7 and 5.8, the scattering pattern is significantly changed for $w_p = 0.4\lambda_0$ and $w_p = 0.6\lambda_0$. In Figure 5.9, the scattering pattern once again approaches that of a flat surface for $w_p = 2\lambda_0$. So, the scattering pattern is only significantly affected by a range of surface frequencies.

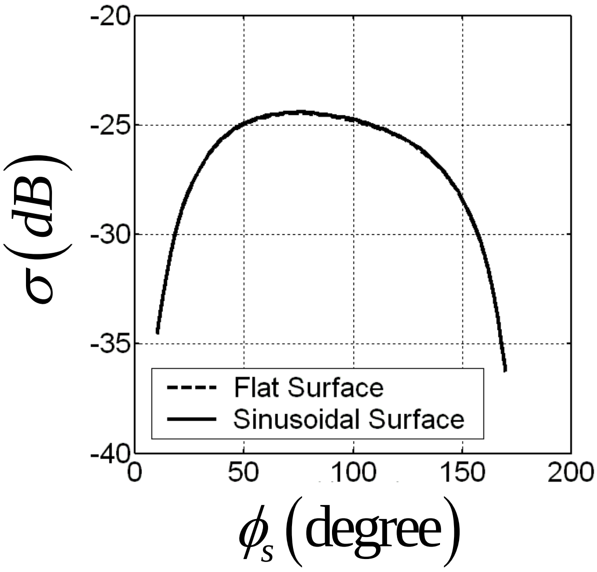

Figure 5. 6 Scattered amplitude from a cylindrical scatterer with circular cross-section for $r_a = 0.16\lambda_0$ m, $w_p = 0.25\lambda_0$ m

The simulations are repeated for various size of the buried object in Figure 5.10-5.13 and it is shown that surface roughness outside a limited range of frequencies does not affected the scattering pattern of a larger buried object.

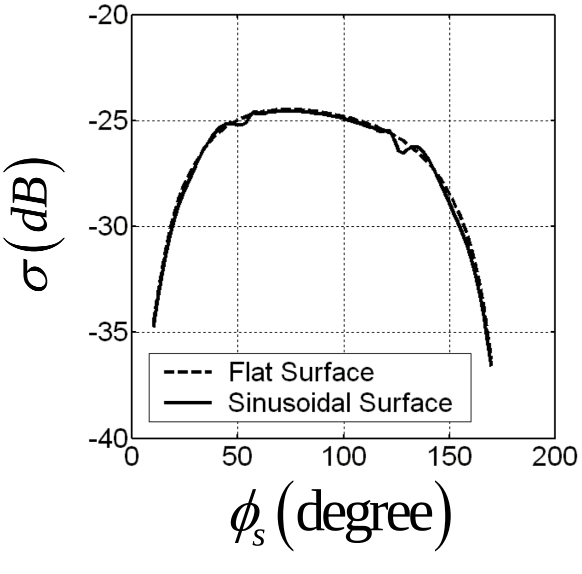

Figure 5. 7 Scattered amplitude from a cylindrical scatterer with circular cross-section for $r_a = 0.16\lambda_0$ m, $w_p = 0.4\lambda_0$ m

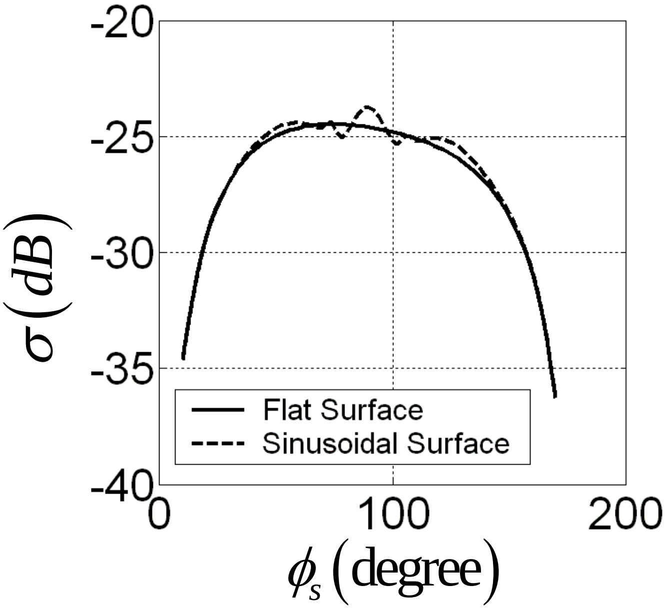

Figure 5. 8 Scattered amplitude from a cylindrical scatterer with circular cross-section for $r_a = 0.16\lambda_0$ m, $w_p = 0.6\lambda_0$ m

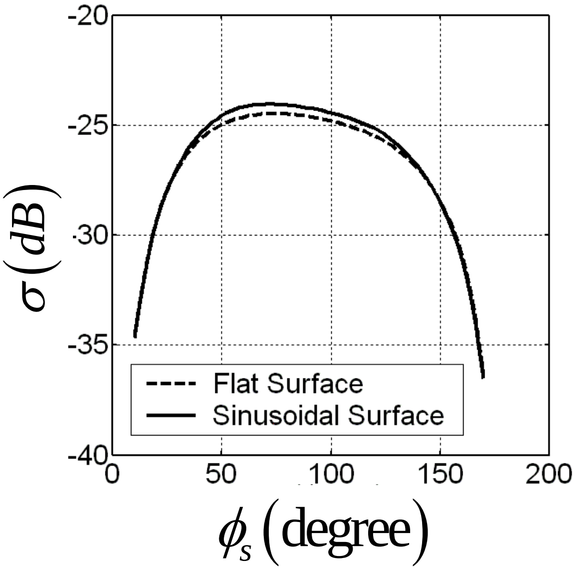

Figure 5. 9 Scattered amplitude from a cylindrical scatterer with circular cross-section for $r_a = 0.16\lambda_0$ m, $w_p = 2\lambda_0$ m

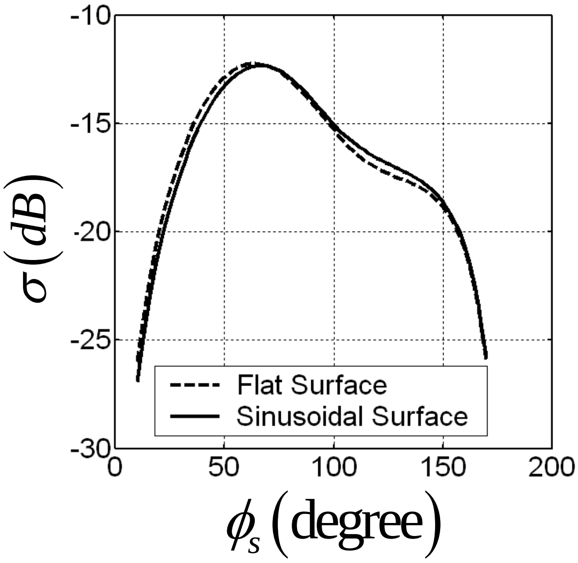

Figure 5. 10 Scattered amplitude from a cylindrical scatterer with circular cross-section for $r_a = 1.0\lambda_0$ m, $w_p = 0.25\lambda_0$ m

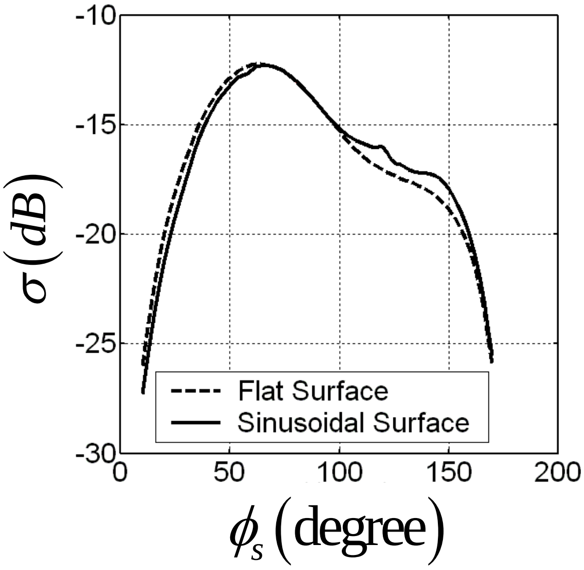

Figure 5. 11 Scattered amplitude from a cylindrical scatterer with circular cross-section for $r_a = 1.0\lambda_0$ m, $w_p = 0.4\lambda_0$ m

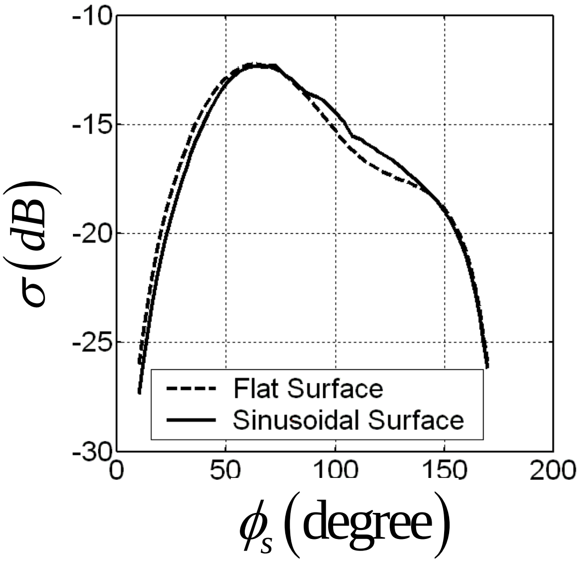

Figure 5. 12 Scattered amplitude from a cylindrical scatterer with circular cross-section for $r_a = 1.0\lambda_0$ m, $w_p = 0.6\lambda_0$ m

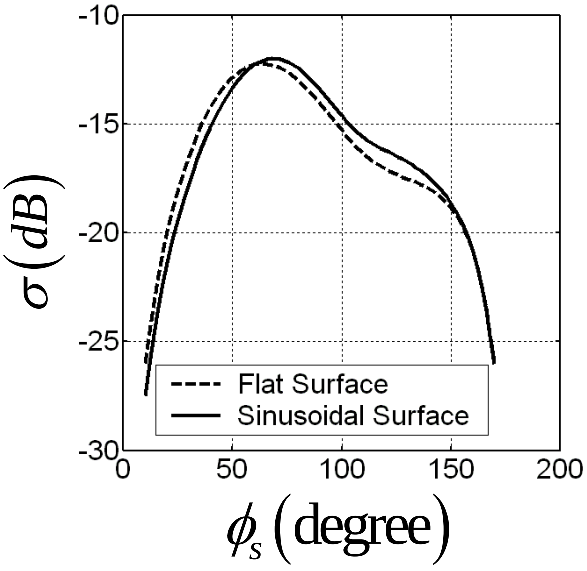

Figure 5. 13 Scattered amplitude from a cylindrical scatterer with circular cross-section for $r_a = 1.0\lambda_0$ m, $w_p = 2.0\lambda_0$ m

The root-mean square error for a lossy media is calculated by using the convergence value of the scattered field (E_L^P) for a very large truncation width

$$E_{RMS}(\%)\Big|_{lossy} = \sqrt{\frac{\left|E_L^P - E^P\right|^2}{\left|E_L^P\right|^2}} \tag{5.12}$$

Then, the RMS error is calculated and shown in Figure 5.14. It is seen that the solution becomes more accurate for increasing truncation width.

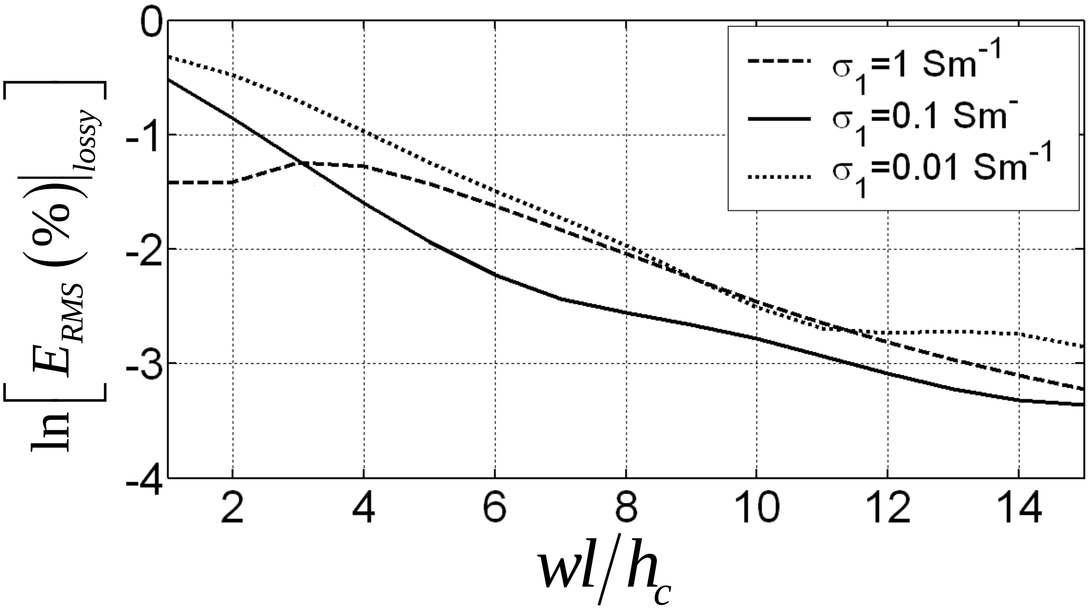

Figure 5. 14 The approximation difference for $f = 400$ MHz, $\phi_i = 30^\circ$, $r_a = 0.16\lambda_0$ m, $w_p = 0.6\lambda_0$ m, $h_p = 0.0064\lambda_0$, $x_c / r_a = 0.0$, $h_c = 0.17\lambda_0$, $wl/h_c = 10$, $\varepsilon_{c1} = (4 - j0.01)\varepsilon_0$ F/m, $\varepsilon_2 = 2.25\varepsilon_0$ F/m, $\mu_1 = \mu_2 = \mu_0$ H/m, and $\sigma_2 = 0.0$ Sm^{-1}

Figure 5.15 shows the influence of the target size and location on the electromagnetic scattering. When the object is shifted in *x*-direction to the right, the object gets closer to the periodic surface. As expected, the scattered field amplitude increases. If the object is buried deeper, the field propagates more distance in lossy media. As a result, attenuation of the field increases. In addition, the size of the object gets smaller, RCS reduces. Therefore, the amplitude of the scattered field decreases.

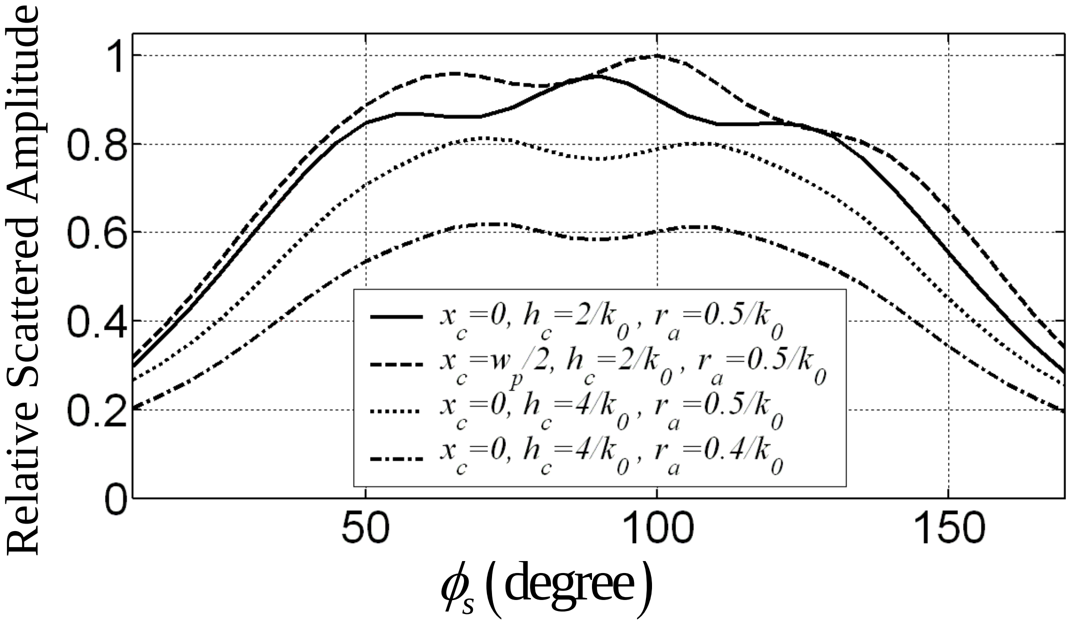

Figure 5. 15 Relative scattered amplitude from a cylindrical scatterer with circular cross-section for $f = 100$ MHz, $\phi_i = 20^\circ$, $w_p = 2/k_0$ m, $h_p = 0.2/k_0$, $wl/h_c = 10$, F/m, $\varepsilon_1 = 4\varepsilon_0$ F/m, $\varepsilon_2 = \varepsilon_0$ F/m, $\mu_1 = \mu_2 = \mu_0$ H/m, $\sigma_1 = 0.001$ Sm^{-1} and $\sigma_2 = 0.0$ Sm^{-1}

CHAPTER 6

TIME DOMAIN ANALYSIS

6.1 Introduction

The perturbation method to calculate scattered fields from a buried object is outlined in Chapter 4 and Chapter 5. This method can be useful for ground-penetrating radar applications. In order to investigate the usage of this method, the analysis of transient scattering for TM_z polarization from a cylindrical object buried in a lossy medium is considered in this chapter. The possible paths traveled by the reflected waves and the multiple reflections are identified by using timing analysis.

The incident signal is constructed from a frequency spectrum of 1-30 GHz with 726 data points. This frequency data is weighted using a double Gaussian function with the values of $\tau_1 = 0.04\times10^{-9}$ and $\tau_2 = 0.0625\times10^{-9}$ and shown in Figure 6.1a. Then, the weighted frequency data transformed into time domain using an inverse Fourier transform. The resulting transient incident TM_z signal is shown in Figure 6.1b.

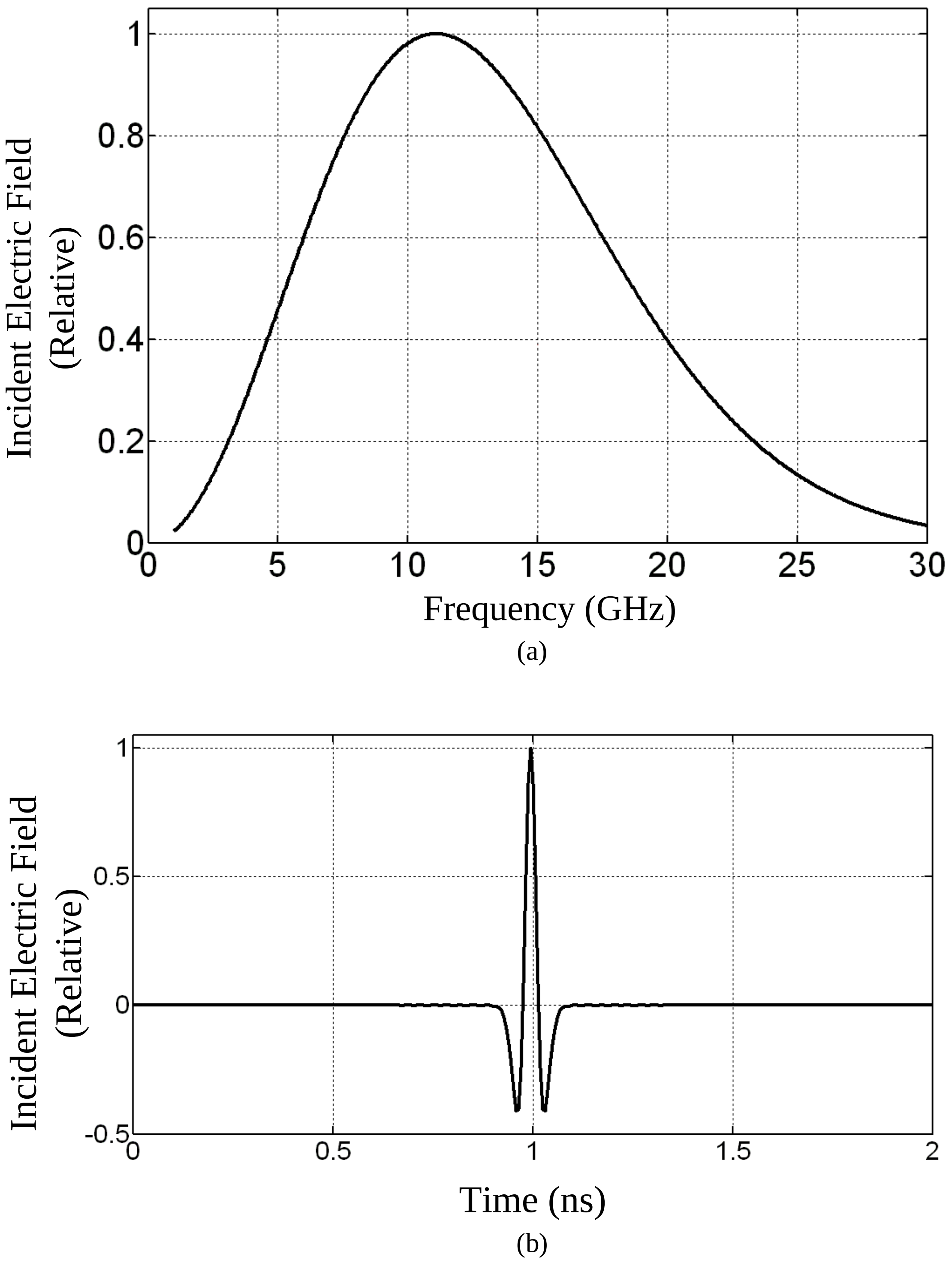

Figure 6. 1 The incident E-field waveform a) in frequency domain b) in time domain

6.2 Time Domain Results

The backscattered field from a PEC cylinder is shown in both the frequency and time domains in Figure 6.2. As expected the reflected field has a sign change because of a single reflection from a PEC surface seen in time domain result in Figure 6.2b.

The backscattered field from a buried PEC cylinder is shown in both the frequency and time domains in Figure 6.3. As seen in time domain results in Figure 6.3b, there are two reflections, one coming from the cylinder (L_1) and one coming from the flat surface-cylinder-flat surface path (L_2) seen in Figure 6.4. The time passing between these two reflections is calculated by

$$\Delta t_n = \frac{\left(L_{n+1} - L_n\right)\sqrt{\varepsilon_{r1}}}{c} \tag{6.1}$$

where ε_{r1} is the relative permittivity of the medium and c is the speed of light in space [33].

In Figure 6.3, $L_2 = 4h_c$, $L_1 = 2h_c$ and ε_{r1} is chosen as 15, so Δt_1 is calculated as 2.582 ns. The relative time Δt_1 found from Figure 6.3b is 2.594 ns. To investigate the effect of the burial depth of the cylinder, it is located nearer to the surface than the one in Figure 6.3. Then, the backscattered field is calculated and shown in both the frequency and time domains in Figure 6.5. It is observed in Figure 6.5b that the time between the reflections decreases. There are four main reflections following the paths L_1, L_2, L_3, and L_4 as shown in Figure 6.4. Here, $L_1 = 2h_c$, $L_2 = 4h_c$, $L_3 = 6h_c$, $L_4 = 8h_c$. Therefore, $\Delta t_1 = \Delta t_2 = \Delta t_3 = \dfrac{2h_c\sqrt{\varepsilon_{r1}}}{c}$ is equal to 0.2582 ns. The relative times Δt_1, Δt_2 and Δt_3 found from Figure 6.5b are 0.2625 ns, 0.2564 ns and 0.2597 ns, respectively. These are good agreements.

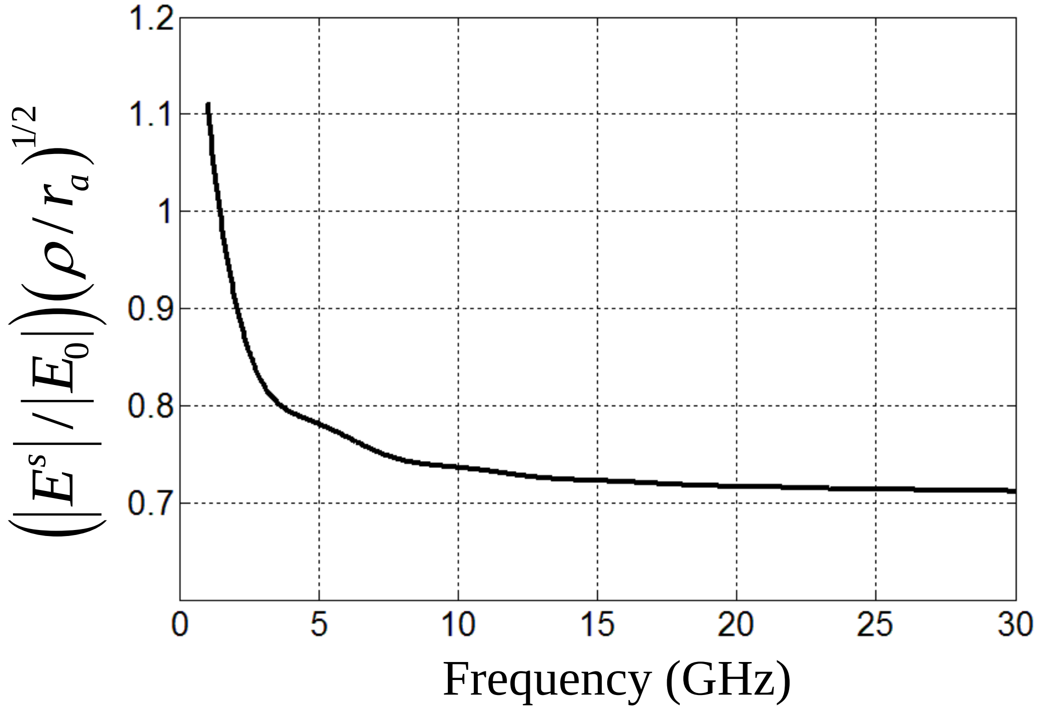

(a)

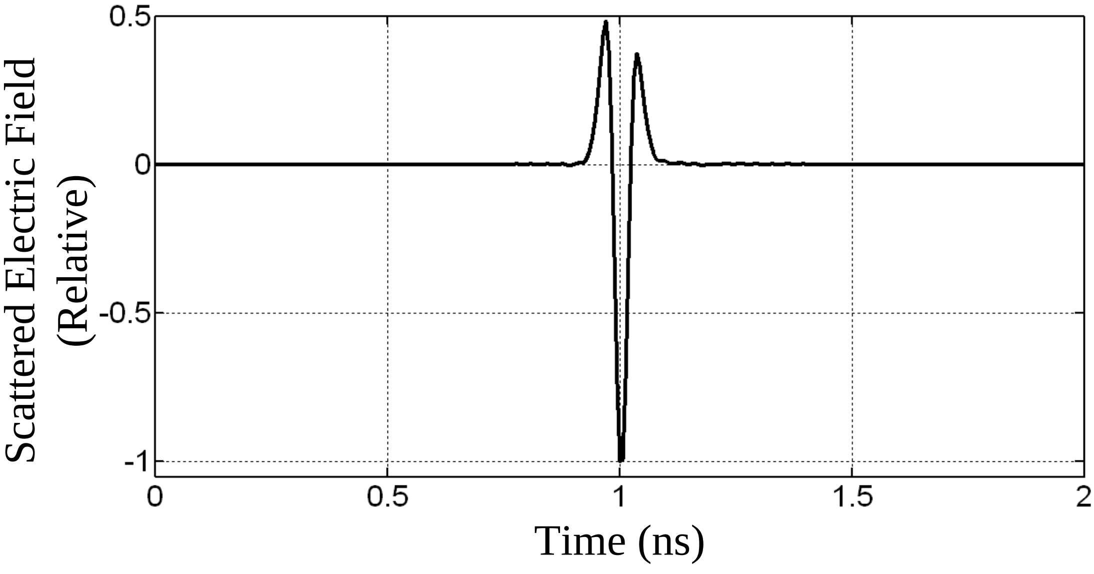

(b)

Figure 6. 2 TM_z backscattered field from a cylindrical PEC object with $r_a = 0.01$ m a) in frequency domain b) in time domain

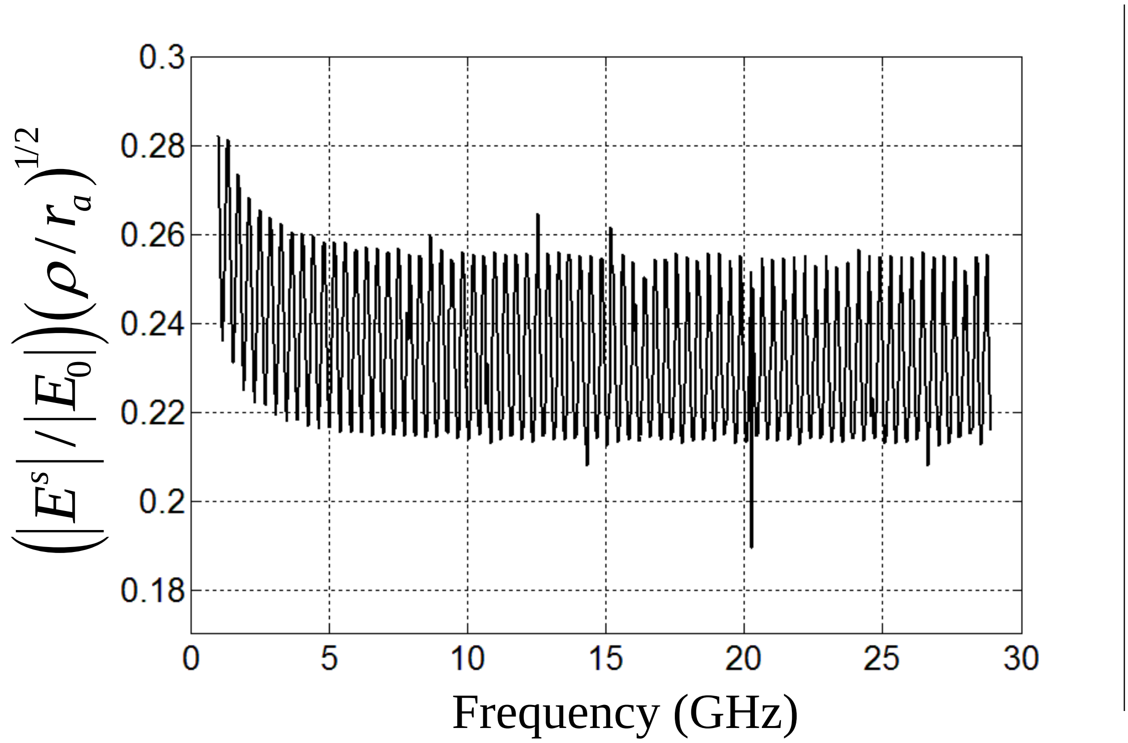

(a)

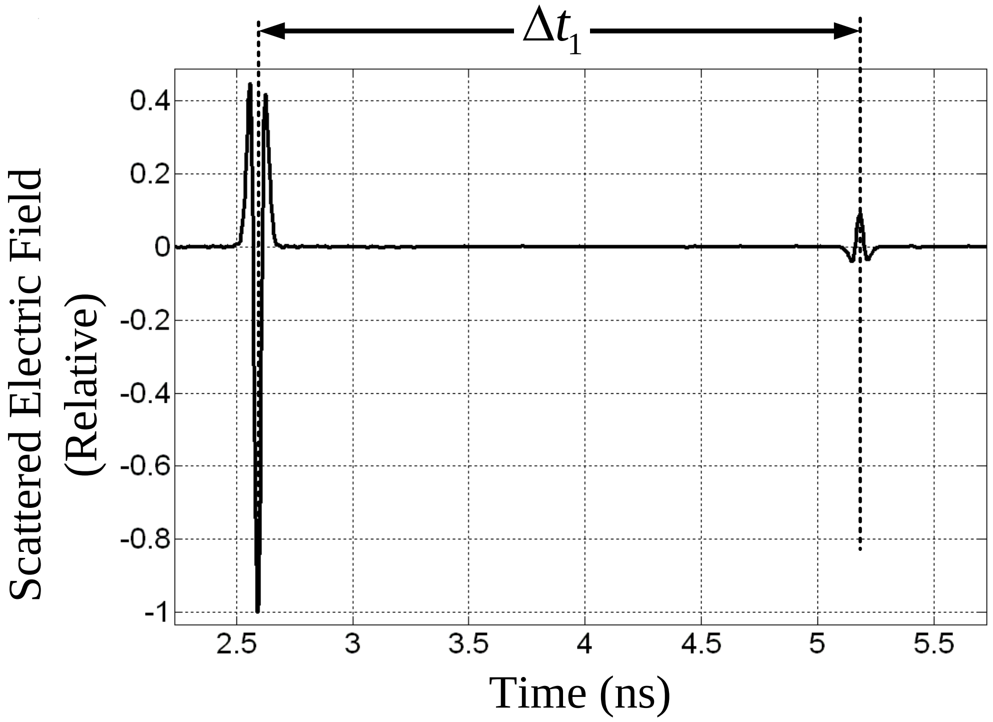

(b)

Figure 6. 3 TM$_z$ backscattered field from a buried cylindrical PEC object for $r_a = 0.01$ m, $h_c = 0.1$ m, $x_c / r_a = 0.0$, $\varepsilon_1 = 15\varepsilon_0$ F/m, $\mu_1 = \mu_0$ H/m, $\phi_i = \phi_s = 90^\circ$, and $\sigma_1 = 0.001$ Sm^{-1} a) in frequency domain, b) in time domain

To investigate effect of the incidence angle on the scattered field, the incident angle is chosen as $\phi_i = 20^\circ$. Then, the backscattered field is calculated and shown in both the frequency and time domains in Figure 6.6. The time between the two main reflections can be calculated by

$$\Delta t_n = \frac{\left(L_{n+1} - L_n\right)\sqrt{\varepsilon_{r1}}}{\sin\left(\phi_t\right)c} \tag{6.2}$$

where ϕ_t is the angle measured from normal of the surface and found $\phi_t = 14^\circ$. Δt_1 is calculated as 2.661 ns. The relative time Δt_1 found from Figure 6.6b is 2.5940 ns.

The effect of the medium loss to the time domain signal is shown in Figure 6.7b. As expected, as the loss of the medium increases, the amplitude of the scattered field decreases.

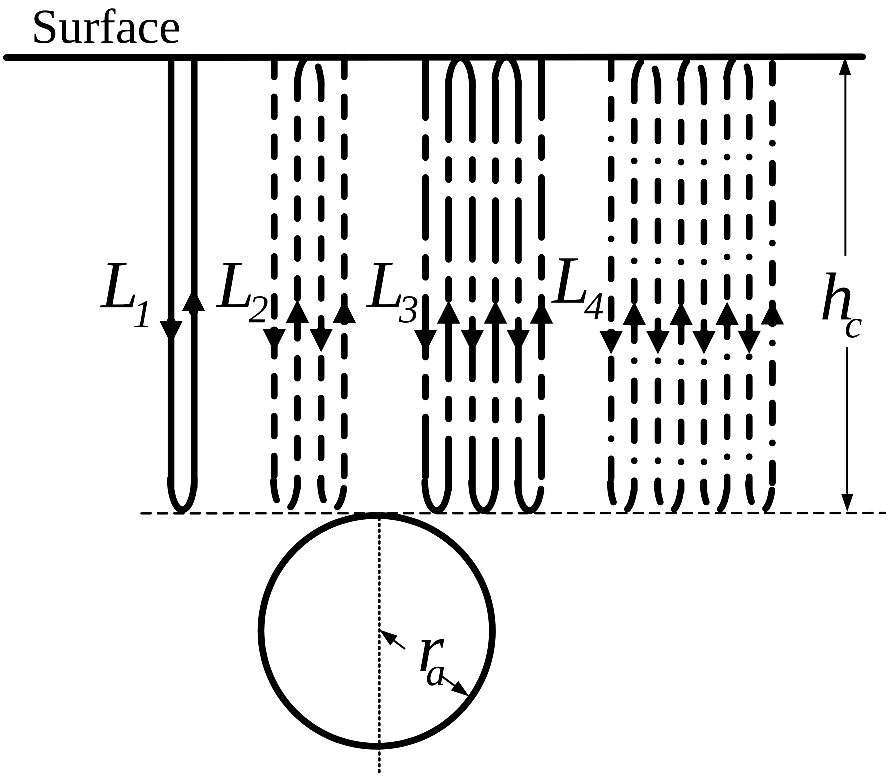

Figure 6. 4 Expected reflections from a buried cylindrical object

The backscattered field from a dielectric cylinder is calculated and shown in both the frequency and time domains in Figure 6.8. It is seen in Figure 6.8b that number of the reflections from the dielectric cylinder increases compared to the PEC cylinder. Because of the time domain answer of the dielectric cylinder, the backscattered field from a buried dielectric cylinder (Figure 6.9b) is much more complicated than the backscattered field from the buried PEC cylinder. Therefore, time domain analysis becomes more difficult to identify the possible paths.

The backscattered field from a PEC cylinder under a slightly rough surface is shown in Figure 6.10 and Figure 6.11. The relative time Δt_1 found from Figure 6.10b and Figure 6.11b is 2.6260 ns and 2.8420 ns; respectively. These time values are similar to the ones in Figure 6.3b and Figure 6.6b, so the beginning of the first group and the last group of reflections are following the paths of L_1 and L_2, respectively. These groups of reflections contain some reflections caused by the surface roughness. However, their paths are difficult to identify.

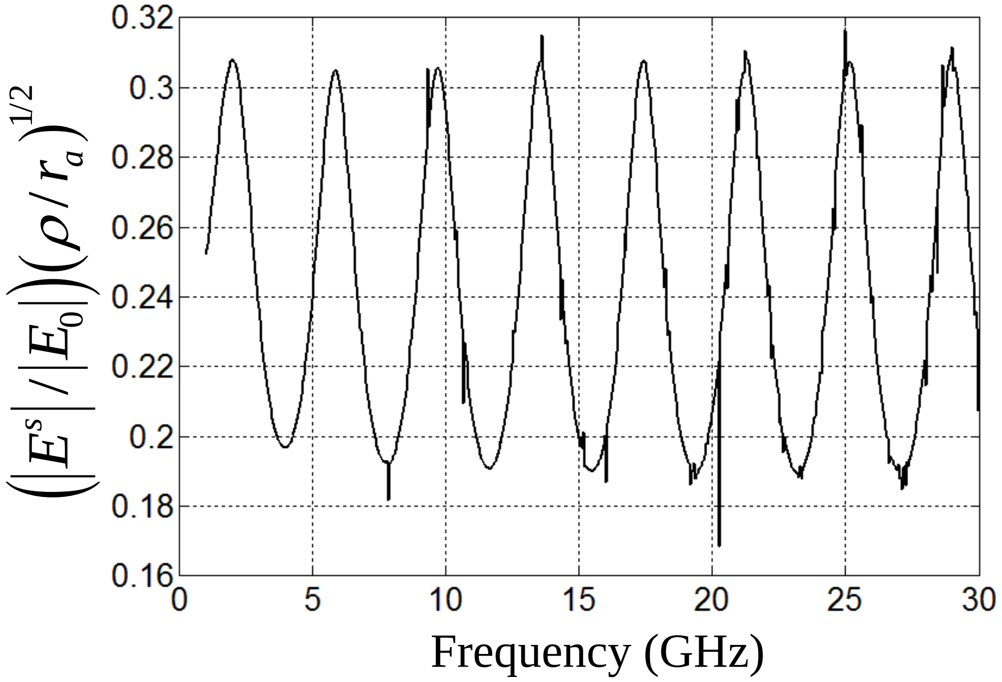

(a)

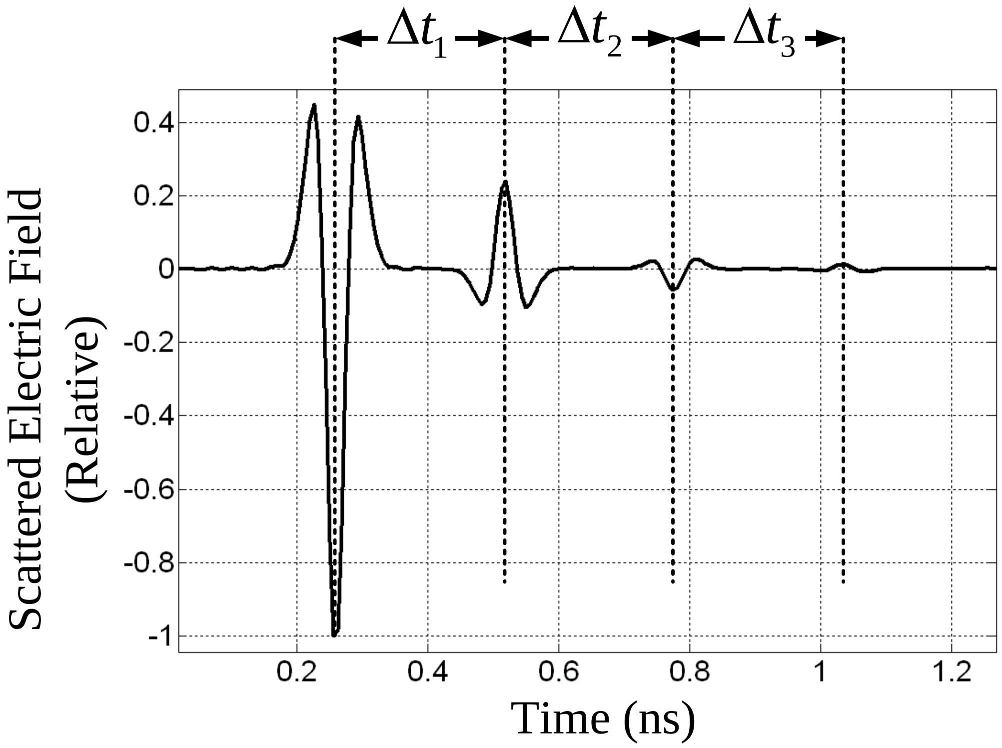

(b)

Figure 6. 5 TM$_z$ backscattered field from a buried cylindrical PEC object for $r_a = 0.01$ m, $h_c = 0.01$ m, $x_c / r_a = 0.0$, $\varepsilon_1 = 15\varepsilon_0$ F/m, $\mu_1 = \mu_0$ H/m, $\phi_i = \phi_s = 90^\circ$, and $\sigma_1 = 0.001$ Sm^{-1} a) in frequency domain, b) in time domain

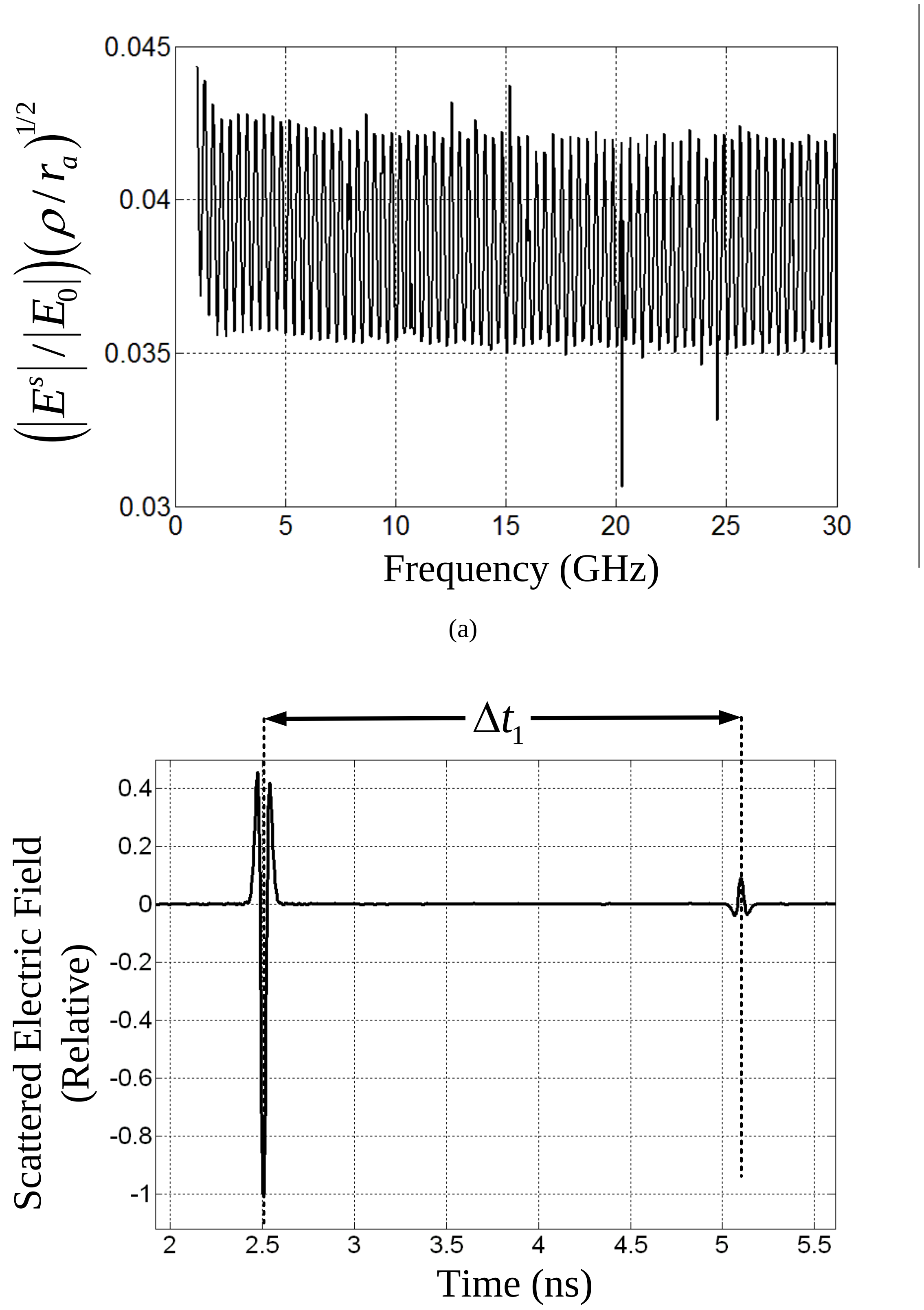

(a)

(b)

Figure 6. 6 TM$_z$ backscattered field from a buried cylindrical PEC object for $r_a = 0.01$ m, $h_c = 0.1$ m, $x_c / r_a = 0.0$, $\varepsilon_1 = 15\varepsilon_0$ F/m, $\mu_1 = \mu_0$ H/m, $\phi_i = \phi_s = 20^\circ$, and $\sigma_1 = 0.001$ Sm^{-1} a) in frequency domain, b) in time domain

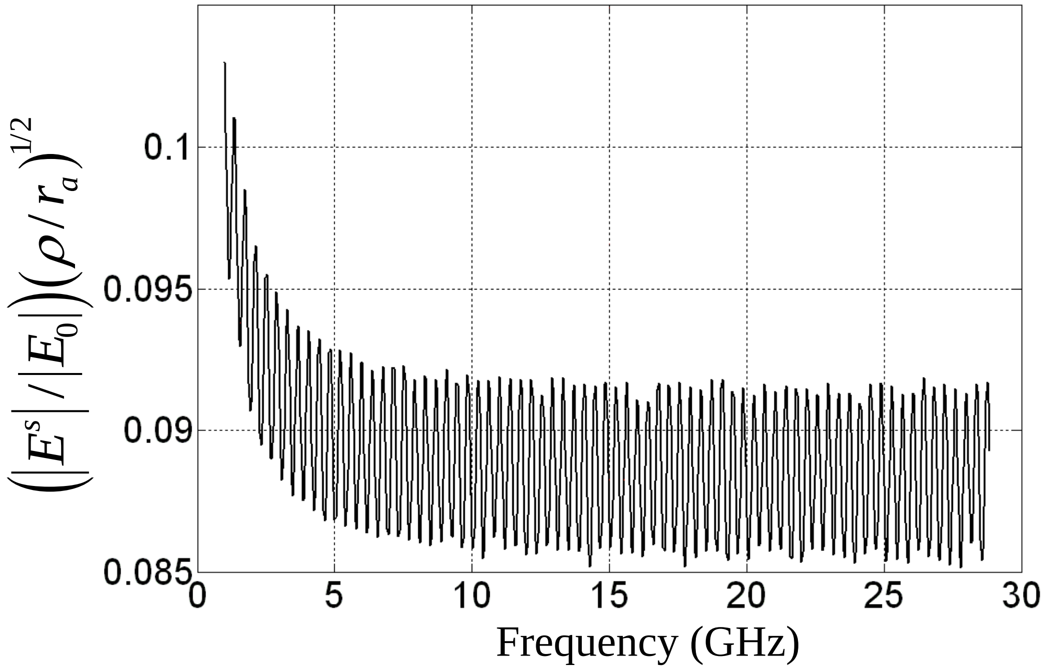

(a)

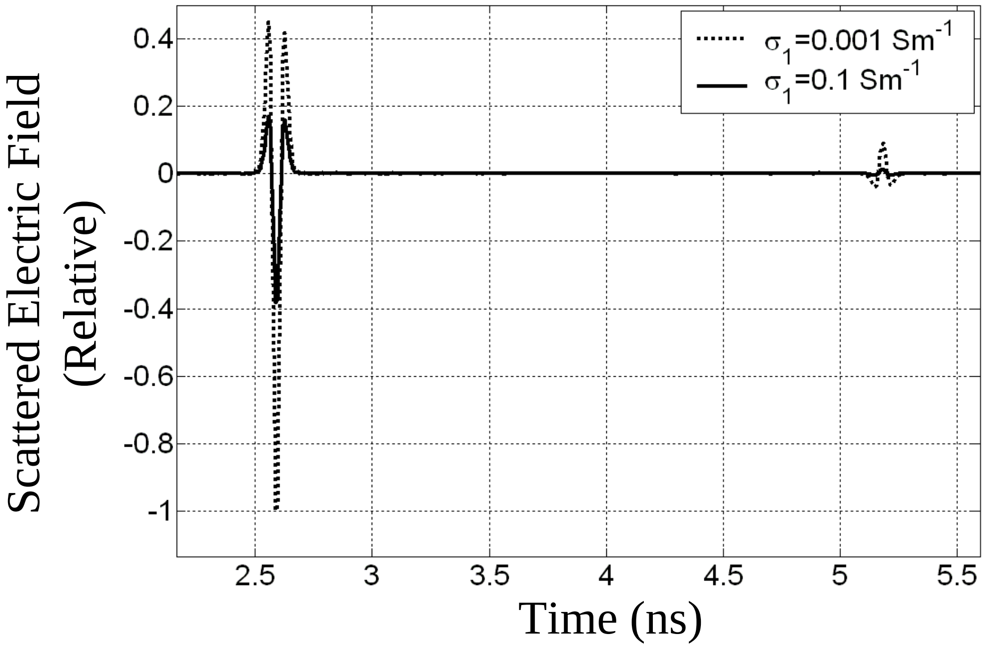

(b)

Figure 6. 7 TM$_z$ backscattered field from a buried cylindrical PEC object for $r_a = 0.01$ m, $h_c = 0.1$ m, $x_c / r_a = 0.0$, $\varepsilon_1 = 15\varepsilon_0$ F/m, $\mu_1 = \mu_0$ H/m, and $\phi_i = \phi_s = 90^\circ$ a) in frequency domain ($\sigma_1 = 0.1$ Sm^{-1}), b) in time domain

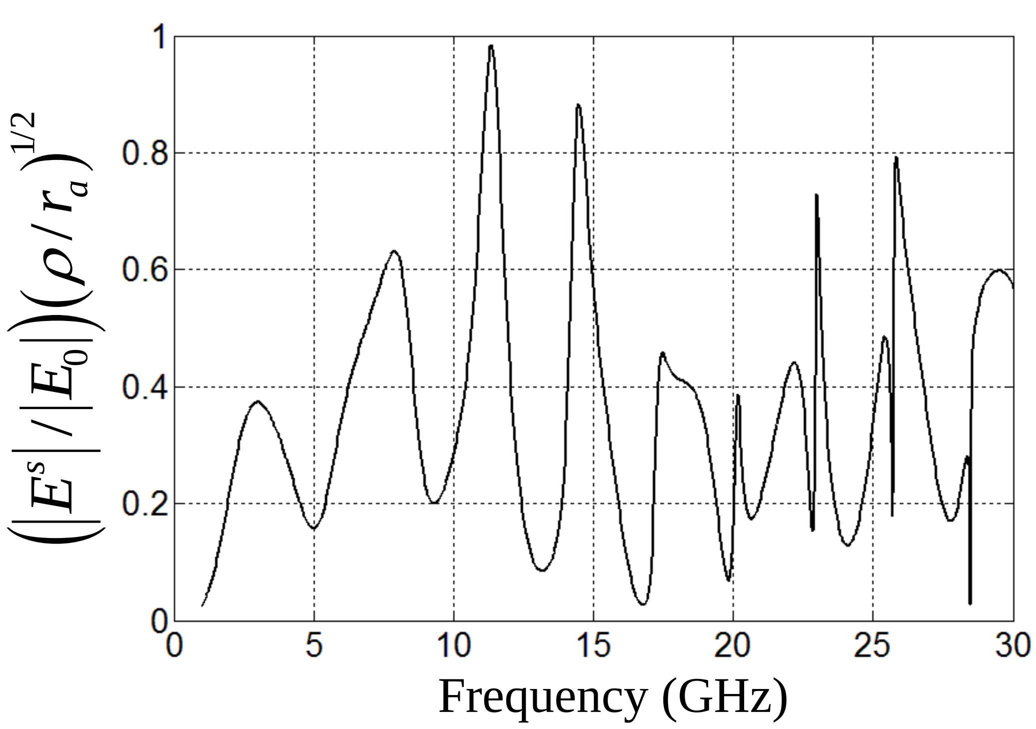

(a)

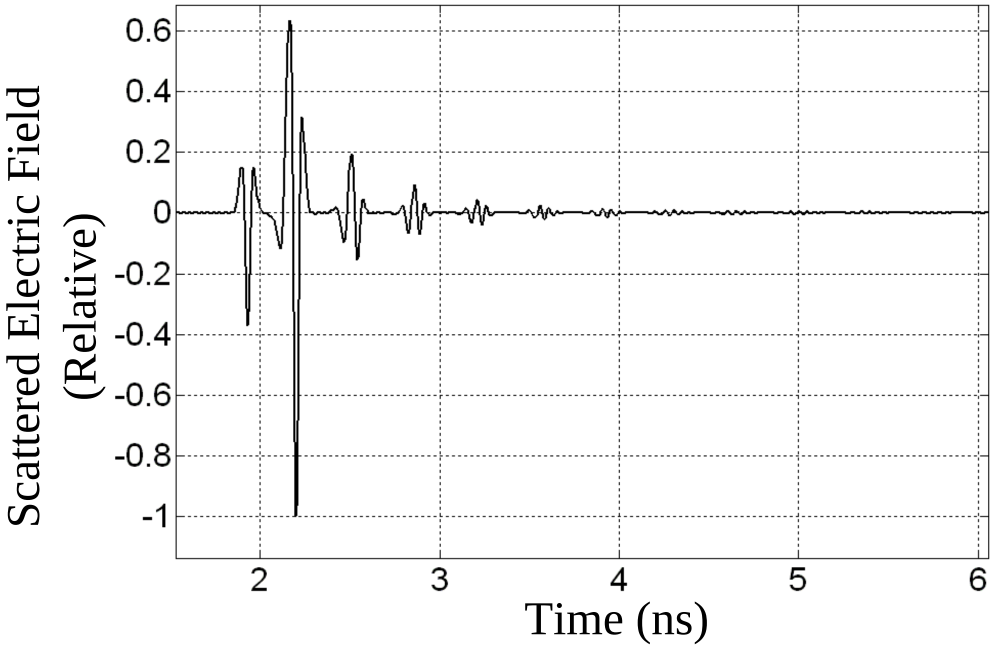

(b)

Figure 6. 8 TM$_z$ backscattered field from a cylindrical dielectric object for $r_a = 0.01$ m, $\varepsilon_1 = 4\varepsilon_0$ F/m, and $\mu_1 = \mu_0$ H/m a) in frequency domain, b) in time domain

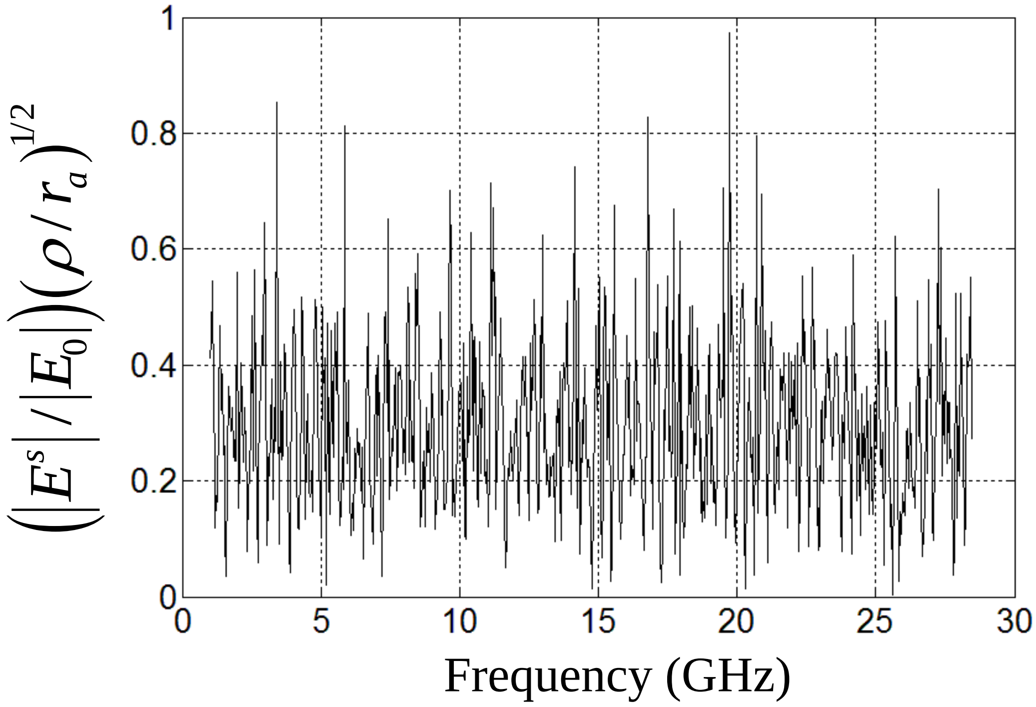

(a)

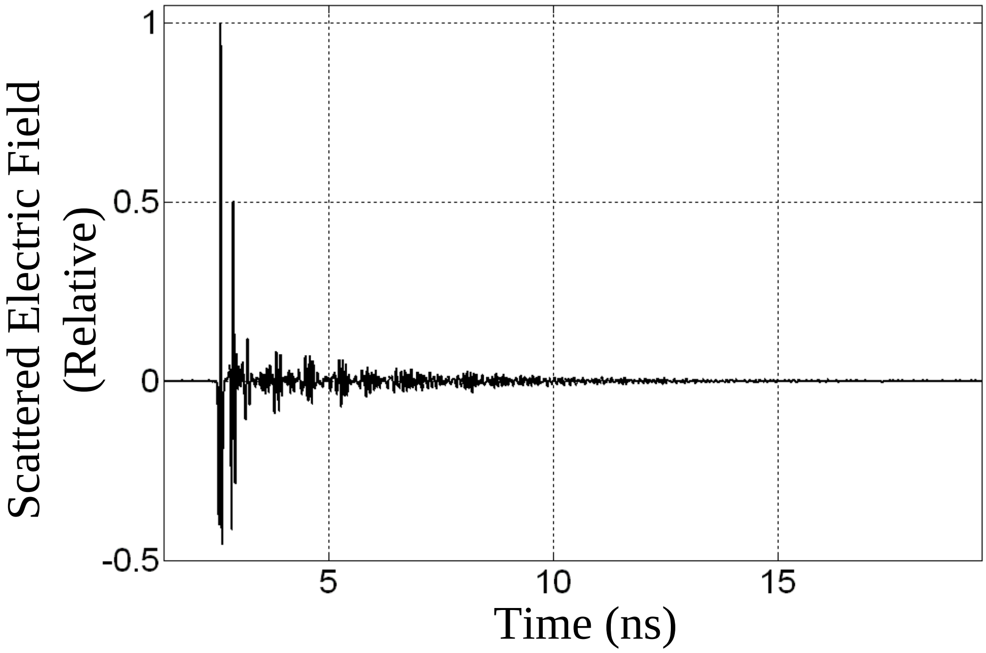

(b)

Figure 6. 9 TM$_z$ backscattered field from a buried cylindrical dielectric object for $r_a = 0.01$ m, $h_c = 0.1$ m, $x_c / r_a = 0.0$, $\varepsilon_1 = 15\varepsilon_0$ F/m, $\varepsilon_2 = 4\varepsilon_0$ F/m, $\sigma_1 = 0.001$ Sm^{-1}, $\sigma_2 = 0.0$ Sm^{-1}, $\mu_1 = \mu_0$ H/m, and $\phi_i = \phi_s = 90^\circ$ a) in frequency domain, b) in time domain

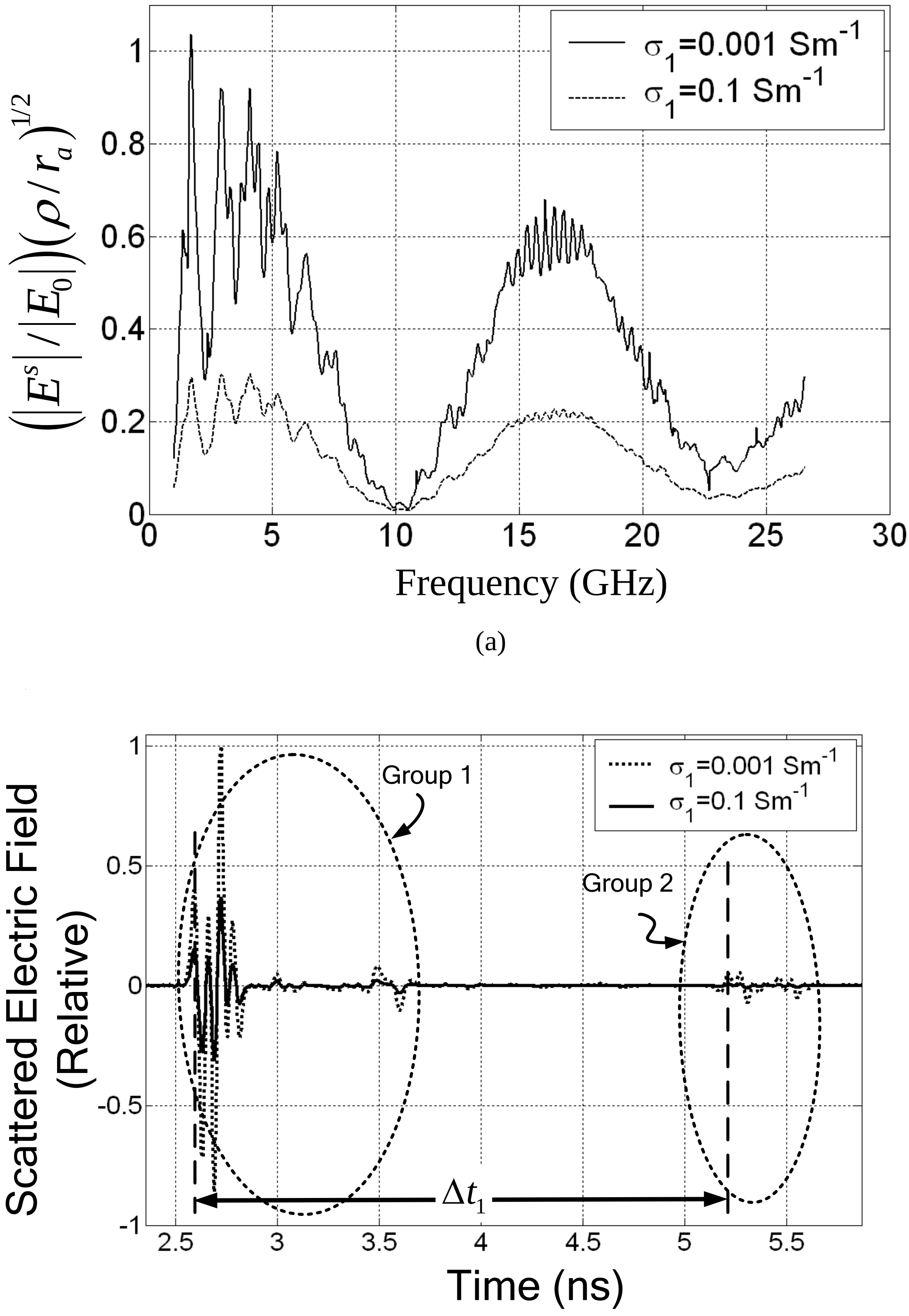

(a)

(c)

Figure 6. 10 TM$_z$ backscattered field from a buried cylindrical PEC object for $r_a = 0.01$ m, $h_c = 0.1$ m, $x_c / r_a = 0.0$, $\varepsilon_1 = 15\varepsilon_0$ F/m, $\mu_1 = \mu_0$ H/m, $\phi_i = \phi_s = 90^\circ$, $w_p = 0.1$ m, $h_p / w_p = 0.1$ a) in frequency domain, b) in time domain

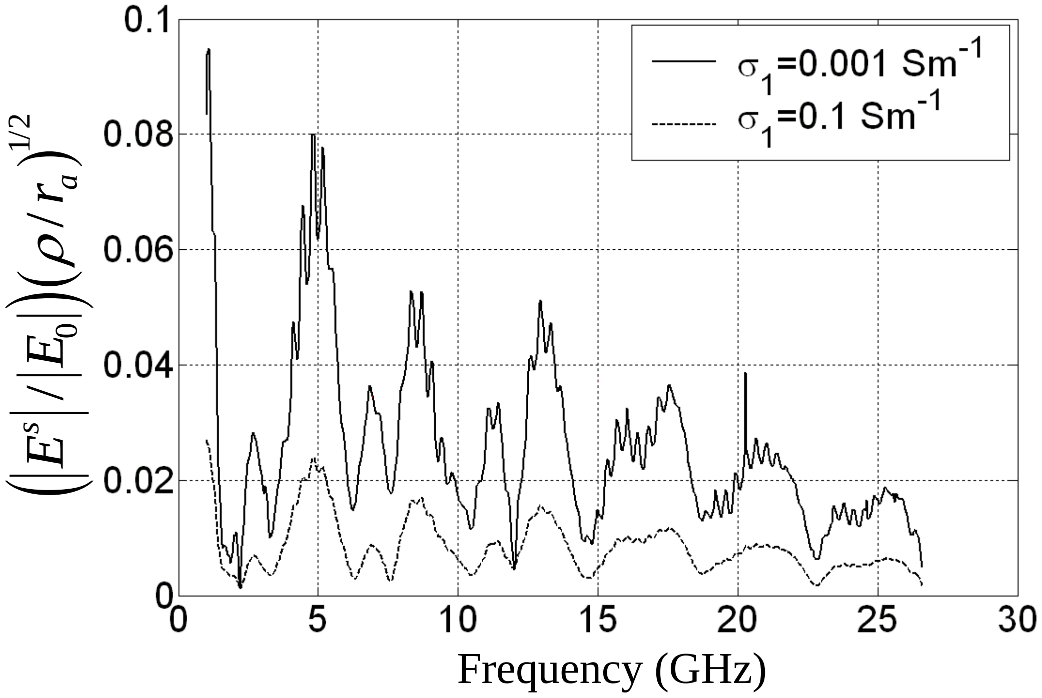

(a)

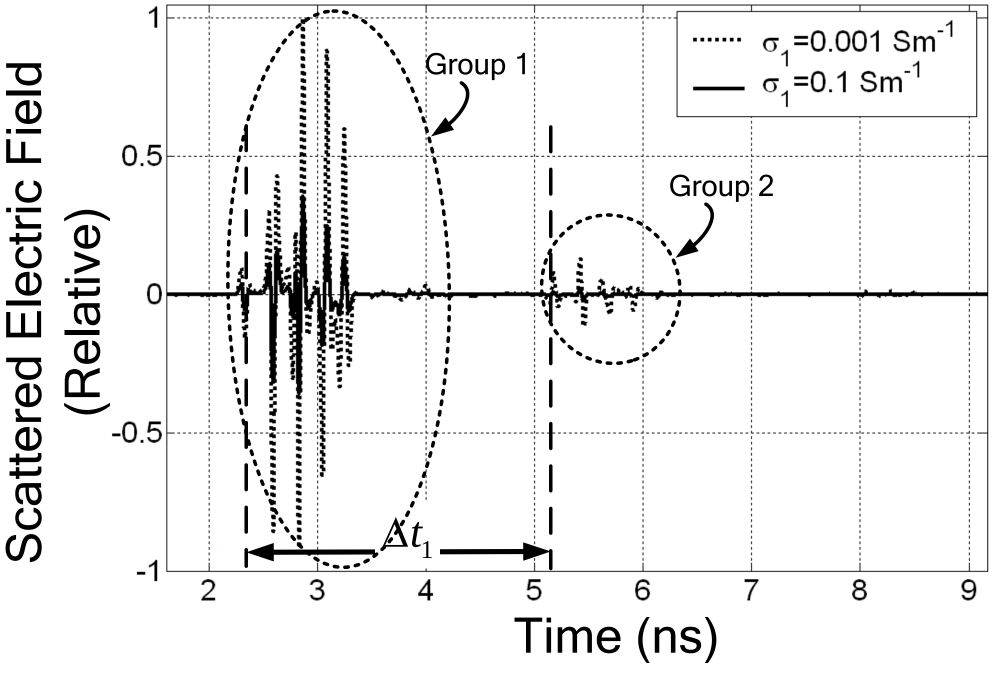

(b)

Figure 6. 11 TM$_z$ backscattered field from a buried cylindrical PEC object for $r_a = 0.01$ m, $h_c = 0.1$ m, $x_c / r_a = 0.0$, $\varepsilon_1 = 15\varepsilon_0$ F/m, $\mu_1 = \mu_0$ H/m, $\phi_i = \phi_s = 20^\circ$, $w_p = 0.1$ m, $h_p / w_p = 0.1$ a) in frequency domain, b) in time domain

CHAPTER 7

CONCLUSIONS

In this thesis, a new numerical solution method for the scattering problems related to cylinder buried in a lossy medium excited by a TM_z polarized electromagnetic wave has been presented. The surface equivalence principle and the perturbation method are employed to form a set of EFIEs for the currents on the object and the portion of the surface most strongly interacting with the object, and solved by MoM in frequency domain. The target is modeled using a two-dimensional cylindrical object, and the surface is chosen to be flat or sinusoidal.

The surface equivalence principle is used to solve the scattered problem of a cylinder and a cylinder coated with a material in Chapter 2 and Chapter 3. Then, in Chapter 4 and Chapter 5, the cylindrical target is buried under a surface having a flat and periodically rough surface. The validity of perturbation assumption is shown by calculating the perturbation currents on the surface. It is shown that the perturbation currents on the surface become negligible except within the region of finite extent near the object for lossy medium. Also, to investigate the accuracy of the method, the medium parameters are taken to be space parameters. It is seen that the method is very accurate. This solution method is utilized to study short pulse scattering from objects buried in a lossy medium with flat and then periodic surface in Chapter 6.

The method yields quite accurate results for rough surfaces since the most appropriate truncation width is selected. Future study is devoted to extend the method to the buried 3D objects.

REFERENCES

[1] Dogaru, T., and Carin, L., (1998). “Time-Domain Sensing of Targets Buried under a Rough Air-Ground Interface”, IEEE Transactions on Antennas and Propagation, 46(3):360-372.

[2] Altuncu, Y., Akduman, I., and Yapar, A., (2007). “Detecting and Locating Dielectric Objects Buried under a Rough İnterface”, IEEE Geoscience and Remote Sensing Letters, 4(2):251-255.

[3] Plett, G. L., Doi, T., and Torrieri, D., (1997). “Mine Detection Using Scattering Parameters”, IEEE Transactions on Neural Networks, 8(6):1456-1467.

[4] Chien, W., and Chiu, C-C., (2005). “Cubic-Spline Expansion with GA for Half-Space Inverse Problems”, ACES Journal, 20(2):136-143.

[5] Huang, C., Chen, C., Chiu, C., and Li, C., (2010). “Reconstruction of the Buried Homogenous Dielectric Cylinder by FDTD and Asynchronous Particle Swarm Optimization”, ACES Journal, 25(8):672-681.

[6] Prokopidis, K. P., and Tsiboukis, T. D., (2007). “Modeling of Ground-Penetrating Radar for Detecting Buried Objects in Dispersive Soils”, ACES Journal, 22(2):287-294.

[7] Bermani, E., Caorsi. S., and Raffetto, M., (2000): “An inverse scattering approach based on a neural network technique for the detection of dielectric cylinders buried in a lossy halfspace”, Progress In Electromagnetics Research, 26:67-87.

[8] Uzunoglu, N. K., and Kanellopoulos, J. D., (1982). “Scattering From Underground Tunnels”, Journal of Physics A: Mathematical and General, 15(2): 459-471.

[9] Kanellopoulos, J. D., and Buris, N. E., (1984). “Scattering From Conducting Cylinders Embedded in a Lossy Medium”, International Journal of Electronics, 57(3):391-401.

[10] Hill, D. A., (1988). “Electromagnetic Scattering by Buried Objects of Low Contrast”, *IEEE* Transactions on Geoscience and Remote Sensing, 26(2):195-203.

[11] Cui, T. J., and Chew, W. C., (1998). “Efficient Evaluation of Sommerfeld Integrals for TM Wave Scattering by Buried Objects”, Journal of Electromagnetic Waves and Applications, 12(5):607-657.

[12] Cui, T. J., Chew, W. C., and Hong, W., (2004). “New Approximate Formulations for EM Scattering by Dielectric Objects”, IEEE Transactions on Antennas and Propagation, 52(3):684-692.

[13] Naqvi, Q. A., Rizvi, A. A., and Yaqoob, Z., (2000). “Scattering of Electromagnetic Waves from a Deeply Buried Circular Cylinder”, Progress in Electromagnetics Research, 27: 37-59.

[14] Ahmed, S., and Naqvi, Q. A., (2008). “Electromagnetic Scattering from a Perfect Electromagnetic Conductor Cylinder Buried in a Dielectric Half-Space”, Progress in Electromagnetics Research, 78:25-38.

[15] Cottis, P. G., and Kanellopoulos, J. D., (1992). “Scattering of Electromagnetic Waves From Cylindrical Inhomogeneities Embedded Inside a Lossy Medium With Sinusoidal Surface”, Journal of Electromagnetic Waves and Applications, 6(4): 445–458.

[16] Cottis, P. G., Vazauros, C. N., Kalamantianos, C., and Kanellopoulos, J. D., (1996). “Scattering From Conducting Cylinders Embedded in a Lossy Medium”, Journal of Electromagnetic Waves and Applications, 10(3):1005-1021.

[17] Lawrance, D. E., and Sarabandi, K., (2002). “Electromagnetic Scattering from a Dielectric Cylinder Buried Beneath a Slightly Rough Surface”, IEEE Transactions on Antennas and Propagation, 50(10):1368–1376.

[18] Altuncu, Y., Yapar, A., and Akduman, I., (2006). “On the Scattering of Electromagnetic Waves by Bodies Buried in a Half-space with Locally Rough Interface”, IEEE Transactions on Geoscience and Remote Sensing, 44(6):1435–1443.

[19] Kizilay, A. and Rothwell, E., (1999). “Efficient computation of transient TM scattering from a cylinder above an infinite periodic surface”, Journal of Electromagnetic Waves and Applications, 13(7):943-961.

[20] Kizilay, A., (2000). A Perturbation Method for Transient Multipath Analysis of Electromagnetic Scattering from Objects above Periodic Surfaces, PhD Dissertion, Michigan State University.

[21] Balanis, C. A., (1989). Advanced Engineering Electromagnetics, John Wiley&Sons, New York.

[22] Harrington, R. F., (1961). Time Harmonic Electromagnetic Fields, McGraw-Hill.

[23] Glisson, A. W., (1984). “An Integral Equation for Electromagnetic Scattering From Homogeneous Dielectric Bodies”, IEEE Transactions on Antennas and Propagation, 32 (2):173-175.

[24] Booysen, A. J., (2000). “A Physical Interpretation of the Equivalence Theorem”, IEEE Transactions on Antennas and Propagation, 48(8):1260-1262.

[25] Arvas, E., Rao, S. M., and Sarkar, T.K., (1986). “E-field Solution of TM-Scattering from Multiple Perfectly Conducting and Lossy Dielectric Cylinders of Arbitrary Cross-Section”, IEE Proceedings, 133(2):115-121.

[26] Arvas, E., Ross, M., and Qian, Y., (1988). “TM Scattering from a Conducting Cylinder of Arbitrary Cross Section Covered by Multiple Layers of Lossy Dielectrics”, IEE Proceedings H, 135(4):226-230.

[27] Arvas, E., Ross, M., and Qian, Y., (1989). “TE Scattering from a Conducting Cylinder of Arbitrary Cross-section Covered by Multiple Layers of Lossy Dielectrics”, IEE Proceedings H, 136(6):425-430.

[28] Harrington, R. F., (1992). Field Computation by Moment Methods, IEEE Press, New York.

[29] Knott, E. F., Shaeffer, J. F., Tuley, M. T., (2004), Radar Cross Section, Scitech Publishing, Boston.

[30] Norman, A. J., and Nyquist, D.P., (1996). Transient Scattering of Electromagnetic Waves in an Ocean Environment, PhD Dissertion, Michigan State University.

[31] Norman, A., Nyquist, D.P., Rothwell, E., Chen, K.M., Ross, J., and Ilavarasan, P., (1996). “Transient scattering of a short pulse from a conducting sinusoidal surface”, Journal of Electromagnetic Waves and Applications, 10(4):461-487.

[32] Warnick, K. F., (2008). “Numerical Analysis for Electromagnetic Integral Equations”, Artech House.

[33] Falorni, P., Capineri, L., Masotti, L., Windsor, C. G., (2007). “Analysis of time domain ultra-wide band radar signals reflected by buried objects”, PIERS ONLINE, 3(5):662-665.

APPENDIX-A

CURVE OF THE MAGNETIC VECTOR POTENTIAL

Rotational of magnetic potential vector is given by the following line integral:

$$\nabla\times\vec{F}\left(\vec{M}\right)=\frac{\varepsilon}{4j}\oint_{C}\nabla\times\left(\vec{M}\left(\vec{\rho}'\right)\ H_0^{(2)}\left(k\left|\vec{\rho}-\vec{\rho}'\right|\right)\right).\ dl' \qquad \text{(App.A.1)}$$

Using a vector identity

$$\begin{aligned}\nabla\times\left(\vec{M}\left(\vec{\rho}'\right)\ H_0^{(2)}\left(k\left|\vec{\rho}-\vec{\rho}'\right|\right)\right)&=H_0^{(2)}\left(k\left|\vec{\rho}-\vec{\rho}'\right|\right)\ \nabla\times\vec{M}\left(\vec{\rho}'\right)\\&\quad+\nabla\left(H_0^{(2)}\left(k\left|\vec{\rho}-\vec{\rho}'\right|\right)\right)\ \times\vec{M}\left(\vec{\rho}'\right)\end{aligned} \qquad \text{(App.A.2)}$$

Because of the magnetic current depends on source coordinate variables

$$\nabla\times\vec{M}\left(\vec{\rho}'\right)=0 \qquad \text{(App.A.3)}$$

The gradient of the zeroth-order Hankel function

$$\nabla\left(H_0^{(2)}\left(kR\right)\right)=\hat{R}\,\frac{\partial H_0^{(2)}\left(kR\right)}{\partial R}=-\hat{R}kH_1^{(2)}\left(kR\right) \qquad \text{(App.A.4)}$$

where

$$\hat{R}=\frac{\left(\vec{\rho}-\vec{\rho}'\right)}{\left|\vec{\rho}-\vec{\rho}'\right|} \qquad \text{(App.A.5)}$$

and equation App.A.2 becomes

$$\nabla\left(H_0^{(2)}\left(k\left|\vec{\rho}-\vec{\rho}'\right|\right)\right)\ \times\vec{M}\left(\vec{\rho}'\right)=-kM\left(\vec{\rho}'\right)\left(\hat{R}\times\hat{\tau}\right)H_1^{(2)}\left(k\left|\vec{\rho}-\vec{\rho}'\right|\right) \qquad \text{(App.A.6)}$$

where $\hat{\tau}=\hat{z}\times\hat{n}$, $\hat{R}\times\hat{\tau}=\hat{z}\left(\hat{n}\cdot\hat{R}\right)-\hat{R}\left(\hat{n}\cdot\hat{z}\right)$ and here $\hat{n}\cdot\hat{z}=0$. Equation App.A.6 becomes

$$\nabla\left(H_0^{(2)}\left(k\left|\vec{\rho}-\vec{\rho}'\right|\right)\right)\ \times\vec{M}\left(\vec{\rho}'\right)=\hat{z}kM\left(\vec{\rho}'\right)\left(\hat{n}\cdot\hat{R}\right)H_1^{(2)}\left(k\left|\vec{\rho}-\vec{\rho}'\right|\right) \qquad \text{(App.A.7)}$$

Finally, after using equation 2.29 in chapter 2, equation App.A.1:

$$\nabla\times\vec{F}\left(\vec{M}\right)=\hat{z}\,\frac{\varepsilon k}{4j}\sum_{i=1}^{N}K_i\oint_{C}H_1^{(2)}\left(k\left|\vec{\rho}-\vec{\rho}'\right|\right)\left(\hat{n}\cdot\hat{R}\right)dl' \qquad \text{(App.A.8)}$$

APPENDIX-B

CALCULATION OF SELF TERMS

When the integration paths go through the source points, it makes the numerical integration very difficult to compute. Therefore, the self terms should be approximated by using the Hankel function terms for small arguments [21]

$$H_0^{(2)}\left(k\,u_L\right) \approx 1 - j\frac{2}{\pi}\ln\left(\frac{k\gamma u_L}{2}\right) \qquad for\ ku_L \ll 1 \tag{App.B.1}$$

where u_L represents the position along segment L as shown in Figure App.B.1, and $\gamma = 1.781$. Evaluation of the integrals containing self terms yields

$$\int_{-\Delta_s/2}^{\Delta_s/2} H_0^{(2)}\left(k\,u_L\right)\,du_L = \Delta_s\left[1 - j\frac{2}{\pi}\left(\ln\left(\frac{k\gamma}{4}\Delta_s\right) - 1\right)\right] \tag{App.B.2}$$

Here, the widths of the constant-current strips are represented by Δ_s.

During the integration while $\vec{\rho} \to \vec{\rho}'$, $H_1^{(2)}\left(k\,\left|\vec{\rho} - \vec{\rho}'\right|\right)$ will vary rapidly when $\vec{\rho}'$ gets close to $\vec{\rho}$. The integration should be carefully evaluated since $k\,\left|\vec{\rho} - \vec{\rho}'\right| \to 0$.

$$\lim_{\rho \to \rho'} \int_{\Delta_c} H_1^{(2)}\left(k\left|\vec{\rho} - \vec{\rho}'\right|\right)\frac{\hat{n}\cdot\left(\vec{\rho} - \vec{\rho}'\right)}{\left|\vec{\rho} - \vec{\rho}'\right|}\,dl' = \lim_{\rho \to \rho'} \int_{\Delta_c} H_1^{(2)}\left(k\left|\vec{\rho} - \vec{\rho}'\right|\right)\cos\left(\psi'\right)dl' \tag{App.B.3}$$

From Figure App.B.2

$$\cos\left(\psi'\right) = \frac{\delta}{\sqrt{\delta^2 + s'^2}} \tag{App.B.4}$$

For small arguments $H_1^{(2)}\left(k\,\left|\vec{\rho} - \vec{\rho}'\right|\right)$ can be approximated as

$$H_1^{(2)}\left(k\,\left|\vec{\rho} - \vec{\rho}'\right|\right) = H_1^{(2)}\left(k\,\sqrt{\delta^2 + s'^2}\right) \approx \frac{2j}{\pi k\sqrt{\delta^2 + s'^2}} \tag{App.B.5}$$

Substituting (App.B.4) and (App.B.5) into (App.B.3)

$$
\begin{aligned}
\lim_{\rho\to\rho'}\int_{\Delta_c} H_1^{(2)}\left(k\left|\vec{\rho}-\vec{\rho}'\right|\right)\cos\left(\psi'\right)dl' &\approx \lim_{\delta\to 0}\int_{-\frac{\Delta_c}{2}}^{\frac{\Delta_c}{2}} \frac{\delta}{\sqrt{\delta^2+s'^2}}\,\frac{2j}{\pi k\sqrt{\delta^2+s'^2}}\,ds' \\
&\approx \frac{2j}{\pi k}\lim_{\delta\to 0}\int_{-\frac{\Delta_c}{2}}^{\frac{\Delta_c}{2}} \frac{\delta}{\left(\delta^2+s'^2\right)}\,ds' \qquad \text{(App.B.6)} \\
&\approx \frac{4j}{\pi k}\lim_{\delta\to 0}\tan^{-1}\left[\frac{\Delta C/2}{\delta}\right] \\
&\approx \frac{2j}{k}
\end{aligned}
$$

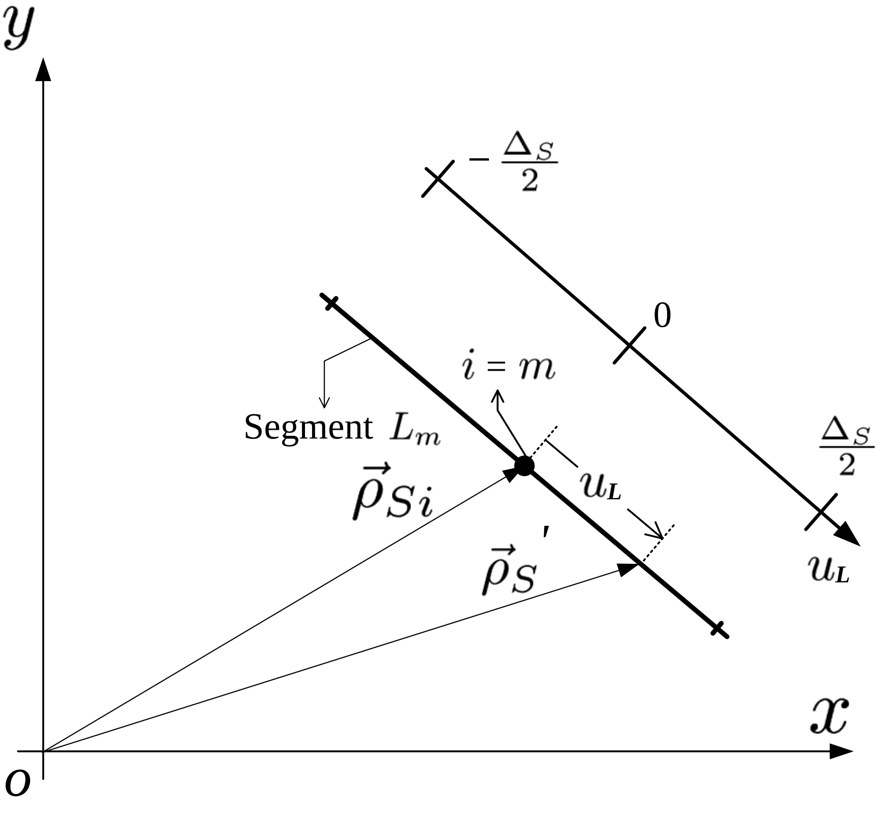

Figure App.B.1 Evaluation of the self terms

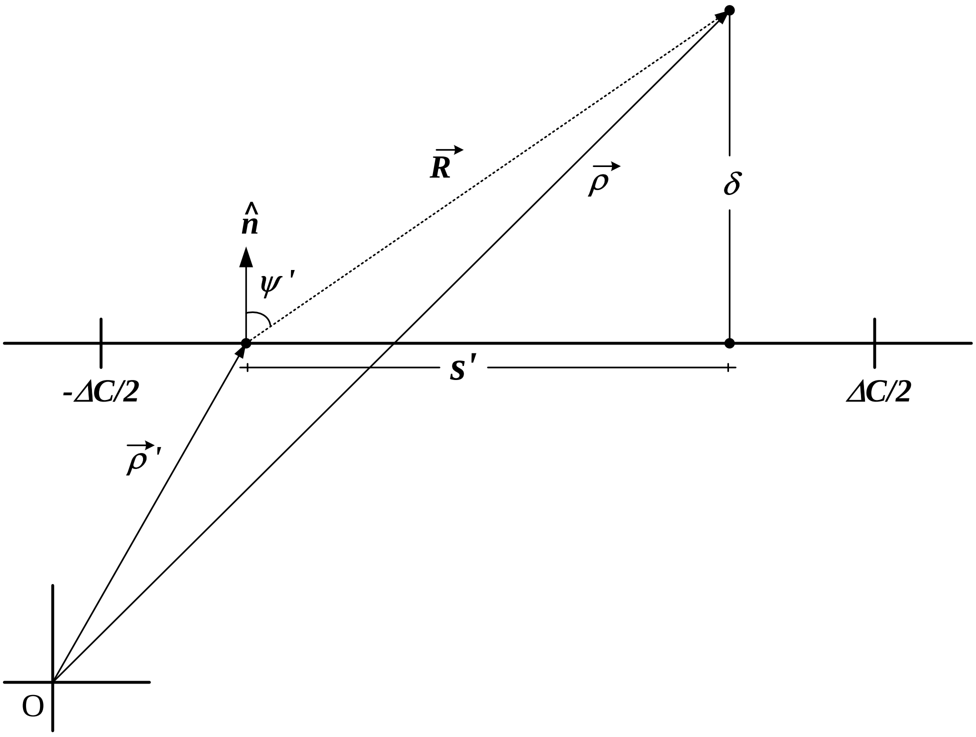

Figure App. B.2 Evaluation of Principle Value

AUTOBIOGRAPHY

PERSONEL INFORMATION

Name Surname	: Senem MAKAL
Birthdate and Birthplace	: 01/01/1983-Tunceli
Foreign Language	: English
E-mail	: smakal@yildiz.edu.tr

EDUCATION

Degree	**Department**	**School/University**	**Graduation Year**
M.S	Electronics and Communications Engineering	Yıldız Technical Uni.	2007
B.S	Electronics and Communications Engineering	Yıldız Technical Uni.	2005
High School		Nevvar Salih İşgören High School	2001

WORK EXPERINCES

Year	**Company/Institution**	**Position**
2011	TÜBİTAK	Senior Researcher
2005	YTU	Research Assistant

PUBLICATIONS

Articles

1. Makal, S., and Kizilay, A., (2011). “A Neural-Based Electromagnetic Inverse Scattering Approach to the Detection of a Conducting Cylinder Coated with a Dielectric Material”, Turkish Journal of Electrical Engineering & Computer Sciences, accepted for publication.

2. Makal, S., and Kizilay, A., (2011). “Computation of the Scattered Fields from a dielectric Object Buried in a Medium with a Periodic Surface by a Decomposition Method”, IET Microwaves, Antennas & Propagation, 5(14):1703-1709.

3. Makal, S., and Kizilay, A., (2011). “A Decomposition Method for the Electromagnetic Scattering From a Conductive Object Buried in a Lossy Medium”, The Applied Computational Electromagnetic Society, 26(4):340-347.

4. Makal, S., Kizilay, A., Durak, L., (2008). “On The Target Classification Through Wavelet-Compressed Scattered Ultrawide-Band Electric Field Data and ROC Analysis”, Progress In Electromagnetics Research, 82:419-431.

5. Kızılay, A., and Makal, S., (2007). “A Neural Network Solution for Identification and Classification of Cylindrical Targets above Perfectly Conducting Flat Surfaces”, Journal of Electromagnetic Waves and Applications, 21(14):2147-2156.

Conference Papers

1. Makal, S., and Kızılay, A., (2011). “Calculation of Scattered TM_z Waves from a Dielectric Scatterer Buried Inside a Lossy Ground”, URSI 2011, 13-20 August 2011, Istanbul, Turkey.

2. Makal, S., and Kızılay, A., (2009). “Neural Network Based Target Recognition”, Progress In Electromagnetics Research Symposium (PIERS2009), 23-27 March 2009, Beijing, China.

3. Makal, S., Ozyilmaz, L., Palavaroglu, S., (2008). “Neural Network Based Determination of Splice Junctions by ROC Analysis”, International Conference on Computer Systems Science and Engineering (CSSE08), 24-26 September 2008, Heidelberg, Germany.

4. Makal, S., Durak, L., Kızılay, A., (2008). “Dalgacık Dönüsümü ve ROC Analizi Yardımıyla Silindirik Hedeflerin Sınıflandırılması”, Sinyal İşleme ve İletişim Uygulamaları Kurultayı (SIU2008), 19-12 Nisan 2008, Aydın, Türkiye.

5. Kızılay, A., and Makal, S., (2007). “A Neural Network Model for Target Identification of Cylindrical Targets Located above Perfectly Conducting Flat Surface”, Progress In Electromagnetics Research Symposium (PIERS2007), 27-30 August 2007, Prague, Czech Republic.

6. Kızılay, A., and Makal, S., (2007). “Identification of Multiple Cylindrical Targets Located above Perfectly Conducting Flat Surface by Artificial Neural Networks”, Progress In Electromagnetics Research Symposium (PIERS2007), 27-30 August 2007, Prague, Czech Republic.

7. Makal, S., and Kızılay, A., (2007). “Classification of Cylindrical Targets above Perfectly Conducting Flat Surfaces by Multilayer Perceptrons”, International Symposium on INnovations in Intelligent SysTems and Applications (INISTA 2007), 20-23 June 2007, İstanbul, Turkey.

8. Makal, S., and Ozyilmaz, L., (2007). “Determination of Splice Junctions on DNA by Neural Networks”, International Symposium on INnovations in Intelligent SysTems and Applications (INISTA 2007), 20-23 June 2007, İstanbul, Turkey.

9. Makal, S., and Kızılay, A., (2007). “Identification of Targets above Perfectly Conducting Surfaces by Using Artificial Neural Networks”, Mediterrenean Microwave Symposium (MMS 2007), 14-16 May 2007, Budapest, Hungary.

10. Makal, S., and Kızılay, A., (2007). “Mükemmel İletken Düz Yüzeyler Üzerindeki Silindirik Hedeflerin İstatistiksel Sinir Ağları İle Sınıflandırılması”, Sinyal İşleme ve İletişim Uygulamaları Kurultayı (SIU2007), 11-13 Haziran 2007, Eskişehir, Türkiye.

Project

1. Calculation of Scattering Electromagnetic Fields from the Buried Cylindrical Targets Under the Sinusoidal Surface, Yildiz Technical University Scientific Research Projects Coordination Department. Project number: 2010-04-03-DOP01.

AWARDS

1.URSI-Young Scientist Award

2.TÜBİTAK National Scholarship Programme for M.Sc. Students

3.TÜBİTAK National Scholarship Programme for Ph.D. Students